Single Crystal Growth of High Melting Oxide Materials by Means of Induction Skull-Melting

vorgelegt von

Matthias Stephan Paun, M.Sc.

geb. in Schwabmünchen

von der Fakultät II – Mathematik und Naturwissenschaften

der Technischen Universität Berlin

zur Erlangung des akademischen Grades

Doktor der Naturwissenschaften

-Dr. rer. nat.-

genehmigte Dissertation

Promotionsausschuss:

Vorsitzender: Prof. Dr. Martin Kaupp

1. Gutachter: Prof. Dr. Martin Lerch

2. Gutachter: Prof. Dr. Matthias Bickermann

3. Gutachter: Prof. Dr. Manfred Mühlberg

Tag der wissenschaftlichen Aussprache: 29.10.2015

Berlin 2015

ABSTRACT

Various high melting oxide single crystals were grown by implementation of the induction skull melting technique. This technique can be described of a combination of high frequency induction heating and a water cooled crucible. Various single crystals were successfully grown; alkaline earth zirconates, transition metal doped titania and rare earth element (REE) doped yttrium stabilized zirconium dioxide (YSZ). The grown alkaline earth zirconate single crystals are $CaZrO_3$, $SrZrO_3$ and $BaZrO_3$ and belong all to the perovskite structure type. $CaZrO_3$ and $SrZrO_3$ exhibit both an orthorhombic distortion and they crystalize in space group *Pnma* while $BaZrO_3$ is belonging to the cubic aristotype $Pm\bar{3}m$. The two orthorhombic zirconate crystals are featuring twins. The twinning emerged through the transformation from cubic to orthorhombic and the loss of symmetry. $SrZrO_3$ single crystals were grown twice; under air and nitrogen atmosphere. The UV-Vis. reflection spectroscopy measurements revealed that the absorbance of both $SrZrO_3$ samples differ from each other, especially at lower wavenumbers. $SrZrO_3$ also shows luminescence effects when excited at approximately 260 nm. The emission spectra also differ between the two $SrZrO_3$ samples. It is suggested that a small amount of nitrogen incorporated in the lattice is responsible for this effect. $CaZrO_3$ was used as substrate for the growth of multiferroic materials carried out at the Institute of Crystal Growth in Berlin (IKZ). $K_{0.8}Na_{0.2}NbO_3$ layers were successfully grown on $CaZrO_3$. However, the twinning present above described resulted in an overall poor quality of the multiferroic material. TiO_2 single crystals with five different transition metal dopants (Ni, Fe, Co, Mn, Nb) were successfully grown. The doping should ensure a decrease in optical band-gap of the host material (~ 3 eV). All titania crystals have a tetragonal rutile structure and belong to the space group $P4_2/mnm$. Optical reflectance measurements, in combination with the Kubelka-Munk model, revealed a successful decrease of the optical band-gap compared to the undoped host material. The ICP-OES measurements show an overall good correlation with the theoretical composition. Several yttrium stabilized zirconium dioxide (YSZ) single crystals with various REE (co-)dopants (Eu, Er, Yb, Tb, Tm) were successfully grown for the first time as part of this work. All phases are cubic and belong to the space group $Fm\bar{3}m$ (CaF_2 structure type). The crystals feature a fluorescence effect by UV light due to the REE doping as well as a thermochromic effect in the case of Tb:YSZ. The high temperature UV-Vis. spectroscopy showed that Tb doped YSZ was also the only sample which has a higher optical absorbance at higher temperatures. The absorbance remained at a higher magnitude even after the cooling.

ACKNOWLEDGMENT

I would like to thank all the persons who helped me on the way during my work on this thesis:

Firstly, Prof. Dr. Martin Lerch for the opportunity to work on this interesting topic as well as for his direction and support,

Prof. Dr. Matthias Bickermann for the great and friendly support during my thesis and for his time as second assessor,

Prof. Dr. Manfred Mühlberg for his time as third assessor,

Prof. Dr. Martin Kaupp for his time as chairperson,

Dr. Dennis Wiedemann for the structure refinement of the single crystals data as well as the help on any crystallographic issues,

Dr. Klaus Irmscher from the Leibniz Institute of crystal growth for the optical transmission measurements on the doped YSZ samples,

Dr. Reinhard Uecker and Dr. Jutta Schwarzkopf form the Leibniz Institute of crystal growth for their cooperation on the $CaZrO_3$ substrates,

Dr. Rainer Bertram for the ICP-OES measurements on the doped titania,

Dr. Stefan Berendts for his help on any technical issues and the proofread of this thesis,

Dr. Gregor Ulbrich for his work and help regarding the Skull melting technique,

Dipl.-Chem. Sven Kühn (AK Ressler) for the optical reflectance measurements of the TiO_2 samples,

Dipl.-Chem. Steven Orthmann and Dipl.-Chem. Tobias Lüdtke for their re-oxidation experiments as well as the help during the Skull melting growth experiments,

Eva Heppke, M.Sc. for her help and support on the Skull melting technique,

Sascha Krüger, M.Sc., University of Siegen, for the optical UV/Vis. measurements on the zirconate crystals,

Martin Naumann from the Leibniz institute of crystal growth for the high temperature UV/Vis. measurements on the doped YSZ crystals,

Paula Nixdorf for the single crystal measurements,

I thank everyone from the workgroup of Martin Lerch for the great time:
Anna, Sevi, Steven, Tobi, Eva, Suliman, Gregor, Dennis, Björn, Stefan, Claudia and Abdulla.

Table of Contents

1. INTRODUCTION/MOTIVATION

Oxides are the most common chemical compounds. Earth crust consists mostly of solid oxides (with SiO_2 being the most prominent), as a result of elements being oxidized by oxygen in water or air. The oxide class of minerals is the largest and most diverse group in mineralogy. Minerals were the first single crystal materials which were studied for their properties and overall characteristics. However, in the discovery and understanding of new materials, artificial single crystals play an essential role. These single crystals provide the ability to study the properties of the material free of any grain boundaries, and in the ideal case without any defects. In addition, most properties of a crystal depend on its orientation, so the information is lost when studying polycrystalline materials. In addition, insight gained through examining the properties of single crystals provide the baseline information necessary for accurate theoretical modeling and the ultimate understanding of the intrinsic properties of a new material. This thesis will focus on three distinct oxide material systems, namely perovskites in form of alkaline earth zirconates ($CaZrO_3$, $SrZrO_3$ and $BaZrO_3$), titania (TiO_2) and yttrium-stabilized zirconium dioxide (YSZ). These materials will be grown as single crystals and analyzed structurally (powder and single crystal diffraction) as well as chemically and optically. Oxide perovskite materials, especially alkaline earth ones, are very versatile and provide a great mechanical and chemical stability. They also are also promising candidates for the usage as substrates for multiferroic materials. However, the very high melting point resulted in a lack of single crystals available of this kind. TiO_2 shows relatively high reactivity but chemical stability under ultraviolet light, whose energy exceeds the band-gap of approximately 3 eV in the rutile crystalline phase [1]. This makes TiO_2 suitable for energy-related technologies like photocatalysis and water splitting. Various TiO_2 modifications can be achieved via transition metal doping, effectively reducing the optical band-gap of the material. The application of crystalline materials in photonic systems has become crucial for research over the last few years, for application as tunable solid lasers in the visible domain, the conception of planar guides, high non-linear optical material and smart windows [2, 3]. Such materials appear to be an interesting way to get non-conventional luminescence properties from rare earth elements (REE) ions used as dopants [4, 5]. REE doping is also necessary to implement active wave guides. Due to the phenomenon of luminescence concentration quenching, host matrices doped with few percent of REE are the best compromise between long lifetime and high luminescence intensity.

Yttrium-stabilized zirconium dioxide (YSZ) is considered to be suitable doping hosts for the rare-earth ions. Furthermore, YSZ is chemically stable and does not decompose even at low pH values [6]. Many possibilities exist for a successful single crystal growth, most are rather unsuitable for these specific cases. It is impracticable to grow these oxide single crystals from solutions, as the solubility of these oxides in most solvents is low. It is also difficult to grow by physical or chemical vapor deposition since the growth rates are low. The most successful growth method became the growth from melt. However, these materials feature all a very high melting point, which limits the possible growth methods from melt. The induction Skull melting technique became therefore a suitable method for the growth of fairly large high melting single crystal materials.

2. THEORETICAL BACKGROUND

2.1 Perovskites

Introduction

The mineral perovskite was discovered and named by Gustav Rose in 1839 which was obtained in the Ural Mountains. Perovskite is named after a Russian mineralogist, Count Lev Aleksevich von Perovski, a Russian nobleman and mineralogist who served as secretary of interior affairs under Nicholas I in 1842. The term perovskite was originally reserved only for the mineral $CaTiO_3$. The first synthetic perovskites were produced by Goldschmidt at the University of Oslo, which led to the use of the term "perovskite" as a description of a class of compounds sharing the same general stoichiometry and connectivity as in $CaTiO_3$. The perovskite structure has the general AMX_3 stoichiometry where "*A*" and "*M*" are cations and "*X*" is an anion. Substitution of different ions on each site is readily accepted making the perovskite structure type one of the most frequently encountered structure in solid state chemistry. Perovskites have held the interest of material scientists for a significant period of time due to the wide range of chemical compositions and variety of resulting physical properties. The perovskite structure can incorporate most of the metallic ions in the periodic table and a significant number of different anions. Perovskites have been reported with all naturally occurring cations in the periodic table with the exception of boron (B) and beryllium (Be). Phosphorus and noble gases are also not observed in the perovskite structure. Most of the perovskite compounds are oxides or fluorides, but the perovskite structure is also known for halides [7] sulfides [8], hydrides [9], cyanides [10], oxide fluorides [11] and oxide nitrides [12].

Physical Properties

Since perovskite materials have such a wide range of composition, the physical and chemical properties can be very diverse as well. For a long time mineralogists and crystallographers have been interested in the perovskite structure, which is proposed to be the most abundant mineral on earth in one of its high pressure form of $Mg_{(1-x-y)}Ca_xFe_ySiO_3$ (x, y = 0 – 0.5)[13]. Catalytic properties are present in a number of perovskites including the potential automotive catalytic converter material $La(Fe_{0.57}Co_{0.38}Pd_{0.05})O_3$ [14]. Solid solutions of $CaTiO_3$-$NdAlO_3$ are employed as microwave resonators for "third generation" mobile phone base stations [15]. Additionally, perovskites formulated from mixtures of ~89 % $Ba(Zn_{0.25}Ta_{0.75})O_3$, 7.5 % $Ba(Ni_{0.25}Ta_{0.75})O_3$ and 3.5 % $BaZrO_3$ have microwave dielectric properties [16]. Electrical conductivity ranges from highly insulating $BaZrO_3$ to metallic $SrRuO_3$ [17], whereby, $BaTiO_3$ has a high dielectric constant, is it ferroelectric and used in capacitors [18]. Perovskites with piezoelectric properties, in which the materials convert mechanical (i.e. strain) energy to electrical energy and vice versa, such as $Pb(Zr_{1-x}Ti_x)O_3$ (x = 0 – 1) and $Pb_{0.33}Sc_{0.66}TaO_3$, play a dominant role in the electro-ceramic industry including applications such as ceramic phonographic cartridges, sensitive microphones, powerful sonar, piezo-ignition systems, pressure gauges and transducers, ultrasonic imaging, and relays [25]. Such materials also serve as critical components in a number of smart devices, which are able to sense the surrounding environment and respond to it [19 - 21]. The highest superconducting transition temperature for a non cuprate oxide material is observed in $BaPb_{1-x}Bi_xO_3$ (x ≈ 0.05 – 0.30) [22]. High temperature cuprate superconductors adopt perovskite related crystal structures [23]. Members of the manganate based perovskite system, $(Ln_{1-x}A_x)MnO_3$ (*Ln* = lanthanides, *A* = alkaline earth elements), are known for their good magnetic and magneto-resistive (CMR) properties [24]. $AZrO_3$ (*A* = alkaline earth elements) perovskites are showing strong mechanical, thermal and chemical stability.

Crystal structure

The ideal perovskite structure has AMX_3 stoichiometry and is composed of a three dimensional network of regular corner linked MX_6 octahedra. The perovskite topology has an efficient packing scheme. Historically, the octahedral site (*M*) is designated to the *B*-site. In the ideal case, the *M*-site cations are at the center of the octahedra with the *A*-cations centrally located in the body center of the cube formed by eight corner linked octahedra.

The symmetry of the ideal perovskite structure is cubic in space group $Pm\bar{3}m$ (No. 221). Axes formed by *M*-*X* bonds of the octahedra coincide with the crystallographic cubic axes [25]. The ideal structure has no variable in the structure besides the lattice parameter. Several points of view are used to describe the perovskite structure, with the corner-sharing octahedra description most commonly used. The corner-sharing description is the most intuitive depiction when considering distortions from ideal symmetry [25].

Tolerance factor

The Goldschmidt tolerance factor is a measure of the fit of the *A*-site cation to the cubic corner-sharing octahedral network and reflects the structural distortion, force constant of binding, rotation, and tilting of the cation octahedra [43]. Twice the *M*-*X* bond length is equal twice the cell edge, and the *A*-*X* bond length is equal twice the face diagonal [25]. The tolerance factor is shown in the following equation:

$$\tau = \frac{R_A + R_X}{\sqrt{2}\,(R_M + R_X)} \qquad (1)$$

Where τ is the tolerance factor, R_A, R_M and R_X are the ionic radii of the *A*-cation, *M*-cation and *X*-anion, respectively. Ionic radii are tabulated by Shannon [44]. The tolerance factor is an approximate guide to estimate the structural stability of the perovskite phase. The upper limit of the tolerance factor for a cubic structure lies at approximately 1.04, whereas a tolerance factor from 0.71 to 0.87 lies nears the range where the orthorhombic structure type becomes more stable. Tolerance factors higher than 1.04 correspond to stable hexagonal structures while at the lower end (> 0.71) structures like ilmenite became more stable.

Distortions from Cubic Symmetry

It is worth mentioning that the mineral $CaTiO_3$, does not adopt the aristotype cubic structure. The parent structure type is referred to as the aristotype, and distorted perovskites are designated hettotypes.

The symmetry of $CaTiO_3$ is lowered from cubic ($Pm\bar{3}m$, $Z = 1$) to orthorhombic ($Pnma$, $Z = 4$) by a cooperative tilting of the titanium centered octahedra [26]. This distortion is driven by the mismatch between the size of the central cavity in the corner sharing octahedral network and the undersized ionic radius of the Ca^{2+} ion. Because of this octahedral tilting distortion the coordination number of Ca^{2+} is lowered from 12 to 8 to reduce the tension in the remaining Ca-O bonds and increase the lattice energy [27]. The local octahedral coordination of the Ti^{4+} ion, however, shows very little disorder. Three different types of distortions were identified, including: distortions of MX_6 octahedral units, *M*-cation displacements within the octahedra, and octahedral tilting distortions [28]. The firstly mentioned distortions of MX_6 octahedral units often result from electronic factors. In octahedral coordination, the 3d transition metal cations with high-spin configuration have electron configurations $(t_{2g})^3(e_g)^1$ and $(t_{2g})^6(e_g)^3$, respectively. From an electronically standpoint this is an unfavorable situation and the Jahn-Teller (J-T) effects results a distortion of the geometry thereby, lowering the symmetry of the octahedron removes the electronic degeneracy [29]. A distortion at *M-X* bond lengths results in an energetic stabilization. J-T distortions typically occur without a large deviation of the *X-M-X* bond angles from their ideal values of 90 ° and 180 °, respectively. Second, displacements of octahedral cations are the result of the combination of structural influences and electronic factors. Octahedral cation displacements are typically observed in compositions with a Goldschmidt tolerance factor greater than 1. Oversized cations stretch the octahedral bonds, resulting in an increase of octahedral volume and therefore a reduction of the *M-X* bonding lengths. The d^0 cations that undergo a second order Jahn-Teller distortion undergo a displacement of the octahedral cation towards anions occurs to increase the bonding of the octahedral cation [25]. Stretching of the octahedral cation is observed, for example, in $BaTiO_3$, resulting in ferroelectric properties [22]. Third, octahedral tilting is the most common type of distortion the perovskite structure type undergoes [26]. Distortion from ideal cubic symmetry of the aristotype cubic perovskite ($Pm\bar{3}m$) occurs by a practically rigid tilting of the octahedral units while maintaining the corner sharing connectivity. Distortions in the octahedral angles are very small (~4 ° for *X-M-X*). Octahedral tilting allows greater flexibility in the coordination of the *A*-cation while maintaining a regular coordination environment for the octahedral cation. Octahedral tilting reduces the symmetry of the *A* cation coordination environment and leads to a significant change in the *M-X* bond lengths. The octahedra can tilt in multiple ways, each leading to a different coordination environment for the *M* cations.

Classification of octahedral tilting in perovskites was investigated by considering the possible tilting patterns coupled with the development of a standard notation to describe octahedral tilting distortions [31]. Glazer describes the cases where only two successive layers are considered. An alternative, but equally valid notation was developed by Aleksandrov [32]. In this work the Glazer notation will be used. The notation describes a tilt system by rotations of MX_6 octahedra about the three orthogonal axes, which are coincident with the three axes [100], [010], and [001] of the cubic aristotype perovskite. Glazer notation uses symbols of the type *a, b, c*. The letters in Glazer notation indicate the relative magnitude of the rotation of a corresponding axis, e.g., use of the letters *a*, *b*, and *c* imply tilts on the *x*, *y*, and *z* axes. These tilts are not necessary equal and the letters do not indicate the absolute magnitude of tilting relative to one another in increasing fashion (i.e., octahedral tilting designated by *b* is not necessarily larger than *a*). Matching letters indicate equal tilts on the different axes. A superscript on the letters is used to denote the phase of the octahedral tilting in neighboring layers. The superscript "+" would denote the neighboring octahedra tilt in the same direction (in phase) while the superscript "–" implies the tilts of neighboring octahedra tilt in the opposite direction (out of phase). A superscript of "0" signifies no tilting about that axis. Figure 2.1.1 shows the structures which correspond to tilt systems $a^0a^0c^+$ and $a^0a^0c^-$. The octahedral rotations in tilt systems $a^0a^0c^+$ and $a^0a^0c^-$ occur only on the *z* axis of the perovskite. The rotation of one octahedron causes the four adjacent octahedra in the same layer to rotate with the opposite direction in the same angle [19]. This figure shows clearly that rotation of a single octahedron defines the rotation of all octahedra in the same layer. However, lattice connectivity is such that rotations of the octahedra in the layer above and below are not geometrically constrained to the initial rotation and can tilt in the same ("+" superscript) or in the opposite ("-" superscript) direction with respect to the first octahedral layer [25].

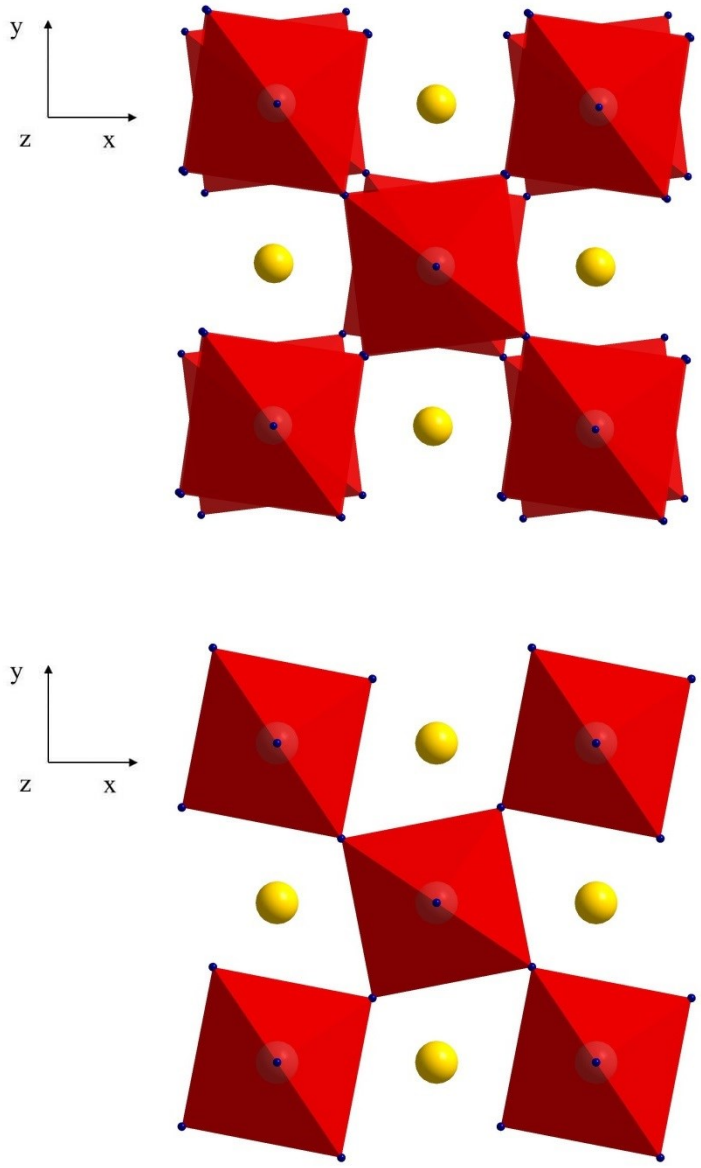

Figure 2.1.1. A view looking down the c axis of $a^0a^0c^-$ (top) and $a^0a^0c^+$ (bottom) with the A-site cations shown as yellow spheres and the *M*-site cations located in the center of the octahedra (red spheres).

Tilting of the octahedra reduces the symmetry of the undistorted perovskite tilt system $a^0a^0a^0$. Glazer derived 23 different tilt systems, leading to 15 different space groups as seen in table 2.1.1 [35]. Minor corrections to the space groups were published in updated descriptions [36, 37]. Considering in phase or out of phase tilting and the magnitude of the tilt angle, there are six basic component tilt systems ($a^+b^0c^0$, $a^-b^0c^0$, $a^0b^+c^0$, $a^0b^-c^0$, $a^0b^0c^+$, $a^0b^0c^-$). The tilt systems for perovskites are a linear combination of the six component tilts.

Considering a repeat pattern of no more than two neighboring octahedra decreased the number of possible tilt systems [35]. The different possible patterns are described by tilting vectors in a representation space. Using this approach, there are 15 tilt systems that can occur in real crystals, each with a different space group. The 15 tilt systems with the space group, degrees of freedom, number of Wyckoff sites for each ion and the estimated number of experimentally reported structures are shown for a single octahedral cation in Table 2.1. In 2001 Aleksandrov and Bartoleme published a review of octahedral tilting (distortions) in perovskites as well as perovskite-related structures [34]. The architecture and properties of perovskite crystals, including cation and anion deficient phases, was examined by Aleksandrov and Beznosikov [35]. Bock and Müller reported the group-subgroup relationships for derivatives of the perovskite structure type [36].

Table 2.1.1. The fifteen tilt systems, space groups, degrees of freedom, number of independent Wyckoff sites and number of observed structures reported for single octahedral cation perovskites with the restriction that not more than two layers show independent tilting.

Glazer Tilt System*	Space Group	Degrees of Freedom	Wyckoff Sites			Frequency of occurrence
			A	M	X	
Group A – High Symmetry Tilt Systems						
$a^0\,a^0\,a^0$ (23)	$Pm\bar{3}m$	1	1	1	1	21
$a^-\,a^-\,a^-$ (14)	$R\bar{3}c$	3	1	1	1	24
$a^0\,a^0\,c^-$ (22)	$I4/mcm$	3	1	1	2	9
$a^0\,a^0\,c^+$ (21)	$P4/mbm$	3	1	1	2	5
$a^0\,b^-\,b^-$ (20)	$Imma$	6	1	1	2	6
$a^-\,b^+\,a^-$ (10)	$Pnma$	10	1	1	2	119
Group B – Multiple A-Site Tilt Systems						
$a^+\,a^+\,a^+$ (3)	$Im\bar{3}$	3	2	1	1	22

cont.

$a^0 b^- c^+$ (17)	*Cmcm*	10	2	1	3	6
$a^0 b^+ b^+$ (16)	*I*4/*mmm*	5	3	1	2	0
$a^+ a^+ c^-$ (5)	$P4_2/nmc$	8	3	1	3	1
Group C – Transitional/Low Symmetry Tilt Systems						
$a^- a^- c^-$ (13)	*C*2/*c*	9	1	1	2	0
$a^0 b^- c^-$ (19)	*C*2/*m*	10	1	1	3	2
$a^- b^- c^-$ (12)	$P\bar{1}$	18	1	2	3	1
$a^+ b^- c^-$ (8)	$P2_1/m$	18	2	2	4	3
$a^+ b^+ c^+$ (1)	*Immm*	9	4	1	3	0

*The number in parentheses corresponds to the numbering of the tilt systems originally adopted by Glazer [24].

The distribution of tilt systems found in literature is shown in Table 2.1.1 with a total of 188 perovskites included [25]. The structures were mainly obtained from the earlier work of Woodward [37], but additions have been made being listed. Figure 2.1.2 accurately depicts the reported distribution of octahedral tilting (distortions) in perovskites at room temperature (excluding perovskites which contain multiple cations on the octahedral site). The perovskite structure can be divided into three groups as listed in Table 2.1.1; Group A are high symmetry tilt systems where all *A*-cation sites are crystallographically equivalent, group B are tilt systems with multiple crystallographic sites for the *A*-cations and group C are low symmetry/transitional tilt systems that are often observed as intermediates in a phase transition between two of the higher symmetry structures [25]. The octahedral tilting in groups A and B can be described using the notation of Zhao [37] by a single tilt where the tilting in $a^0a^0c^-$ corresponds to a single tilt φ about the cubic [001] direction, $a^0b^-b^-$ to a single tilt θ about the cubic [110] and $a^-a^-a^-$ to a tilt Φ about the cubic [111] or two tilts (e.g. $a^+ a^+ c^-$) at most. The majority of the perovskite structures belong to either group A or B, while structures that fall into group C are very rare. Therefore, it is not unusual that the most common mineral perovskite $CaTiO_3$ adopts a distorted structure, since distorted perovskites are far more common than undistorted cubic perovskites as seen in Figure 2.1.2.

In fact, the prevalence of the perovskite structure type can be directly attributed to the inherent ability of the corner-sharing octahedral framework to undergo cooperative octahedral tilting in response to the size mismatch between the A-cation and octahedral cations [25].

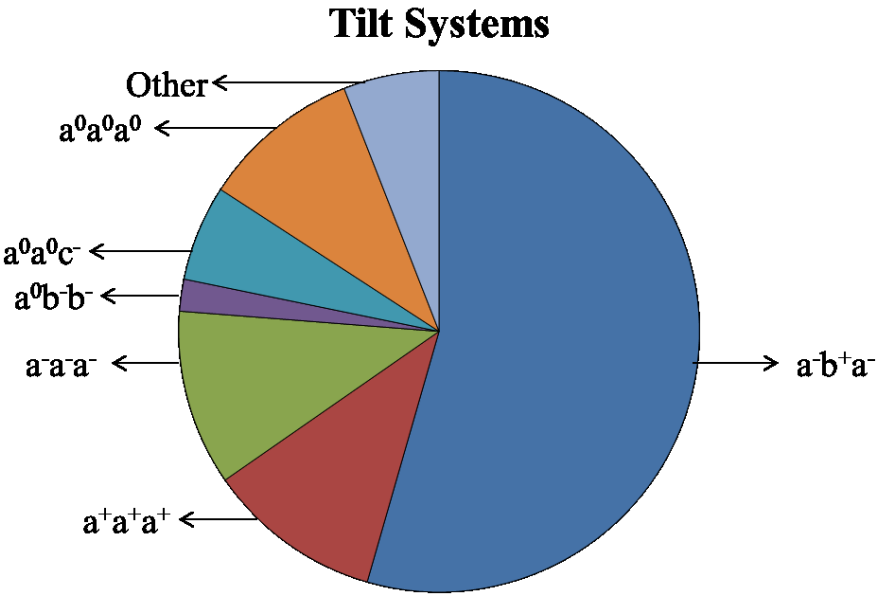

Figure 2.1.2. Distribution of tilt systems among known perovskites with a single octahedra *M*-cation [25].

The presence and magnitude of an octahedral tilting distortion affects not only the crystal structure, but also has a profound influence on a number of physical properties, such as electrical conductivity, magnetic super-exchange interactions, and various dielectric properties. For example, $Ln_{0.7}A_{0.3}MnO_3$ perovskites undergo a transition from a paramagnetic insulating state to a ferromagnetic metallic state upon cooling. Its magneto-resistance reaches a maximum value as the temperature approaches this transition temperature. Furthermore, it is known that the transition temperature can be tuned from 100 to below –200 °C by changing the magnitude of the octahedral tilting [39]. This remarkable sensitivity to this small structural distortion originates from the decrease in orbital overlap that occurs as the octahedral tilting increases [40, 41]. Another example of relation between the octahedral tilting and a physical property occurs in perovskites used for microwave dielectric applications. Colla *et al.* [42] have shown that the sign and magnitude of the temperature coefficient of the dielectric constant is quite sensitive to changes in the octahedral tilting distortion. From a technical standpoint, this has a major influence for the application of such materials.

2.2 Titania

Introduction

The commercial availability of titanium dioxide dates back to the early twentieth century [45]. Traditionally, the main use of titanium dioxide was as pigmentation for paints and plastics. In 1972 the photocatalytic activity of TiO_2 for water splitting was reported, known as the "Honda-Fujishima effect", which involves photocatalyzed electrolysis of water to generate hydrogen [46]. This material then became a focus of attention for many researchers and various promising applications were proposed, promoting TiO_2 to the front stage in selected energy-related technologies including photocatalysis, water splitting for production of hydrogen, sensing, photo-electrolysis, polymer-based bulk heterojunction photovoltaics, dye-sensitized solar cells (DSSC) and energy-storage devices such as Li-ion batteries [47, 48]. In dye-sensitized solar cells, which convert the solar energy into electrical energy, TiO_2 nanomaterials are coated with a dye that can absorb light in the visible range and rapidly inject the photo-excited electrons into the conduction band of TiO_2 [49]. The, these electrons travel through the TiO_2 layer to reach the back contact in the solar cell. Dye-sensitized solar-cells have high efficiency values (up to 11%) in conversion of solar energy to electrical energy [49, 50]. Surface-modified TiO_2 nanomaterials with super-hydrophilic or super-hydrophobic nature are currently used for antifogging mirrors, glasses and eyeglasses, as well as for self-cleaning or stain-proof surfaces such as self-cleaning paints. In addition, TiO2 nanostructures are considered promising for environmentally-benign photocatalytic applications against pollutants such as methyl-mercaptane [45]. TiO_2 nanotube arrays can be employed in the same applications as other TiO2 nanostructures. In addition, the nano-tubular assembly provides a preferred dimensionality to the devices, for instance, when their vertically aligned arrays provide a direction for the charge transfer toward the electrode [51]. Further, the controllable uniform top openings of these nanotubes make them appropriate for the size selective applications such as filters or as templates for fabrication of other materials. Additionally, the well-defined and regular inner volume of the nanotubes is beneficial as nano-test-tubes, for instance in fluorescence immunoassay which is a sensitive technique to measure the concentration of many compounds including drugs, hormones and proteins. [52]

Polymorphs and crystal structures

Titanium dioxide (titania) is a transition metal oxide that exists in various crystalline polymorphs (as well as one amorphous state). The most common polymorphs of TiO_2 in nature are rutile, anatase and brookite [53, 54]. Rutile is the most stable form of titanium dioxide (up to 60 kbar) and can form under high temperature and high pressure conditions. [57]. Brookite is typically not found as a pure phase in nature and usually contains some rutile or anatase as second phase. Its technical and scientific value is overall very small [53, 55, 56, 62]. Figure 2.2.1 provides schematic representations of the crystal structure of TiO_2 in these two common polymorphs, anatase and rutile. Both, rutile and anatase have a tetragonal crystal structure with unit cells containing six and twelve atoms, respectively. Titanium atoms are coordinated by six oxygen atoms to form distorted TiO_6 octahedra. In rutile, the octahedra share two edges whilst in anatase the octahedra share four edges. The distortion of the TiO_6 octahedra is more significant in anatase than in the rutile structure [58, 59, 62].

Table 2.2.1. Lattice and structural information of anatase and rutile, two common polymorphs of TiO_2. [53, 63]

	Anatase	Rutile
Crystal lattice/space group	Tetragonal $I4_1/amd$ (No. 141)	Tetragonal $P4_2/mnm$ (No. 136)
Lattice Parameters [Å]	$a = 3.78$	$a = 4.59$
	$c = 9.52$	$c = 2.96$
Volume [$Å^3$]	34.06	31.22
Formula unit Z	4	2
Density [g/cm^3]	3.79	4.13

The lattice parameters and structural information of anatase and rutile are summarized in Table 2.2.1.

It is reported that after reaching a specific particle size of > 14 nm, the anatase structure transforms into the more stable rutile phase reflecting the lower surface energy of rutile for larger particle sizes [60, 61, 62].

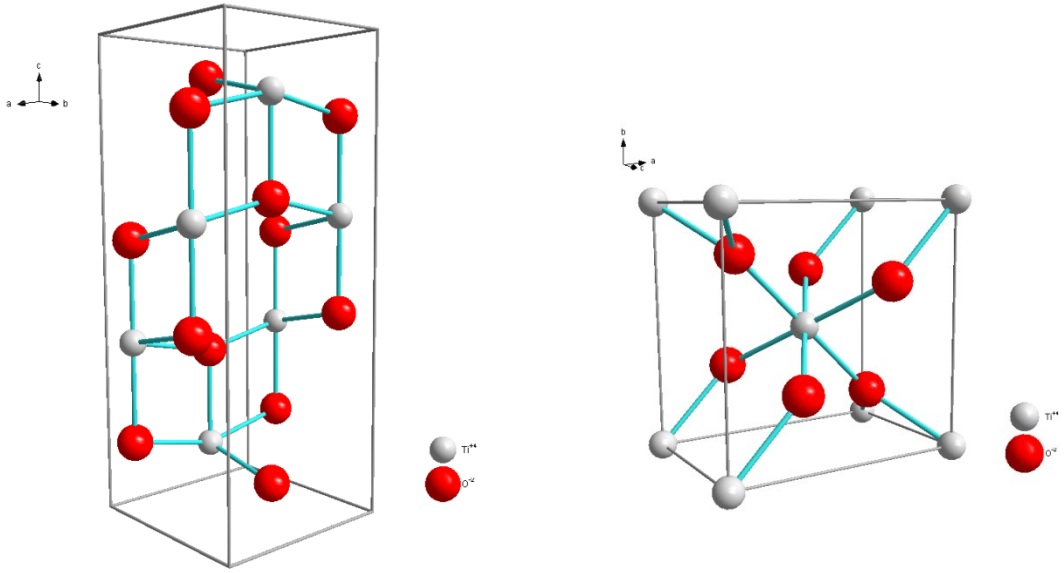

Figure 2.2.1. Unit cell of TiO_2 in the form of the anatase (left) and rutile (right) structure; where the grey spheres represent Ti^{4+} and the red spheres

Many transition metal oxides are non-stoichiometric (defective) when synthesized under typical processing conditions. [64] Crystal structures of TiO_2 may contain bulk and surface structural defects such as oxygen vacancies or interstitial titanium [65, 66]. Oxygen vacancies are the most common defect in TiO_2 [67], and are slightly more energetically favorable in anatase than in rutile, while Ti interstitials form more easily in rutile than in the anatase structure. TiO_2 can lose oxygen and become oxygen-deficient via the following reaction [62, 64],

$$TiO_2 \rightleftharpoons TiO_{2-\delta} + \frac{1}{2}(\delta)O_2 \qquad (2)$$

in which δ is the deviation from stoichiometry. Structural defects can influence the electronic structure, charge transport and surface properties of TiO_2-based materials as will be explained in detail in the further subchapters.

Electronic properties

Semiconducting and transport properties

TiO_2 is a wide-band-gap semiconductor and a promising candidate for photocatalysis due to its low cost, chemical inertness and non-toxicity. The anatase band-gap energy is E_g = 3.2 eV – 3.3 eV, corresponding to absorption wavelengths of 376 – 380 nm, and that of rutile is E_g = 3.0 to 3.1 eV, which corresponds to absorption wavelengths of 400 to 410 nm [53]. These wavelengths are located within the ultraviolet (UV) range of (sun)light [53, 60, 62]. When TiO_2 receives the appropriate radiation corresponding to its bandgap energy, an electron is excited from the valence band to the conduction band whereby generating electron-hole pairs. The generation of charge carriers, i.e. electrons and holes, is important for the operation of many semiconductor devices and photocatalysts, as they will be involved in the catalytic reactions. For example photo-generated holes that are produced on TiO_2 surfaces have strong oxidizing power oxidize carbon monoxide to carbon dioxide [62]. However, these photogenerated pairs may be destroyed by recombination and no longer react with nearby molecules. The catalytic functionality of TiO_2 is activated when some of these electron-hole pairs persist with appreciable lifetime to achieve charge separation and then diffuse to the surface of TiO_2 to initiate redox reactions such as decomposition of an organic compound into its constituents. The electrons and holes that reach the surface of TiO_2 without recombination can reduce and oxidize the adsorbed reactants, respectively [68]. The semiconducting properties of TiO_2 nanostructures can facilitate photocatalyzed reactions, for instance, to produce hydrogen fuel from water. During hydrogen production from water, the energy level of the semiconductor's conduction band should be more negative than the energy level of hydrogen production (i.e. $E_{\mathrm{H_2}}/E_{\mathrm{H_2O}}$, as shown in Figure 2.2.2) and the energy level of the semiconductor valence band should be more positive than the energy level for water oxidation (i.e. $E_{\mathrm{O_2}}/E_{\mathrm{H_2O}}$, as shown in the same Figure 2.2.2).

The energy levels of TiO_2 satisfy these criteria for hydrogen production [62, 68, 69].

$$TiO_2 \xrightarrow{hv} e^-_{TiO_2} + h^+_{TiO_2} \quad (3)$$

$$2h^+ + H_2O \rightarrow \frac{1}{2}O_2 + 2H^+ \quad (4)$$

$$2e^- + 2H^+ \rightarrow H_2 \quad (5)$$

And the overall reaction is: $H_2O + hv \xrightarrow{TiO_2} \frac{1}{2}O_2 + H_2$ (6)

where *h* is the Plank's constant and *v* the wavelength of irradiated light. However, the photocatalytic efficiency of TiO_2 (defined as the ratio of change of reactant in concentration per unit time divided by the total incident light flux from the source) is generally low [62, 68, 70].

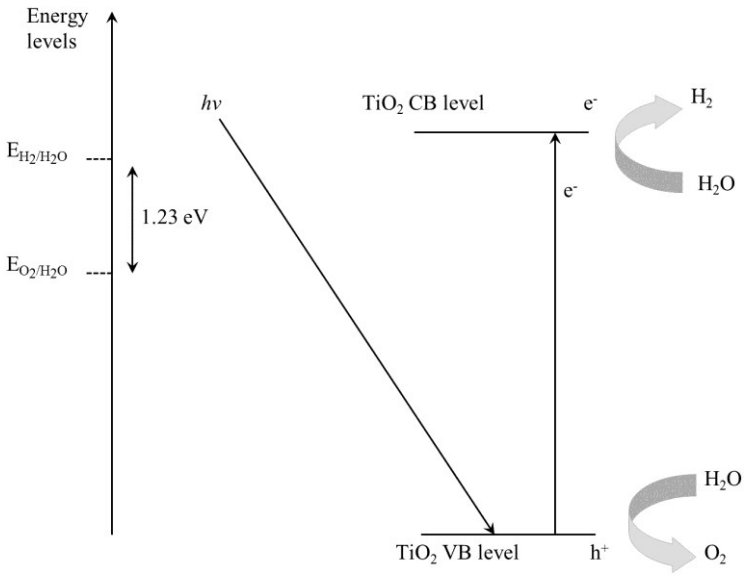

Figure 2.2.2. The photocatalytic water splitting process generates hydrogen using TiO_2. The energy schemata (CB: conduction band; VB: valence band) are shown with their corresponding reactions [68].

Electrons in the conduction band can very quickly recombine with holes in valence band and release energy in form of heat or photons before they can diffuse and reach the surface of TiO_2. In pure rutile TiO_2 the lifetime of an electron-hole pair is ~30 ns (Table 2.2.2) [62, 71].

Table 2.2.2. Primary processes in photocatalysis and the associated characteristic time domains for TiO_2 [71].

Primary Process	**Characteristic Time Domains**
electron-hole generations	fs (very fast)
electron-hole trapping	0.1 ns – 10 ns (fast)
electron-hole recombination	10 ns – 100 ns (slow)
interfacial charge transfer	100 ns (slow) – ms (very slow)

Visible light comprises ~ 50 % of the solar spectrum. However, the band-gap of rutile TiO_2 (E_g = 3.0 eV) corresponds to the energy of UV light which only accounts for ~ 6 % of the solar spectrum [72]. Therefore, only a small portion of the solar energy can be used to activate TiO_2 for initiating the catalytic reactions. The electronic structure of rutileTiO_2, such as the band-gap, can be engineered by controlled doping of this material. Figure 2.2.3 shows as an example a schematic representation of the bandgap of pure and Fe-doped rutile. Depending on the type of dopant (p- or n-type), intermediate energy levels may form above the valence band or below the conduction band of TiO_2, and thus narrowing the band-gap [62].

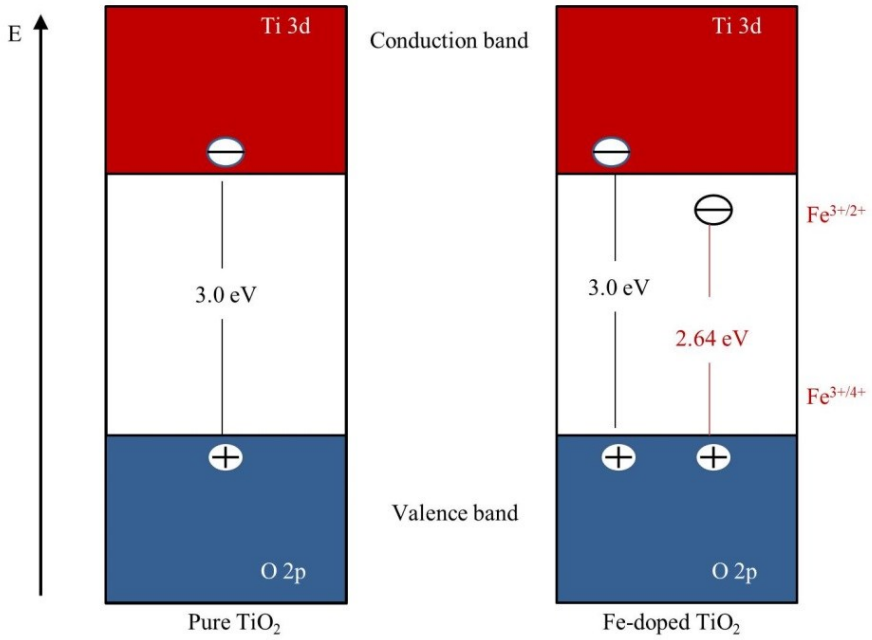

Figure 2.2.3. Schematic representation of the band-gap of pure (left) and Fe-doped TiO_2 (right).The dopant forms an intermediate energy level below the conduction band which reduces the band-gap [62].

In general, the main purpose of doping TiO_2 with other elements, including transition metals such as Fe, is to modify the catalytic properties of titania-based structures. An example would be the band-gap engineering or modifying of the electron-hole recombination rate [62, 73 – 75]. In Fe-doped TiO_2, Fe^{3+} ions may act as both electron and hole traps and transform to Fe^{2+} or Fe^{4+} [73]. Both of are less stable than the Fe^{3+} ions and thus can easily release the trapped charges and transform back to Fe^{3+}. In this manner, the electron-hole pairs may reach the surface of TiO_2 without recombining. Another purpose of doping TiO_2 (or other metal oxide semiconductors) with transition metals is to introduce magnetic moments into its structure.

Magnetic properties

TiO_2 has the electronic configuration of a noble gas and thus is expected to exhibit diamagnetic behavior [76]. However, a range of positive and negative values of magnetic susceptibilities are reported for rutile type TiO_2 ranging from χ_v = (– 0.024 to + 0.029). The difference in the values of magnetic susceptibility reported for rutile is attributed to the presence of adsorbed oxygen and iron impurities, which can act as paramagnetic species [76].

Further, although stoichiometric TiO_2 contains mostly Ti^{4+} ions and is considered to be non-magnetic, positive temperature-dependent value of magnetic susceptibility is reported for the anatase type TiO_2 if it has an oxygen deficient structure [76, 77]. The presence of ferromagnetism in pure titanium dioxide nanostructures and other metal oxides is reported by various sources [78, 79]. The origin of this type of magnetism is still under debate and is mostly attributed to the creation of structural defects such as oxygen vacancies, which can be a reversible process [79]. In 1972, Danley and Mulay studied the magnetic behavior of non-stoichiometric titanium dioxide (Ti_nO_{2n-1}) and reported a field independent (but temperature-dependent), magnetic susceptibility of these structures [80]. Yoon *et al.* fabricated dopant-free thin films of magnetic TiO_2 with a reproducible saturation moment. The thin TiO_2 film was fabricated in an oxygen-deficient environment and anionic defects were introduced into the film structure by controlling the Ti – O atomic ratio [76, 84]. Alivov *et al.* studied the magnetic properties of nominally-pure anatase, rutile and amorphous TiO_2 nanotube arrays with different pore size diameters of 40 to 160 nm [62, 84]. They observed similar paramagnetic behavior for all the nanotubes within the temperature range of 1.8 to 300 K, regardless of their diameter. Apart from pure TiO_2, magnetic properties of transition metal-doped TiO_2 nanostructures have also been studied, including Mn-, V-, Co- and La-doped TiO_2 powder [84], Cu-doped rutile thin film [86] and Co- and Cr-doped TiO_2 nanorods [87]. Effects of the annealing temperature, annealing atmosphere and structural defects are evaluated on these doped materials. In addition, several groups have studied the magnetism in Fe-doped TiO_2 in form of thin films 44], nanoparticles [79 – 91], nano-rods [92] and nanotube arrays [93]. However, the amount of research on pure and doped single crystal TiO_2 is still fairly limited [62].

2.3 Zirconia

Introduction

Zirconia (i.e. cubic stabilized zirconium dioxide), is a man-made mineral. Zirconia is widely used as a diamond substitute, since it is visually flawless and has a colorless state. It is therefore often referred to as the "cheap man's diamond". However, zirconia has also a variety of properties that makes them suitable for technical applications. Its chemical and mechanical stability makes it suitable as refractory material. Additionally, cubic zirconia features certain electrochemical properties like oxygen ion conduction, which can be applied for e.g. solid state fuel cells. ZrO_2 was discovered in 1892 in its monoclinic form, the yellowish mineral called Baddeleyite [94]. However, it had little economic importance. In 1899, mineralogists discovered a naturally occurring form of cubic zirconia as microscopic grains [95]. Growing cubic zirconia artificially was a challenge due to its high melting point of approximately 2750 °C. No existing crucible could hold cubic zirconia at its molten state. In the 1960s french scientists began investigating single crystal growth of cubic zirconia. However, the process only created small crystals. Soviet scientists later picked up this research and perfected the technique. This discovery was published in 1973, which helped producing cubic zirconia on an industrial level. This process is called induction-Skull melting technique and will be presented in Chapter 2.5 in more detail.

The polymorphs of zirconia

At atmospheric pressure, pure zirconia exists as cubic, tetragonal and monoclinic phase. At pressures above ~ 3.5 GPa, several orthorhombic phases are formed, which will not be discussed further.

Monoclinic phase

The monoclinic phase (m-ZrO_2) is thermodynamically stable at temperatures below approximately 1100 °C. The unit cell can be described as a distorted cubic cell, although the structure is significantly more complex than that of the cubic or tetragonal phases (Figure 2.3.1) [94-96]. Each zirconium atom is coordinated by 7 oxygen atoms, with bond lengths from 2.04 to 2.26 Å, and with varying O-Zr-O bond angles. The oxygen atoms are arranged in two parallel (100) planes, separated by layers of zirconium atoms [94].

The structure can be described using the space group $P2_1/c$ (No. 14). The unit cell parameters at room temperature vary somewhat between different literature sources [94 – 99].

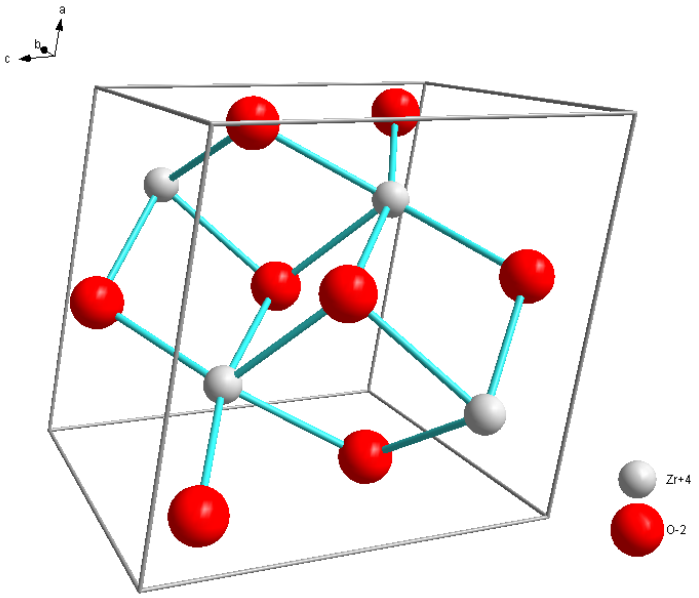

Figure 2.3.1. Monoclinic unit cell of ZrO_2. The red spheres represent oxygen and the white ones zirconium ions.

Tetragonal phase

The tetragonal phase, t-ZrO_2, is thermodynamically stable from 1100 to 2380 °C. It has, with respect to the cubic phase, a distortion in the lattice, corresponding to a slight elongation along the *c*-axis and a displacement of columns of oxygen atoms, alternately up or down the *c* axis [96]. The result is the movement of four oxygen neighbors closer to the zirconium atom, and the other four oxygen neighbors away from it, respectively (Figure 2.3.2). These interdependent distortions are required to prevent O-O contact [96, 100]. Each zirconium atom maintains its coordination of oxygen with four oxygen atoms at a distance of ~ 2.1 Å and four at a distance of ~ 2.3 Å. The space group is $P4_2/nmc$ (No. 137). The tetragonal phase can also be indexed to a higher symmetry, as a so called "supercell", $P\bar{4}m2$ (No.115). This "supercell" has a parallel *c* axis and the same value of *c* as the primitive unit cell. The *a* and *b* axes are rotated at 45° with respect to the primitive unit cell. The "supercell" is a useful tool for the description of phase transformations and the comparison of the structures, as its axes are parallel to those of the cubic *fcc* fluorite cell, and almost parallel to those of the monoclinic cell. The *c/a* value is usually calculated also by using the $P\bar{4}m2$ unit cell.

The zirconium atoms are fixed with respect to their unit cell positions, while the position of the oxygen atoms in the *c*-axis can vary. The displacement of the oxygen atoms along the *c* axis can be defined as $\delta = 1/4 - z$ with respect to the cubic phase (where position is z = 1/4) [96, 100]. The values of *z* and the lattice parameters *a* and *c* vary with temperature and chemical composition.

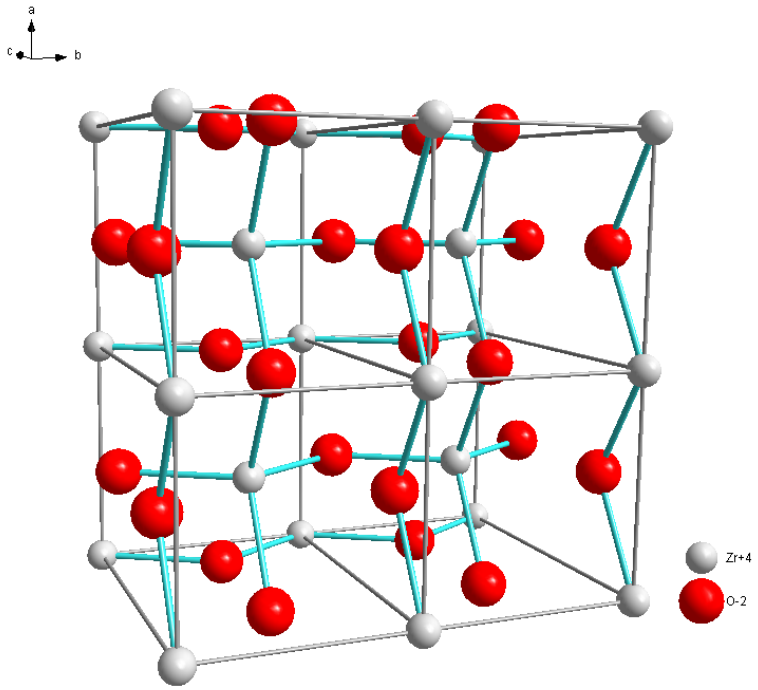

Figure 2.3.2. Tetragonal unit cell of ZrO_2, shown as a 2x2 "supercell". The red spheres represent oxygen and the white ones zirconium ions.

Cubic phase

The cubic phase, c-ZrO2, is stable from 2380 °C up to the melting point at 2750 °C [101]. The structure has the fluorite (CaF_2) structure, in which each zirconium atom is coordinated, with the same distance, by 8 oxygen atoms. This can be visualized by cations occupying fcc positions in a cubic lattice, with eight interstitial oxygen atoms and a large vacancy in the center (Figure 2.3.3). The space group of this structure is $Fm\bar{3}m$ (No. 225), with Zr located at the position 0,0,0 and O at 1/4,1/4,1/4, respectively [96, 99].

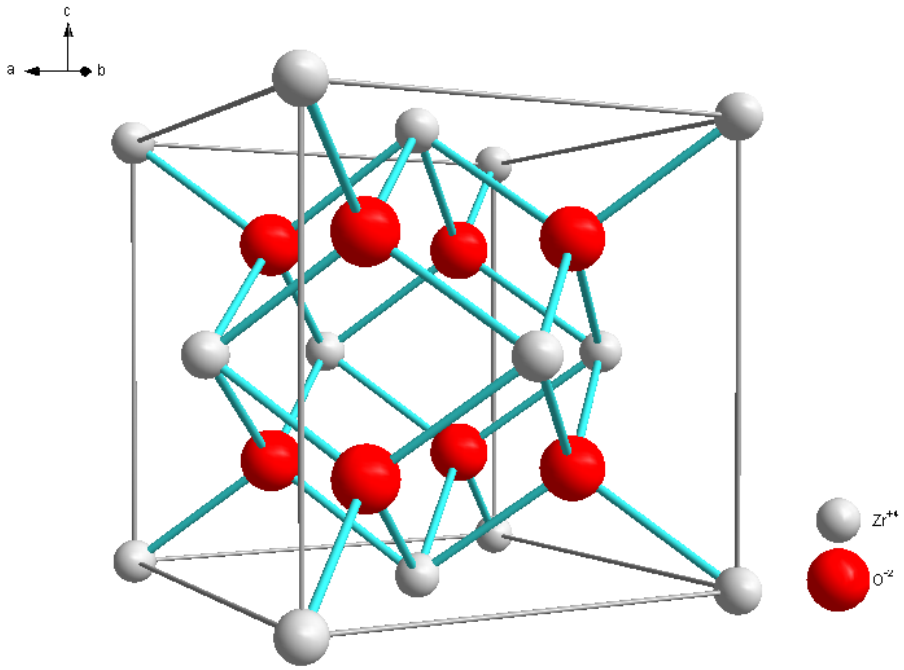

Figure 2.3.3. Cubic unit cell of ZrO_2. The red spheres represent oxygen and the white ones zirconium ions.

Phase stabilization

It is well known that the substitution of certain other oxides into ZrO_2 will drastically alter the relative stability of the phases [96, 100, 108, 109]. The transformation temperatures are lowered, with the result that the tetragonal or cubic phases may become stable (or metastable) at room temperature. These oxides are usually of di- or trivalent metals, such as Y_2O_3, CaO, MgO, or lanthanide oxides. Zirconia that is "partially stabilized" (containing a mixture of phases), is an important engineering ceramic with a high mechanical toughness and chemical stability. The toughness is derived from the transformation of the "metastable" tetragonal phase into the monoclinic phase, which is accompanied by an increase in volume ("transformation toughening"). This mechanism will be explained in more detail in the following subchapter. The stabilization is generally associated with the presence of oxygen vacancies in the lattice [96, 100, 110]. These are created to balance the charge of the di- or trivalent cations, which are substituted on the Zr^{4+} sites. The anion vacancy sites are positively charged, so that neighboring oxygen anions move closer to the vacancy and cations are displaced outwards, which permits a relaxation of the lattice structure. Other critical factors include the size of the stabilizing cation [96, 100, 108, 113, 114].

The tetragonal to monoclinic (t → m) phase transformation

The rapid transformation from the tetragonal phase to the monoclinic phase (t → m) involves a significant volume increase (~3.5 %) [115], which has practical importance to zirconia ceramics. The expansion causes considerable cracking in dense zirconia when it is cooled below the transition temperature. The transformation, and the subsequential increase in volume plays a central role in the above mentioned "transformation toughening" of partially stabilized zirconia [96, 100, 110]. The nature of the t → m transformation is dominated by two main characteristics: the sharp change in volume, and the martensitic character [96, 100]. An ~ 3% increase in volume occurs with the t → m transformation, equivalent with an decrease in density from 6.10 g/cm^3 to 5.83 g/cm^3 [99]. The transformation also has a martensitic character, which are rapid, diffusionless and displacive. Furthermore, they are highly dependent on nucleation kinetics [117, 119]. Both, the volume change and the martensitic character contribute towards the sensitivity of the transformation to mechanical stress. First, the density difference between the phases allows stress to affect their relative thermodynamic stability. Hence, compressive stress will decrease the thermodynamic t ↔ m transformation temperature [99]. Second, the rapid and displacive nature of the martensitic transformation means that the kinetics are dominated by nucleation, which is also strongly affected by stress [96, 109, 116]. This causes a temperature hysteresis in the transformation, generally in the range of 100 °C to 200 °C. The effect of stress can be clearly seen by the stabilization of tetragonal particles in a constraining matrix [120 – 122]. Table 2.3.1 lists the transformation temperatures of m → t from various literature sources.

Table 2.3.1. Reported transformation temperatures between the monoclinic and tetragonal phases of ZrO_2.

	Transformation temperature (°C)	
Reference	m → t (heating)	t → m (cooling)
Frey *et al.* [118]	800 - 1150 (stage 1) 1150 - 1400 (stage 2)	1020 – 870
Garvie *et al*. [124]	1160 - 1190	1100 – 1020
Perry *et al.* [125]	1070 - 1150	1000 – 950
Osiko *et al.* [126]	1030 - 1130	1000 – 890
Patil *et al.* [115]	930 - 1100 (stage 1) 1100 - 1220 (stage 2)	1020 – 700

Garvie *et al.* have presented evidence that the crystal size will also affect the temperature at which the transformation takes place [123]. These factors make it difficult to define a temperature for the transformation which results in a wide variety of reported temperatures for both the t → m and m → t transformations. Several of these temperatures are shown in Table 2.3.1. On cooling, the t → m transformation occurs between approximately 1100 °C and 950 °C, while the reverse m → t transformation occurs during heating between approximately 1050 °C and 1175 °C. Differences have also been observed between the t → m and m → t transformation, with evidence presented that the latter is composed of two distinct stages [115, 118]. Twinning is commonly observed in monoclinic crystals that have undergone a transformation from the tetragonal phase [127 – 129]. The details of the crystallographic changes during the transformation have been thoroughly reported [117, 127, 128] and will not be discussed here. There have been many attempts to formulate theoretical models to interpret these observations. The simplest approach is to define a temperature M_s, at which the martensitic transformation starts during cooling [127]. The observation that this temperature is highly dependent on a range of conditions, as discussed above, has driven the development of more complex models. A number of these models propose the existence of monoclinic or transitional-structure "nuclei" in the tetragonal matrix [129 – 135]. However, there is no scientific consensus about this model [126].

2.4 Luminescence

Introduction

Luminescence is a topic always closely related to spectroscopy, which is the study of the general laws of absorption and emission of radiation by matter [136]. The existence of luminous organisms such as bacteria in the sea and in decaying organic matter, glow worms and fireflies have mystified and thrilled man since time immemorial. A systematic scientific study of the subject of luminescence is of recent origin, from the middle of nineteenth century. In 1852 G. C. Stokes identified this phenomenon and formulated his law of luminescence now known as Stoke's law [137], which states that the wavelength of the emitted light is greater than that of the exciting radiation. E. Wiedemann introduced the term 'luminescence' (weak glow) into the literature in 1888 [138]. The phenomenon of certain kinds of substance emitting light on absorbing various energies without heat generation is called luminescence. Luminescence is obtained under a variety of excitation sources [138]. The wavelength of emitted light is characteristic for the luminescent substance and not of the incident radiation [139]. The various types of luminescence phenomena are given their classification based on the type of radiation used to excite the emission (Table 2.4.1) [140].

Table 2.4.1. The "types" of luminescence phenomena and excitations [140].

Luminescence "types"	**Excitation methods**
Photoluminescence	Light / photons
Bioluminescence	Biochemical energy
Sonoluminescence	Sound waves
Electroluminescence	Electric field
Chemiluminescence	Chemical energy
Triboluminescence	Mechanical energy
Cathodoluminescence	Electrons / cathode radiation
Radioluminescence	Nuclear / Ionizing radiation
Fluorescence	Ionizing radiation; UV / visible light
Phosphorescence	
Thermoluminescence	

The last three phenomena are linked together since the time scale over which the light emission takes place lies in the same range. Fluorescence is a luminescent process, which persists only as long as an excitation takes place. The decay time of fluorescence is independent of temperature; it is determined by the probability of transition from the excited state to the ground state. Phosphorescence is luminescence observable after the removal of the exciting source. The decay time is temperature dependent. Substances emitting luminescence are called “luminophors” or phosphors. The study of luminescent materials in the form of polycrystalline, single crystalline and glass phosphors are reported [139]. Most phosphors can be basically described as semiconductors, in terms of the energy band model, with valence and conduction band, and with localized energy levels in the forbidden regions between the bands. The localized centers are associated with the impurities (dopants) or defects in the host lattice. Impurities that provide levels, which permit radiative transitions, are called activators. Generally the levels that are close to the valence band can also act as traps for valence band hole, when occupied by electrons [140]. Impurities can bring the levels close to that of the conduction bands, which if empty, may act as electron traps. Typical excitation mechanisms of luminescence involve raising an electron from a filled band or from a filled activator level to the conduction band. Alternatively, an electron can also be raised from an activator ground level to a higher activator level. Those electrons that reach the conduction bands can either return to activator level or can be trapped [140]. In the case that the electron is trapped it can return to the conduction band by absorbing sufficient energy (e.g. thermal energy). The return of an electron from the conduction band to an empty activator level yields to luminescence. Transition with the lack of radiation may also occur to trapped or free holes in which energy is transferred to lattice in the form of phonons [137]. The system consisting of activator impurity and surrounding disturbed host lattice, where these transitions take place, is known as “luminescence center”. Radiations from the transitions of an excited to a ground state of the activator that produces fluorescence with a delayed return of the electron from a trap through the conduction bands results in phosphorescence. Phosphorescence can be “frozen” at low temperatures in such a way that thermal energy is not sufficient for the release of trapped electrons. Thermoluminescence (TL) is the release of such “frozen” phosphorescence by temperature rising. It is also known as thermally stimulated luminescence (TSL) or thermally stimulated relaxation [139].

Photoluminescence

Luminescence in solids is the phenomenon in which electronic states of solids are excited by some form of external energy and the excited energy is released as light [137]. When the energy arises from short wavelength light, the process is known as photoluminescence (PL). In this case a molecule absorbs light of a certain wavelength λ_1, decays to a lower energy state and then emits light of wavelength λ_2 as it continues to decay, in a radiative manner, to its electronic ground state. Generally, the wavelength of emission λ_2 is longer and has therefore a lower energy, than the excitation wavelength. Luminescence bands can be either fluorescence or phosphorescence depending on the average lifetime of the excited state which is longer for phosphorescence than fluorescence [140]. The relative broadness of the emission band is related to the relative distance between the excited emitting state and the electronic ground state in equilibrium [138]. PL of a molecular species is different from emission from an atomic species [140]. In the case of atomic emission both the excitation and emission have the same wavelengths. This is in contrast to the excitation of a molecular species, where an emission has usually a longer wavelength than the excitation wavelength. PL can occur in gas, liquid and solid phases [140]. An energy level diagram, as seen Figure 2.4.1, shows the radiative and non-radiative transitions that lead to the observation of molecular photoluminescence. The spin multiplicities of a given electronic state can either a singlet (paired electrons) or a triplet (unpaired electrons). The electronic ground state is normally a singlet state and is described as S_0 [140]. Excited electronic states can either be singlet (S_1, S_2) or triplet (T_1). When a molecule absorbs light of a certain energy an electron is elevated within $10^{-14} – 10^{-15}$ s, from the ground electronic state to an excited state that possess the same spin multiplicity as the ground state. An exception is a triplet-excited state as the final state of electronic absorption since the selection rules for electronic transitions dictates that the spin state should be maintained upon excitation. An abundance of radiative and non-radiative processes usually occur after the absorption of light until the observation of molecular luminescence [140].

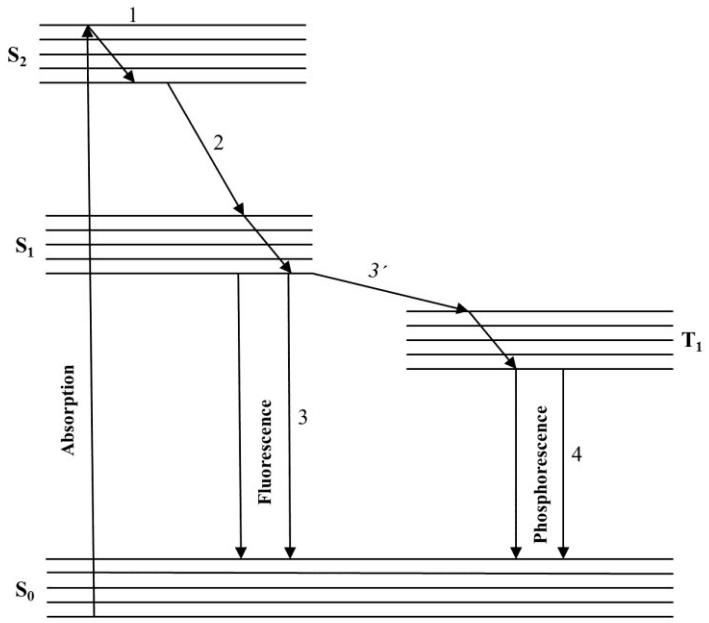

Figure 2.4.1. Energy states diagram of the fluorescent and phosphorescent process, where S_0 is the electronic ground state, S_1 and S_2 are singlet states and T_1 the triplet states A molecule absorbs light of a certain energy and an electron is excited from the electronic ground (S_0) to an excited state (S_1 and S_2). The electron sinks gradually to the electronic ground state while releasing the surplus energy in form of light. [140].

Non-radiative relaxation processes

(a) Vibrational relaxation:

Excitation usually leads to higher vibrational level of the excited state. However, the excited molecules normally relax very rapidly to the lowest vibrational level of the excited electronic state. These non-radiative processes are known as vibrational relaxation. The occurrence lies between 10^{-14} and 10^{-12} s, which is much shorter than the typical luminescence lifetime. These processes occur prior to the actual luminescence.

(b) Internal conversion:

If the molecule is excited to a higher energy excited singlet state than S_1 (like S_2 in Figure 2.4.1), a rapid non-radiative relaxation usually occurs to the lowest excited singlet energy state (S_1).

Relaxation processes between electronic states with the same spin multiplicity such as S_1 and S_2 are called internal conversion. Normally, the occurrence is after the vibrational relaxation (approx. at a time scale of 10^{-12} s)

(c) Intersystem crossing:

Non-radiative relaxation processes can also occur between excited states of different spin multiplicity. Such relaxation process is known as intersystem crossing. The relaxation from S_1 to T_1 in Figure 2.4.1 is such an example. This effect can occur at the same time scale as the internal conversion.

(d) Non-radiative de-excitation:

The mentioned non-radiative processes occur very rapidly and release only a small amount of energy. The rest of the energy is either exhausted by emission of photons or by the release of thermal energy. This non-radiative release of excitation energy which results in the decay of the excited molecule to the electronic ground state is called non-radiative de-excitation. However, the amount of energy released in the form of heat is usually very small [140, 145].

Radiative processes

(a) Fluorescence

Fluorescence refers to the emission of light associated with a radiative transition from an excited electronic state with the same spin multiplicity as the ground electronic state. Fluorescence transitions occur very rapidly and average lifetimes of the excited states are typically in the range of 10^{-6} s. Electronic transitions between states of different spin multiplicity are normally forbidden. However, the probability increases when the so called spin orbit coupling increases. This occurs through a combination of excited singlet (like S_1 and S_2) and triplet states (like T_1). This “mixing” removes the spin forbidden nature of the transitions between pure singlet and pure triplet states [140]. Therefore, if this intersystem crossing is populating the triplet excited state then luminescence can occur from the triplet state to the electronic ground state.

(b) Phosphorescence

Phosphorescence refers to the emission of light associated with a radiative transition from an electronic state that has a different spin multiplicity from that of ground electronic state. Since phosphorescence transitions are spin forbidden they occur slowly resulting in an average lifetime from 10^{-6} s to several seconds. Phosphorescence is also known as "delayed fluorescence".

Mott-Seitz model of luminescence

Most of the luminescent solid materials exhibit broad curved absorption bands as well as emission bands which correspond to larger wavelengths/smaller energies. Various luminescent spectra models for rare earth elements were suggested over the time to explain the presence or absence of luminescence. The 1-dimensional configuration-curve (CC) of the Mott-Seitz model is the most accepted among them (Figure 2.4.2) [137, 140].

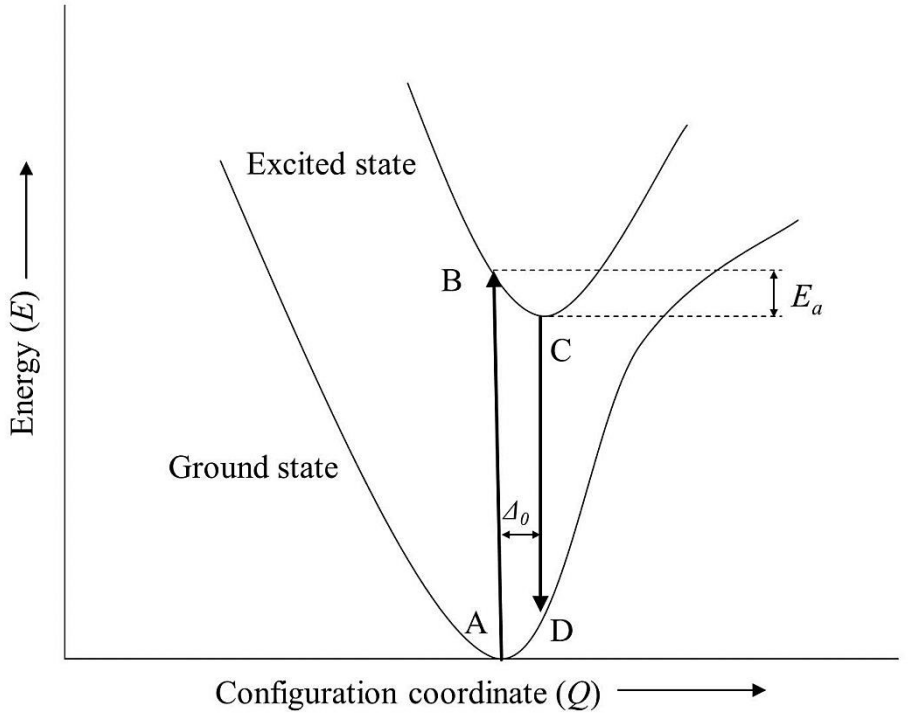

Figure 2.4.2. Schematic configuration coordinate energy diagram of rare earth elements for the ground and the first excited state. Δ_0 is the relative displacement of the excited potential well compared to the ground state and E_a is the so called Stoke-shift [137, 140].

The total potential energy of the luminescent center E is plotted against the configuration-coordinate Q for ground and excited states. The configuration-coordinate represents the distance between the rare earth ions and their surrounding cations. The absorption of light with a certain energy value causes a transition from point A to point B. The lifetime of the excited state is in the order of 10^{-8} s which is longer than the average thermal lattice vibration period. The thermal vibration causes the ions to occupy different (lower) energy levels inside the parabola curve of the excited energy state (point C). The difference between the lowest energy regions of the ground and the excited state is the displacement Δ_0. Due to this displacement, the absorbed photon has a slightly higher energy than the emitted photon (point D). The difference in energy is called the Stoke-shift.

Kinetics of Luminescence

There are two kinds of luminescence processes which can be distinguished in kinetics of first (mono-molecular mechanism) second order (bi-molecular mechanism).

First order kinetics

According to a constant probability Law, the number of excited electrons N decreases as seen in Eq. 7

$$\frac{\mathrm{d}N}{N} = -a\mathrm{d}t \tag{7}$$

Where a is the decay constant. With originally N_0 electrons the equation can be written as follows:

$$N = N_0 \cdot e^{-at} \tag{8}$$

Since the luminescence intensity I is:

$$I \propto \frac{\mathrm{d}N}{N} \tag{9}$$

Equation 8 can be written as such:

$$I = I_0 \cdot e^{-at} \tag{10}$$

The major characteristic is the lifetime t, which is the average stay of an ion in a given excited state [140].

Second order kinetics

In this case the probability for recombination is proportional to the number of centers [140].

$$\frac{\mathrm{d}N}{N} = -aN\mathrm{d}t \tag{11}$$

Where *N* is:

$$N = \frac{N_0}{(1+N_0 at)} \tag{12}$$

Therefore *N* has a hyperbolically decrease over time.

Since the luminescence intensity is:

$$I \propto \frac{\mathrm{d}N}{\mathrm{d}t} \tag{13}$$

Eq. 11 and 13 can be written as such:

$$I = -aN^2 \tag{14}$$

$$I = \frac{I_0}{(1+\sigma t)^2} \tag{15}$$

Where:

$$\sigma = (I_0 a)^{1/2} \tag{16}$$

The increase in decay is proportional to the increase of the excitation intensity. The above kinetics can be applied only if the optical transition is associated to dipole radiation or the lifetime of approximately 10^{-8} s. In the case of phosphorescence the kinetics involved in the process depends on the spatial relation between luminescence centers and the motion of conduction electrons. Therefore, the glow is longer at lower temperatures and shorter at higher temperatures showing the strong dependence of phosphorescence on temperature [140].

Decay mechanisms

In order to explain the mechanisms of decay different methods were presented [136 – 140].

Simple exponential decay

The luminescence intensity from *N* atoms is given by:

$$I \propto -\frac{\mathrm{d}N}{\mathrm{d}t} = aN \tag{17}$$

The number of photons emitted (or the number of atoms de-excited) at time t is equal to the rate constant α times the number of excited atoms existing at time t.
Integration of this equation leads to [140]:

$$-\log I \propto -\log N = at \tag{18}$$

where the rate constant a is inversely proportional to the lifetime t of the excited state.

$$a = \frac{1}{\tau} = Se^{-E/kT} \tag{19}$$

where S is the frequency factor, τ is the time taken by the system to decay to $e^{-1}I_0$, (I_0 is the luminescence emission intensity at $t = 0$)

Hence:

$$I = I_0 e^{-at} \tag{20}$$

Hyperbolic decay

This type of decay takes place in a system where shallow irradiation traps are also produced along with deeper traps. The decay of phosphorescence occurs generally in two or three groups depending on the nature and concentration of the traps. In such cases, the observed intensity will be due to the superposition of all the exponentials corresponding to different traps and represented generally as [140]:

$$I = I_0 t^{-b} \tag{21}$$

where b is the decay constant.
Again:

$$I = I_0 t^{-b} = \sum_m I_{0m}\, e^{(-P_m t)} \tag{22}$$

where I_{0m} is the phosphorescence intensity due to electrons in traps of energy E_m and

$$P_m = Se^{(-E_m/kT)} \tag{23}$$

where P_m is the probability of an electron escaping from the trap.

Methods for the determination of optical properties

Absorption:

To characterize the optical properties of a material its absorption spectrum in the ultra violet to visible region can be measured [142]. It is useful to identify the active impurities and gives information on their environment. In crystalline host materials the polarization of absorption spectra can be used to conclude the site symmetries and crystal field parameters [140]. The ground state absorption investigates the excited state absorption characteristics. In addition, modified techniques are available, where two excitation sources are used: one powerful beam to excite the material and another to measure the absorption after the excitation pulse.

Excitation / emission:

In certain materials ground state absorption is too weak to be measured [137, 142]. A method known as "zero order excitation spectroscopy" can provide sufficient information. Emission at all wavelengths is directed to a detector without dispersion. By varying the wavelength of exciting beam and recording the strength of emission at all wavelengths a spectra equivalent to that of absorption of all luminescent centers can be recorded. In excitation spectra the emission wavelength that corresponds to the emission peak of the sample is fixed whereas the excitation monochromator is varied [144]. The much higher sensitivity of luminescence technique compared to absorption technique which can be an advantage for excitation spectra over absorption spectra [140]. Finally, excitation spectra can provide valuable information about excited state processes such as energy transfer that cannot be obtained by absorption spectra [145].

2.5 The Induction Skull Melting Technique

The Induction Skull melting technique was developed for the synthesis of high melting oxide single crystals materials, glasses and metallic alloys. The main focus lied on the growth of yttrium-stabilized zirconium dioxide (zirconia) single crystals which has been studied very good over the last decades [146 – 150]. However, other oxide materials, such as cerium oxide and Sapphire (Al_2O_3) have also been examined [152]. Skull melting is a combination of a high frequency induction heater and a (water-)cooled crucible in which the growth of the single crystals is achieved through directional cooling of the melt. The material is heated directly with a HF (high frequency) field, from the inside of the material, which means that at least in theory the temperatures which can be achieved are limitless and just dependent of the melting point of the material. The HF field is generated from a direct current in an oscillating circuit and induced though a water-cooled coil into the material. Therefore, no external heating source is needed. The cooled crucible prevents the outer parts of the material to melt during the inductive heating, hence, creating a thin ceramic boundary between the crucible wall and the melt. Therefore, the method can be described as a quasi-crucible-free. As a result, the grown crystals are very pure with little to no contamination of the crucible material. During the melt process the material densifies resulting in a hollow upper part of the created ceramic block. The ceramic block itself has a visual similarity with a skull, hence, the name Skull-melting. The cooled-crucible (which is usually made of copper) can be moved vertically in and out of the coil region, to achieve the directional cooling of the melt. As mentioned above, the parameter which influences the resulting temperatures of the melt is the melting point of the material itself creating together with the cooled crucible equilibrium between the inner melt and the outer ceramic boundary. Therefore, increasing the energy input will, just shift the equilibrium towards the melt, reducing the thickness of the ceramic boundary. The melt itself has approximately the temperature of the melting point and cannot be overheated.
The inductive heating and can be described through the Faraday equation [152]:

$$E = -k\mathrm{d}\psi/\mathrm{d}t \qquad (24)$$

where E ist he electromotive force (in Volt; V), $d\psi$ the variation of the electromagnetic flow and k a coefficient which in the International System of units (SI) is equal to 1.

The minus is indicating the direction of the electromagnetic flow. ψ is proportional to the number of induction coil windings ω *and* the magnetic flow Φ (in Weber; Wb):

$$\psi = \omega\Phi \tag{25}$$

Φ has a sinusoidal relation to time t and frequency f [7]:

$$\Phi_M = sin2\pi ft \tag{26}$$

This results in an electromotive force E [7]:

$$E = 4.44f\omega\Phi_{\mathrm{M}} \tag{27}$$

The thermal power P (in Watt; W) induced on the material can be described [152]:

$$P = EIcos\varphi = 4.44f\omega I\Phi_{\mathrm{M}}cos\varphi \tag{28}$$

where I is the current (in Ampere; A). Eq. 28 shows that the induced power is proportional to the frequency, meaning a higher frequency results in a higher induced thermal power. The power is also proportional to the number of induction coil windings and the amplitude of the electromagnetic flow. Most oxides with high melting points are insulators at room temperature. To heat up such materials through an electromagnetic field very high frequencies are needed. Due to practical and technical reasons the frequencies used do not exceed 10 MHz which is proved to be insufficient and prohibits the direct heating of the material. However, on higher temperatures there materials become electrically conducting. The addition of a secondary heat source is necessary to achieve a certain temperature of the material to become electrically conducting. For that purpose a small amount of metal (ignition material) is used to heat up a small region of the oxide material. Since the metal is conducting at room temperature, it can be heated up through the induced HF field, which subsequently will heat up the surrounding oxide material to the point where it will become electrically conducting itself and be induced by the HF field. Usually the metal of the corresponding oxide (e.g. Zirconium metal for Zirconium oxide) is used to avoid contamination. These metals can be called “ignition materials” (Zündmaterial). The induced material can then be melted step-by-step through the upward vertical movement of the crucible until everything is melted. The densified melt is occupying approximately the lower third of the crucible. The “ignition material” will oxidize and become part of the melt.

Alternatives for a secondary heat source may be graphite which will oxidize to CO_2 during the process, an oxyhydrogen torch or Laser to heat up a small region of the oxide material. In order to achieve an optimal crystal growth of high melting oxides with minimal energy loses certain thermal and electrodynamic processes have to be understood. Important are the interactions between the HF field and the solid/melt. However, the electrical and thermal properties at temperatures above 2000 °C are only described empirically, making a precise calculation of the process difficult. However, certain facts can be claimed: the melt becomes due to the inductive heating, the heat source, heating up the surrounding material which will become part of the melt and heating up even more material until the water-cooled part of the crucible is reached. The melt itself should always be at the height of the center of the coil. The process can only be stable if the generated power is equal to the heat loss.

The generated amount of heat Q is described as [152]:

$$Q = IRt \tag{29}$$

where I (in Ampere; A) is the current flowing running through the melt, R the electrical resistance (in Ohm; Ω) and t the time (in seconds).
The electrical conductivity σ can be described as [152]:

$$\sigma = \sigma_0 e^{\frac{-T_A}{T}} \tag{30}$$

where T_A and σ_0 are material specify parameters. The electrical conductivity is proportional to the temperature T. The electrical conductivity helps to describe the dependence of the penetration depth of the HF field from the circular frequency ω of the electric field [152]:

$$d = \left(\frac{2}{\omega\sigma\mu\mu_0}\right)^{1/2} \tag{31}$$

where μ_0 and μ are the electromagnetic permeability of the vacuum and the material, respectively. Equation 31 shows that the penetration depth decreases with the increase of frequency. The penetration depth is an important parameter and has to be considered during the development and construction of the crucible and the Skull melting machine. A higher penetration depth results in a smaller absorption of the HF field i.e. the field would go though the material without any energy transfer. The fact that the penetration depth and the conductivity are interconnected requires a certain skill with the usage of this technology.

The absorption of the field and the heat propagation in the melt can described schematically, as seen in figure 2.5.1.

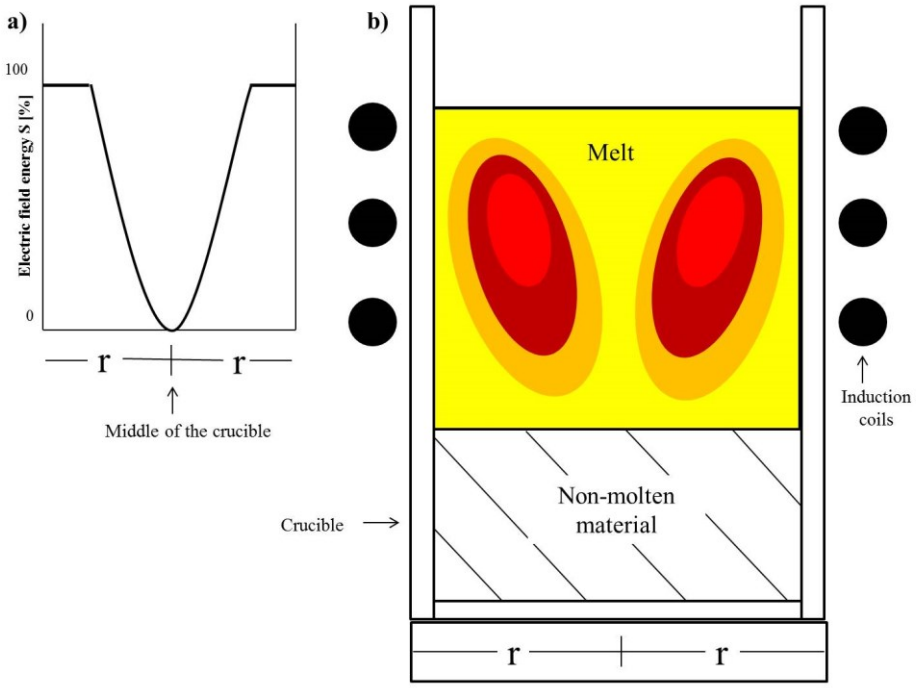

Figure 2.5.1. Schematic representation of the electric field energy *S* in a crucible with a certain thickness *2r* (a) and the heat propagation in the melt (b); where red indicates the hottest region. This heterogeneous heat distribution will homogenize over time due to convections effects in the melt [153].

The edges of the crucible which consist of the ceramic boundary, have little to no absorption of the electric field energy while the conducting melt absorbs all it. This leads to the hotter circular region in the middle of the melted material at the middle of the induction coil with decreasing temperature from middle to outer region. The heat distribution homogenizes over time in the melt due to convection effects. By driving the crucible out of the induction coil region the melt will cool down to a temperature for seed crystallization to take place. On these initial seeds will deposit more material over time which will result in the final crystals.

2.6 The Rietveld Analysis

The Rietveld analysis or Rietveld refinement is a mathematical tool for the analysis and evaluation of powder diffraction data [154 – 157]. Using a template with the same structure as the measured sample, which serves as a reference, a theoretical powder diffraction diagram is created and iteratively compared to the measured data. The comparison is based on the least square method. The Rietveld analysis consists of two segments, i) the profile and ii) structure fitting combined with the background adjustment. There are a number of mathematical functions used to determine the background. The most common is the 6-coefficient-polynomial function. Another possibility is the linear-interpolation which requires a manual positioning of each background point. Certain functions are also available for the reflection shape fitting, with the Pseudo-Voigt function being the commonly used. The Pseudo-Voigt function is a linear combination of a Gauß and Lorentz function, whereby the Gauß part is describing the sample specific influences on the form of the reflection and the Lorentz part the effects resulting from the measurement setup [156]. Simultaneously, the metric of the samples can be resolved as part of the structure fitting. Additional parameters can be determined during the analysis like atomic positions, thermal displacement or occupation. The Rietveld analysis makes it also possible to determine the composition of multi-phased material due to use of integral intensities. Important for the profile functions are the integral intensities of the the k reflection $I_{k,}$ the reflex postion $2\theta_k$ and the full width at half maximum (FWHM) HB_k. The Index of the measured point is I [156];

The intensity y_{ik} can be described with the Pseudo-Voigt function as such:

$$y_{ik} = wL_{ik} + (1 - w)G_{ik} \tag{32}$$

where L_{ik} describes the Lorentz function:

$$L_{ik} = y_{ik}(L) = \frac{I_k 2\sqrt{Ln2}}{HB_k\sqrt{\pi}\, e^{(-\delta_{ik}^2 ln2)}} \tag{33}$$

and G_{ik} the Gauß function [3]:

$$G_{ik} = y_{ik}(G) = \frac{2I_k}{HB_k\sqrt{\pi}\, e^{(1+\delta_{ik}^2)}} \tag{34}$$

Whereby:

$$\delta_{ik} = \frac{2(2\vartheta_i - 2\vartheta_k)}{HB_k} \tag{35}$$

A profile can also be described as a mere Loentz (w = 1) or Gauß function (w = 0).
The integral intensity I_k is described as:

$$I_k = \frac{I_{max,k} HB_k}{NF} \tag{36}$$

The normalizing factor *NF* is 0.637 for the Lorentz function and 0.939 for the Gauß function. $I_{max,k}$ is the maximum intensity at the position $2\vartheta_k$ [156].
The FWHM is described through the parameters *U, V* and *W* as such:

$$HB_k^2 = U \tan^2\vartheta_k + V \tan\vartheta_k + W \tag{37}$$

During the refinement, the parameters *U, V* and *W* are used to fit the profile. The refinement quality is expressed through the residual values R_w, R_{exp} and *S*.

$$R_w = \sqrt{\frac{\sum_i w_i (y_{oi} - y_{ci})^2}{\sum_i w_i y_{oi}^2}} \tag{38}$$

where y_o is the observed and y_c the calculated intensity, respectively. The value of w_i is presented as $1/y_{oi}$.

$$R_{\mathrm{exp}} = \sqrt{\frac{N-P}{\sum_i y_{oi}}} \tag{39}$$

R_{exp} is the expected value and used to determine the quality of the measurement, i.e. the lower the value the better the measurement. *N* describes the amount of measured point and *P* the number of varying parameters [156]. The goodness of fit *S* is described as:

$$S = \frac{R_{\mathrm{w}}}{R_{\mathrm{exp}}} \tag{40}$$

The minimum value for *S* can therefore be 1. In practice, a value of approximately 2 is considered as sufficient. For the structure fitting the structure factor F_{hkl} has to be defined:

$$F_{hkl} = \sum_j f_j \, e^{\left(-B_j \sin^2\frac{\vartheta}{\lambda^2}\right)} \, e^{(2\pi i(hx_j + ky_j + lz_j))} \tag{41}$$

The factor B_j is describing the spherical region in which an atom is moving due to thermic oscillation. The atomic form factor f_j describes the X-ray scattering of the atom and results from the radial electron density distribution as a quadratic wave function. The values for each atom are listed in the International Table for Crystallography Vol. C [157].

The value of λ described the wavelength of the emitting X-ray radiation (i.e. 1.54 Å for Cu K_{a1} or 0.54 Å for Mo K_a). The Miller-indices *hkl* are combined with the atom coordination *xyz*. The structure factor can be used to describe the intensity I_{hkl}:

$$I_{hkl} \sim |F|^2 \qquad (42)$$

Equation 42 shows that the intensity I_{hkl} is proportional to the squared absolute value of the structure factor. This equation is just an approximation; the complete equation involves additional parameters such as the Lorentz-polarization factor *LP*, the absorption factor *A*, and static disorder factor (or displacement factor) *T* etc. Nevertheless, equations 41 and 42 establish a relation between the atomic layers and the intensity. Modern software allows not only a numerical but also a graphical interpretation of the fitted data as shown in figure 2.6.1.

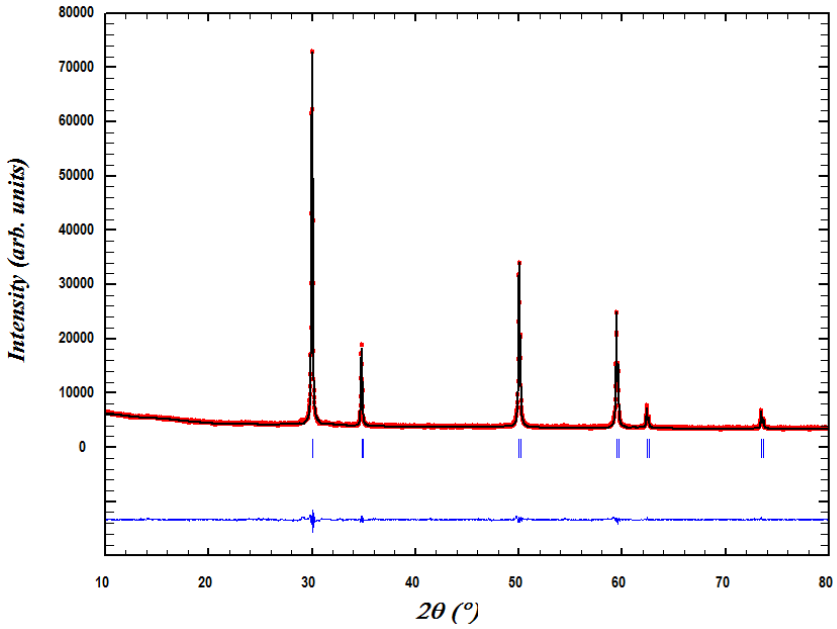

Figure 2.6.1. Graphical interpretation of a finalized Rietveld refinement (example of cubic YSZ). The red dots represent the measured data, while the black line represents the calculated powder diffraction pattern. The expected reflection positions are represented as small lines beneath the reflexes. The blue lines represent the difference between the calculated and measured diagram.

The red dots represent the measured data, while the black line represents the calculated powder diffraction pattern (with the fitted profile and structure). The expected reflection positions are represented as small lines beneath the reflexes (always two lines per reflex; for K_{a1} and K_{a2} radiation). The blue lines represent the difference between the calculated and measured diagram (i.e. the smoother the line the smaller the difference) [156].

2.7 Laue diffractometry

Laue diffractometry was first introduced 1912 and was the first X-ray diffraction experiment on a crystal. The theoretical background was established by Max von Laue, and the experimental setup by Friedrich and Knipping [158]. The lattice planes, as with all diffraction methods, has to satisfy the Bragg equation in order to diffract:

$$n\lambda = 2d_{hkl} \sin\vartheta \qquad (43)$$

where λ is the wavelength of the X-ray source, d_{hkl} the distance between the lattice planes and ϑ the reflection angle. n describes the order of diffraction and is always an integer. The difference to other X-ray diffraction methods lies in the source, which uses white non-monochromatic X-ray light. This results the satisfaction of the Bragg equation by multiple lattice planes at once, making the evaluation more difficult. Also a distinction between polar and non-polar rotation axes is not possible which makes the differentiation between structures with or without inversion center impossible. Therefore, a distinction between only 11 groups (instead of the 32 point groups) is possible [158]. These groups are also known as Laue-groups and are shown in table 2.7.1.

Table 2.7.1. The 11 Laue-groups and their corresponding crystal system.

Crystal system	**Laue group**
Triclinic	$\bar{1}$
Monoclinic	2/*m*
Orthorhombic	*mmm*
Tetragonal	4/*m* , 4/*mmm*
Trigonal	$\bar{3}$, $\bar{3}m$
Hexagonal	6/*m*, 6/*mmm*
Cubic	*m*3, $m\bar{3}m$

Since the light from the X-ray source is white no lattice plane distance d_{hkl} can be determined easily. The order of diffraction n has no influence on the difficulty evaluating the data since the intensity decreases rapidly with higher n.

Over the years the development of monochromatic X-ray light has been established to simplify the data collection and evaluation. However, the process is more time consuming in comparison to white light sources. Therefore, Laue diffractometry is still used for sensitive samples, like proteins, the observation of fast dynamic processes or simple and fast orientation and crystallinity definition [159].

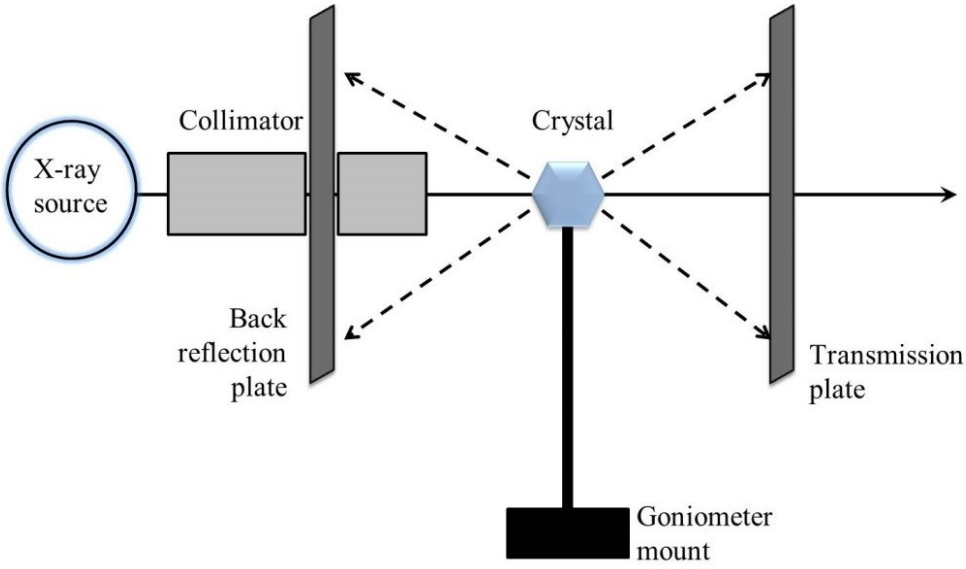

Figure 2.7.1. Schematic representation of the Laue diffractometry setup. The beam from the X-ray source is adjusted through the collimator to hits the crystal at the right position. The beam gets partially reflected and transmitted (diffracted) and reach the photosensitive plates. The pattern on these plates correspond certain structures.

Figure 2.7.1 shows a schematic linear setup of a Laue diffractometer. The X-ray source is usually a tube containing a Tungsten filament which creates under the used Voltage (~50 kV) no characteristic emission. The beam is then directed and focused through the collimator to the crystal. The diffracted beams reach photosensitive plates to record the pattern (one for transmission and reflection). Each lattice plane satisfying the Bragg equation creates a spot (reciprocal space) on the photosensitive plate creating a pattern corresponding to one of the 11 Laue groups [158].

3. METHODS

3.1 The Skull Melter

The machine, used for the growth of the single crystals in this thesis, is a prototype constructed from SurfaceNet GmbH (Rheine, Germany) in cooperation with Prof. Dr. W. Aßmus (Goethe Universität, Frankfurt a. M., Germany). The HF-generator is an IG 60/3000 from Trumpf-Hüttinger (Trumpf-Hüttinger Elektronik GmbH und Co. KG, Freiburg, Germany). The cooling circuit was constructed by the company Mercedöl (Mercedöl Feuerungsbau GmbH, Berlin, Germany). Figure 3.1.1 shows the induction skull melter and its components.

Figure 3.1.1. The Induction Skull Melter at the Institut für Chemie, Technische Universität Berlin; 1) Generator, 2) Primary and secondary resonator, 3) Control panel, 4) Crystal growth chamber, 5) Cooling circuit.

The machine consists of a water-cooling-circuit (primary and secondary), a high frequency generator, with primary and secondary resonator and a crystal growth chamber complete with a connected gas and vacuum supply which realizes crystal growth experiments under different gas atmospheres. The primary water circuit supplies a water amount of 18500 to 27000 L/h with a temperature of approximately 6 °C. The secondary water circuit re-circulates approximately 10500 L/h cooling water. The current intake of the generator is 126 kA. The power output of the primary resonator circuit is 72 kW. The secondary resonator circuit works with a frequency of 1.61 MHz. The used crucible consists of copper, since copper has a good thermal conductivity and mechanical stability and is also water cooled (Figure 3.1.2).

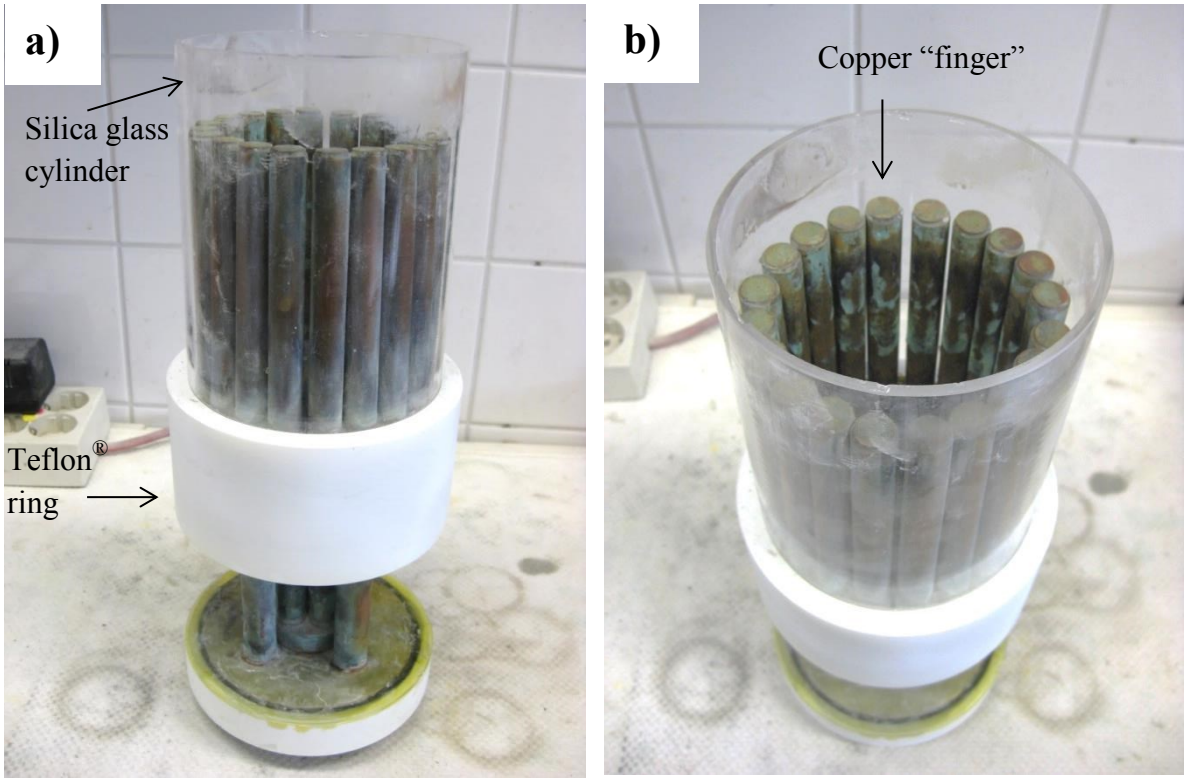

Figure 3.1.2. The Skull Melter crucible as seen from the side (a) and above (b). The crucible is build of several copper “fingers” and enclosed by a silica glass cylinder. A ring of perfluorcarbon (Teflon®) is fixating the contraption.

The crucible is 60 mm in inner diameter and 120 mm in height, resulting in a volume of 0.6 l. The bottom of the crucible is split and the wall is not closed but build of numerous “fingers”. This setup is necessary to avoid the buildup of any ring current which would result in loss of electrical power. The two halves at the bottom are separated through mica plates to avoid any electrical contact/overload.

The bottom is also surrounded by ring of perfluorcarbon (Teflon®) to avoid the contact between crucible and coil, which would result in an electrical overload at the capacitor of the secondary resonator circuit. On the Teflon® ring sits a silica glass tube which surrounds the copper fingers to avoid contact to the coil and to hold up any melt eventual pouring out of the crucible during the Skull melting process (Figure 3.1.2). Hereby, silica glass has a low thermal expansion coefficient which will prevent any breaking through thermal stress. The whole crucible is screwed on a "lance" which can be vertically moved. The lance provides the crucible with the cooling water from the secondary water circuit. The induction coil is made of copper and also water-cooled. It sticks in the crystal growth camber, encircling the crucible. The coil consists of 3 windings and has a height of 60 mm and inner diameter of 120 mm. The actual crystal growth process will be described in the following chapter.

3.2 Single Crystal Growth

Every single crystal growth starts with the powder of the respective oxide materials. If needed, the starting materials can be mixed and homogenized in a powder mixer (prototype; Technische Universität Berlin, Berlin, Germany). Approximately 2 kg of material are required for a growth experiment. Some materials (like TiO_2) need to be sintered to densify the powder in order to get more material into the crucible. The system requires a minimum mass of the material in order to keep the induction process stable. The powder is stuffed and compressed manually in the crucible. 5 g to 8 g of the "ignition metal" are embedded to approx. 1 to 3 cm under the powder surface (the exact height and amount for each grown crystal will be mentioned in Chapter 4). The crucible (screwed on the lance) is moved vertically until the ignition metals are located at the middle of the induction coil. The growth chamber is closed and purged with certain gases if needed. The used gas atmospheres for each grown crystal will be mentioned in Chapter 4. The experiment starts heating up the powder slowly, for approximately 15 min, with low power output. The power is controlled manually, while the voltage is adjusting automatically according to the current flowing through the material. The power regulation takes place through the adjustment of the amplitude of the electromagnetic flow Φ_m. The power output is increased step-by-step until the inductive coupling is achieved. Inductive coupling is the process in which the material is heated up enough through the ignition metal to become sufficient electrical conducting, resulting in the absorption of the HF field and the gradually melting of the material. The powder at the edges of the crucible remain solid (sinter-crust) by the water-cooling. The surface of the material may also stay solid due to the heat emission. The crucible is moved gradually while increasing steadily the power output until the material is completely melted (with exception of the edges). The system is held in the idle position for approximately 30 min in order for the convection to homogenize the melt. During this time the system stays under constant observation by the user for any inductive appearing decoupling or melt spillage.

Inductive decoupling is the process in which the power of absorbed HF field is not enough to keep the material melted i.e. the equilibrium of melt and the cooled solid edge is shifted towards the solid condition and the material solidifies prematurely.

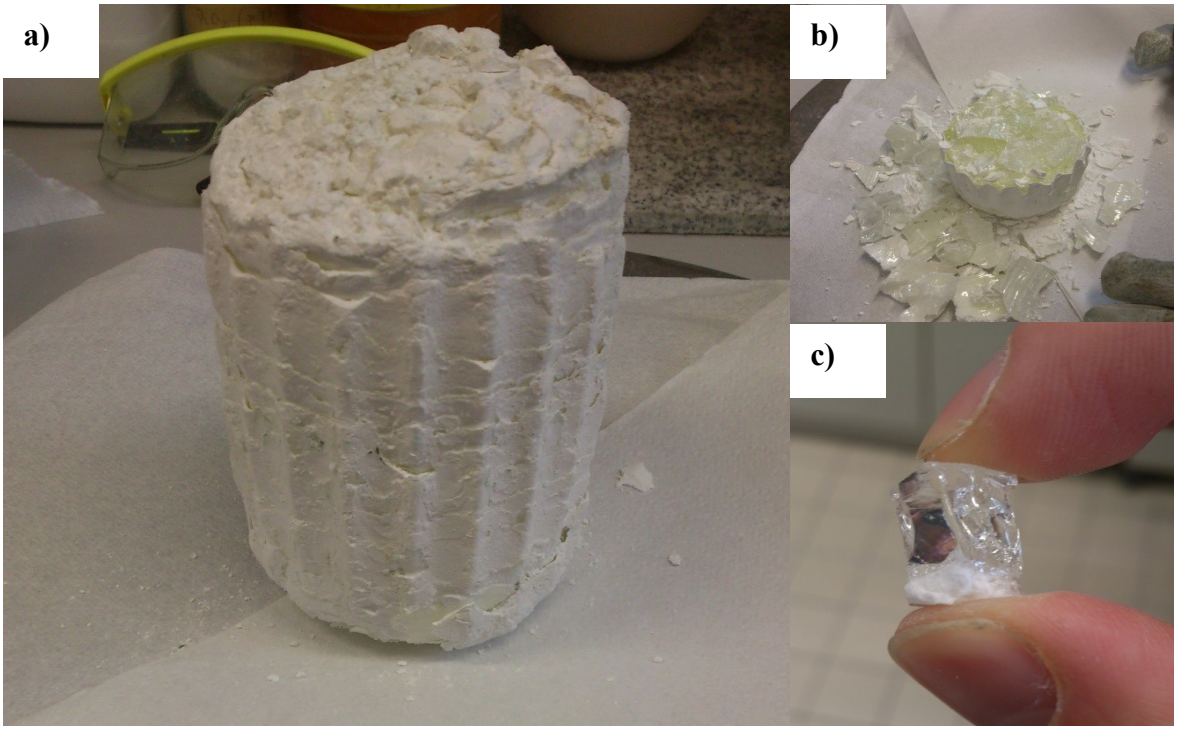

Figure 3.2.1. a) The Skull after the growth experiment. The solid edges have taken a negative imprint of the crucible fingers. b) a broken Skull and the lower c) a separated crystal (cubic YSZ).

In this case the power output has to be increased. A melt spillage occurs when the equilibrium between melt and cooled solid edge is shifted towards the melt, decreasing the thickness of the solid edges. This results in the breaking of the solid edges at certain breaking points and the spill of the melt. To avoid this scenario, the power output has to be decreased in advanced. Howver, the experiment has to be stopped immediately if spillage of the melt occurs. Afterwards, the crucible is moved vertically out of the induction coil region. The movement speed varies severely (1 mm/h to 15 mm/h) for each material and will be shown in more detail in Chapter 4. After a few hours the growth experiment is finished, the power is steadily decreased and finally turned off. The result is shown in Figure 3.2.1.

3.3 X-ray Structure Analysis

The structure analysis was accomplished through 3 experiments; one powder and two single crystal diffraction experiments (Laue and 4-circle diffractometer).

3.3.1 Powder Diffraction

The X-ray powder diffraction experiments were conducted with the X`Pert Pro from PANalytical (PANalytical B.V, Almelo, Netherlands). It consists of a ϑ/ϑ setup and Bragg-Brentano geometry. The X-ray sources consist of copper. The Bremsstrahlung and the radiation below the K_α wavelength are filtered through a Ni-filter. The setup uses no monochromatic light, which results in the presence of $CuK_{\alpha1}$ and $CuK_{\alpha2}$ radiation (with a ratio of 2 to 1). An automatic divergence aperture is used to keep the irradiated sample area constant with varying angles. This must be taken to account for the following Rietveld analysis. As a detector, a Si(Li)-semiconducting detector was used. The supplied software X`Pert Highscore Plus *v.2.2.1* was used for a first quick evaluation of the measurement through the Inorganic Structure Database (ICSD, FIZ Karlsruhe, Germany and US Department of Commerce, USA).

3.3.2 Laue Diffraction

The setup is a prototype constructed from STOE (STOE & Cie GmbH, Darmstadt, Germany). The X-ray source consists of white light (non-monochromatic light) emitted from a tungsten tube. The detection of transmission and refection is possible by photosensitive plates. The plates are therefore coated with Eu:BaBrF. The emitted X-ray radiation oxidized the Europium from Eu^{2+} to Eu^{3+}, creating a long-lasting free electron (color center), which can be used for the analysis. For data evaluation the software OrientExpress (by Jean Laugier and Bernard Bochu at Laboratoire des Materiaux et du Génie Physique de l'Ecole Supérieure de Physique de Grenoble) was used. The software allows the use of simulated Laue structure patterns to overlay on the obtained Laue image to confirm the crystal structure and estimate the orientation of the crystals

3.3.3 Single Crystal Diffraction

The single crystal diffraction experiments were conducted with the X`calibur E X-ray diffraction system from Agilent (Agilent Technologies, Santa Clara, CA, USA). The setup uses a single wavelength molybdenum (Mo Kα; λ = 0.54 Å; 3 kW) fine focus X-ray source and a 4-circle kappa goniometer. As sensor, was the Eos CCD detector used with a diameter of 64 x 64 mm. The measurements were all performed at approximately 150 K (N_2-cooling system). The sample preparation and execution of the X-ray single crystal diffraction experiment were conducted by Ms. Paula Nixdorf. The structure refinement was carried out by Dr. Dennis Wiedemann using the CrysAlisPro software (CrysAlisPro v.1.171.37.35, Agilent Technologies).

3.4 Optical Spectroscopy

Certain optical spectroscopy experiments (i.e. UV/Vis. and luminescence spectroscopy) were conducted by several workgroups:

- Single crystal UV/Vis. spectroscopy measurements at room temperature were conducted by Dr. Klaus Irmscher at the IKZ (Leibniz Institut für Kristalzüchungt, Berlin). The setup was a Lambda 19 from Perkin Elmer (Perkin Elemer, Waltham, MA, USA) detecting transmission at a wavelength rage of 200 nm to 2500 nm, using polarized emission in an integrating sphere (Ulbricht sphere). The circular aperture has a diameter of 5 mm.
- Single crystal UV/Vis. spectroscopy measurements at high temperature were conducted by Mr. Martin Naumann at the IKZ in Berlin. The setup was a prototype using a HT19 oven from Hesse (Hesse Instruments, Osterode am Harz, Germany), an EQ-99 model from ENERGETIQ (ENERGETIQ Technology Inc., Woburn, MA, U.S.A.) as light source and a spectrograph from Stresing (Entwicklungsbüro Stresing, Berlin, Germany). The measurements were conducted in air with temperature steps of 50 K (from 25 °C up to 1000 °C).

- Absorption/reflection spectroscopy measurements were conducted by Mr. Sascha Krüger at the University Siegen (AK Wickleder, Universität Siegen, Siegen, Germany). The setup consists of an Fluorolog®-3 Spectrofluometer FL3-22 from Jobin Yvon (HORIBA Jobin Yvon Scientific, Edison, NJ, U.S.A.) and a Xenon light source with monochromator (spectrum for UV to IR).
- Diffuse reflectance (DR) spectroscopy measurements were conducted by Dipl. Chemiker Sven Kühn at the Technische Universität Berlin (AK Ressler, Technische Universität Berlin, Berlin). The spectra were measured in a wavelength range of 890 nm to 220 nm. The experimental optical band-gap has been determined by the use of the Kubelka-Munk function obtained from the DR spectrum.

3.5 ICP-OES

The inductively coupled plasma optical emission spectroscopy measurements were by Dr. Rainer Bertram from the Institute of Crystal Growth (IKZ) in Berlin. The single crystals were grinded to a fine powder with the vibrating mill MM-2 from Retsch (Retsch GmbH, Haan, Germany) The samples were pre-heated via microwaves with an ETHOS plus from MLS (MLS GmbH, Leutkirch, Germany) prior to the measurements. The used ICP spectrometer is an IRIS Interpid HR Duo from Thermo Elemental (Thermo Fisher Scientific Inc., MA, USA). Three separated weigh portions of each sample were used for the measurements.

4. RESULTS AND DISCUSSION

4.1 $(Ca,Sr,Ba)ZrO_3$

Three single crystal perovskites were successfully grown for the first time and examined as part of this thesis; $CaZrO_3$, $SrZrO_3$ and $BaZrO_3$.

4.1.1 Single crystal growth

It was necessary to prepare the perovskite material prior to the growth experiment. ZrO_2 (99.99%) was mixed with $CaCO_3$ (99%), $SrCO_3$ (99%) or $BaCO_3$ (99%), (for $CaZrO_3$, $SrZrO_3$ and $BaZrO_3$) homogenously in a molar ratio of a 1:1 and fired in an alumina crucible at a temperature of 1500 °C for 12 h. The exact mixture and solid state reaction parameters are listed in Table 4.1.1. The resulting zirconate powders were then filled in the Skull-crucible for the growth experiment. The growth experiment was conducted under normal air atmosphere conditions, with the exception of $SrZrO_3$ where a nitrogen atmosphere was used. Zirconium was serving as ignition metal with amounts in the range of 6.1 g to 7.8 g. It should be noted that the absorption of the HF field from the melted material was very high, resulting in a high power output relative to the other experiments (Table 4.1.2). The solid surface of the material tended to break during the melt process, hereby revealing the melt. This resulted in a large heat emission, disrupting the solid-melt equilibrium. Therefore, the ignition metal has been placed deeper in the material, at a depth of approximately 3 cm. This results in a thicker upper crust of the material, therefore, minimizing the risk of breaking. The grown $CaZrO_3$ single crystals will be referred to as V78. Two growth experiments of $SrZrO_3$ were conducted; under air (V79) and nitrogen (V82) atmosphere, respectively. The first growth experiment (V79) showed sublimation effects of the material during the growth. Parts of the material started to evaporate during the melt process which was obscuring the vision to the experiment and deposed on the inner wall of the growth chamber. This also ran the risk of disrupting the stoichiometry of the pre-synthesized material. In order to avoid the sublimation on the second experiment (V82) a 1.35 bar nitrogen atmosphere was established. $BaZrO_3$ will be referred to as V92.

Table 4.1.1. Stoichiometry and solid state parameters of the starting perovskite materials which were prepared prior to the single crystal growth experiment.

$CaZrO_3$ (V78)		**$SrZrO_3$ (V79 and V82)**		**$BaZrO_3$ (V92)**	
Compound	**mass [g]**	**Compound**	**mass [g]**	**Compound**	**mass [g]**
ZrO_2	1109.1	ZrO_2	1232.2	ZrO_2	1232.2
$CaCO_3$	900.8	$SrCO_3$	1475.9	$BaCO_3$	1973.3
Sum	2009.9	**Sum**	2708.1	**Sum**	3204.6
Solid state reaction parameters					
Temperature [°C]		1500			
Time [h]		12			

As mentioned above, the growth experiments were conducted mostly under normal air atmosphere conditions with the exception of $SrZrO_3$ (V82) where a nitrogen atmosphere was used. Zirconium metal was serving as ignition metal. The absorption of the HF field from the melted material was very high resulting in a high power output relative to the other experiments as shown in Table 4.1.2.

Table 4.1.2. Operating parameters of the grown zirconate crystals

	$CaZrO_3$ (V78)	**$SrZrO_3$ (V79)**	**$SrZrO_3$ (V82)**	**$BaZrO_3$ (V92)**
Ignition metal	Zr; 6.5 g	Zr; 6.1 g	Zr; 7.5 g	Zr; 7.8 g
Growth atmosphere	Air; 1 bar	Air; 1 bar	N_2; 1.35 bar	Air; 1 bar
Parameters at idle position				
Voltage [%]	73	80	90	80
Current [%]	32	39.5	38	34
Power output [%]	23	31.5	36	28

The crucible was kept at the idle position for approximately 30 min to achieve a good homogenization of the melt prior to the growth. The idle position is the position at which the crucible was driven gradually up until the end where all the material is melted.

Table 4.1.3. Growth parameters (speed and time) for the grown zirconate crystals.

	$CaZrO_3$ (V78)	**$SrZrO_3$ (V79)**	**$SrZrO_3$ (V82)**	**$BaZrO_3$ (V92)**
Speed	**Time**	**Time**	**Time**	**Time**
Idle phase	30 min	30 min	30 min	30 min
1 mm/h	1 h 30 min	30 min	1h 30 min	1h 30 min
3 mm/h	1 h	3 h	1 h	1 h
6 mm/h	1 h	30 min	1 h	1 h
9 mm/h	1 h	1 h	1 h	1 h
12 mm/h	1 h	30 min	30 min	1 hours
15 mm/h	1 h	30 min	/	/
18 mm/h	/	/	/	/
Sum	**7 h**	**6 h 30 min**	**5 h 30 min**	**6 hours**

The growth experiment took approximately 7 hours for $CaZrO_3$ (V78), 6.5 hours for $SrZrO_3$(air) (V79), 5.5 hours for $SrZrO_3(N_2)$ (V82) and 6 hours for $BaZrO_3$ (V92) to complete. Hereby, starting with a growth speed of 1 mm/h and gradually increasing pulling up speed up to 15mm/h (Table 4.1.3). Figure 4.1.1 shows the as-grown zirconate single crystals for each experiment.

$CaZrO_3$ (V78)

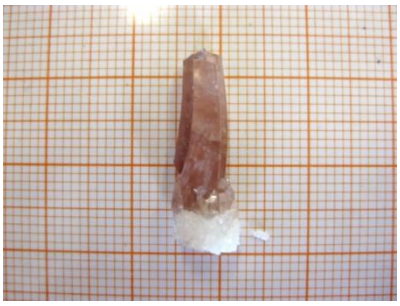

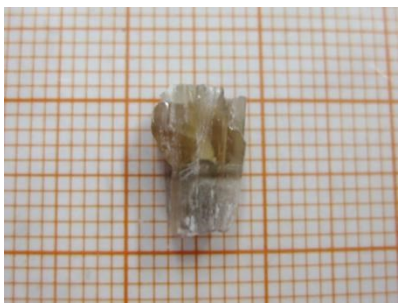

$SrZrO_3$ (V79); Air

cont.

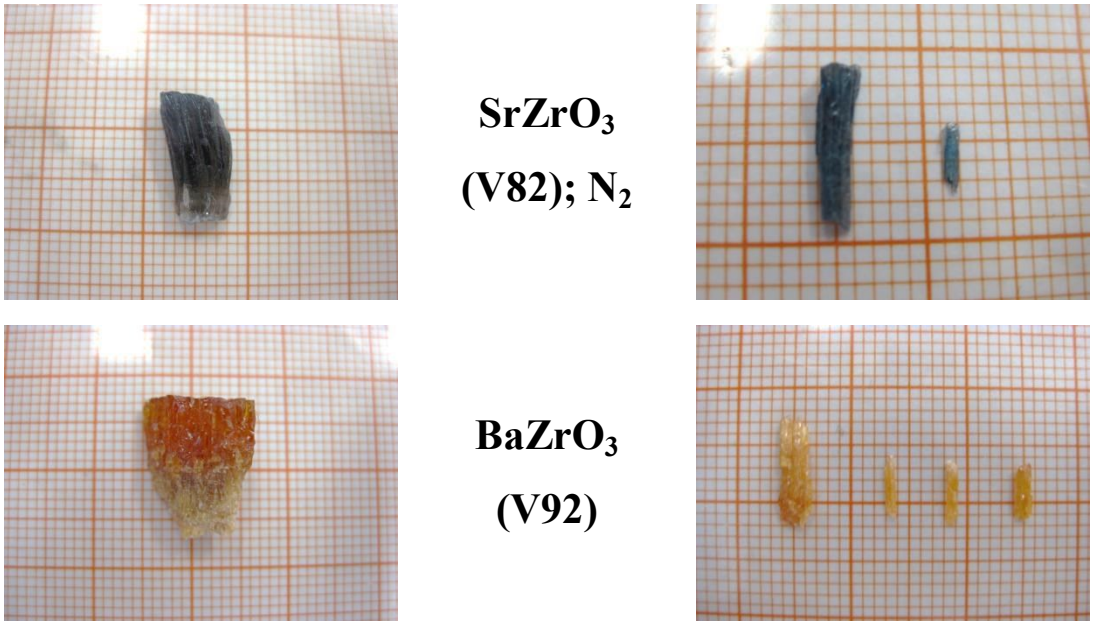

Figure 4.1.1. As-grown zirconate single crystals of $CaZrO_3$ (V78), $SrZrO_3$ (V79 and V82) and $BaZrO_3$ (V92); shown as "bundle" on the left and as separated crystals on the right. The white colored region on the certain crystals consist of the lower part of the Skull crust.

$CaZrO_3$ (V78) has an elongated shape with a length of approximately 2 cm and width of 0.5 cm (2 x 0.5 x 0.5 cm^3) respectively. The color can be described as "dusky" pink. The crystals are not completely transparent which already indicates defect and/or twinning effects. $SrZrO_3$ (V79) has a length of approximately 0.5 cm and a width of 0.1 cm (0.5 x 0.1 x 0.1 cm^3) and a light brown color. V82 features similar dimensions and shape compared to V79 (0.7 x 0.1 x 0.1 cm^3) but has a dark blue color. The different colorizations will be addressed in Chapter 4.1.3. Both crystals (V79 and V82) are opaque, indicating defect and/or twinning effects as well. $BaZrO_3$ (V92) is sharing the dimensions and shape of V79 and V82 (0.6 x 0.2 0.2 cm^3) and features an orange color. The smaller crystals are transparent in contrast to the other grown zirconate crystals.

4.1.2 Structural analysis

The first structural characterization was achieved via X-ray powder diffraction analysis. A single crystal of each grown material was grinded to a powder and measured.

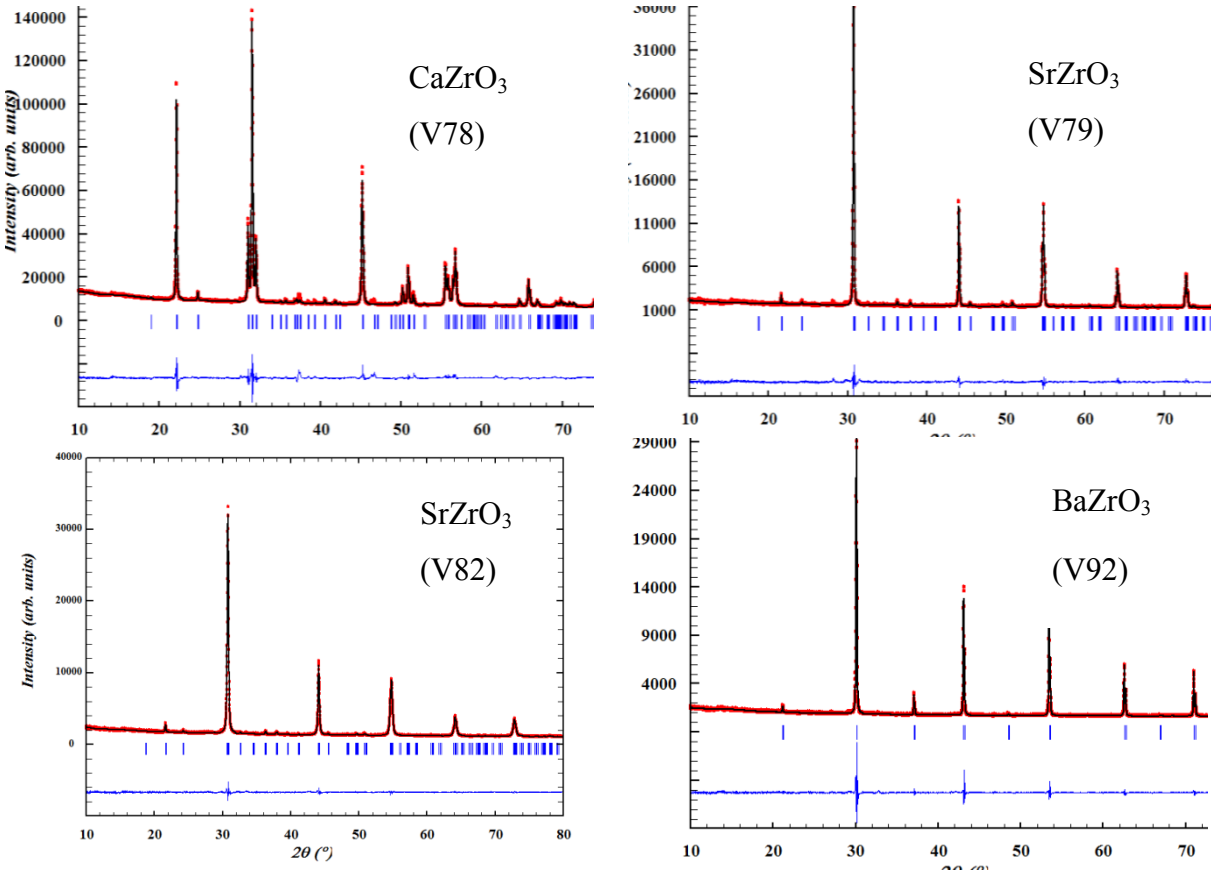

Figure 4.1.2. X-ray powder diffraction diagrams of the grown zirconates crystals (V78 upper left; V79 upper right; V82 lower left; V92 lower right) with the graphical interpretation of the Rietveld refinement.

Figure 4.1.2 shows the X-ray powder diffraction patterns of the grown zirconate crystals with the completed Rietveld fit. The V78 sample has an orthorhombic structure and was refined in space group *Pcmn* (general: *Pnma* No. 62) with four formula units per cell. The lattice parameters are a = 5.5902 Å, b = 8.0170 Å and c = 5.7665 Å. V79 and V82 have an orthorhombic structure as well and were refined to the space group *Pbnm* (general: *Pnma*; No. 62) with four formula units per cell. The lattice parameters are a = 5.7911 Å, b = 5.8241 Å and c = 8.2045 Å for $SrZrO_3$ (V79) and a = 5.7964 Å, b = 5.8227 Å and c = 8.2088 Å for $SrZrO_3$ (V82). Both have four units per cell as well. It should be mentioned that the diffraction pattern of V79 is showing one very small additional reflection at the 2θ position of 28°. However, it was not possible to accurately determine its origin.

Some possible explanations were a slight contamination of the material during the grinding or the sublimation effect during the growth process of the V79 single crystal caused a small disruption in the stoichiometry of the material .Nevertheless, this additional reflection was so small that it did not influence the refinement. $BaZrO_3$ (V92) has a cubic structure and was refined in space group $Pm\bar{3}m$ (No. 221) with one formula unit per cell. The lattice parameters is a = 4.1951 Å. Table 4.1.4 lists the lattice parameter and goodness of the fit values.

Table 4.1.4. Results of the Rietveld refinement of the zirconate samples (standard deviations in parentheses where applicable).

	$CaZrO_3$ (V78)	**$SrZrO_3$ (V79)**	**$SrZrO_3$ (V82)**	**$BaZrO_3$ (V92)**
Space group	*Pcmn (Pnma)*	*Pbnm (Pnma)*	*Pbnm (Pnma)*	$Pm\bar{3}m$
Lattice parameter [Å]	a = 5.76165 (17) b = 8.01706 (17) c = 5.59022 (12)	a = 5.7911 (3) b = 5.8241 (3) c = 8.20458 (4)	a = 5.79648 (1) b = 5.82275 (13) c = 8.2089 (2)	a = 4.1951 (8)
R_{wp}	3.02	2.25	3.06	5.19
R_{exp}	1.92	2.45	2.39	2.65
R_{Bragg}	5.75	2.34	5.10	2.90
S	1.57	1.08	1.28	1.95

The better value of S for V79 compared to V82 was not expected given the slightly less pure nature of V79. Nevertheless, the overall refinement values of all samples are acceptable indicating a good fit. Laue-diffraction experiments have been conducted to determine the single crystal nature of the material.

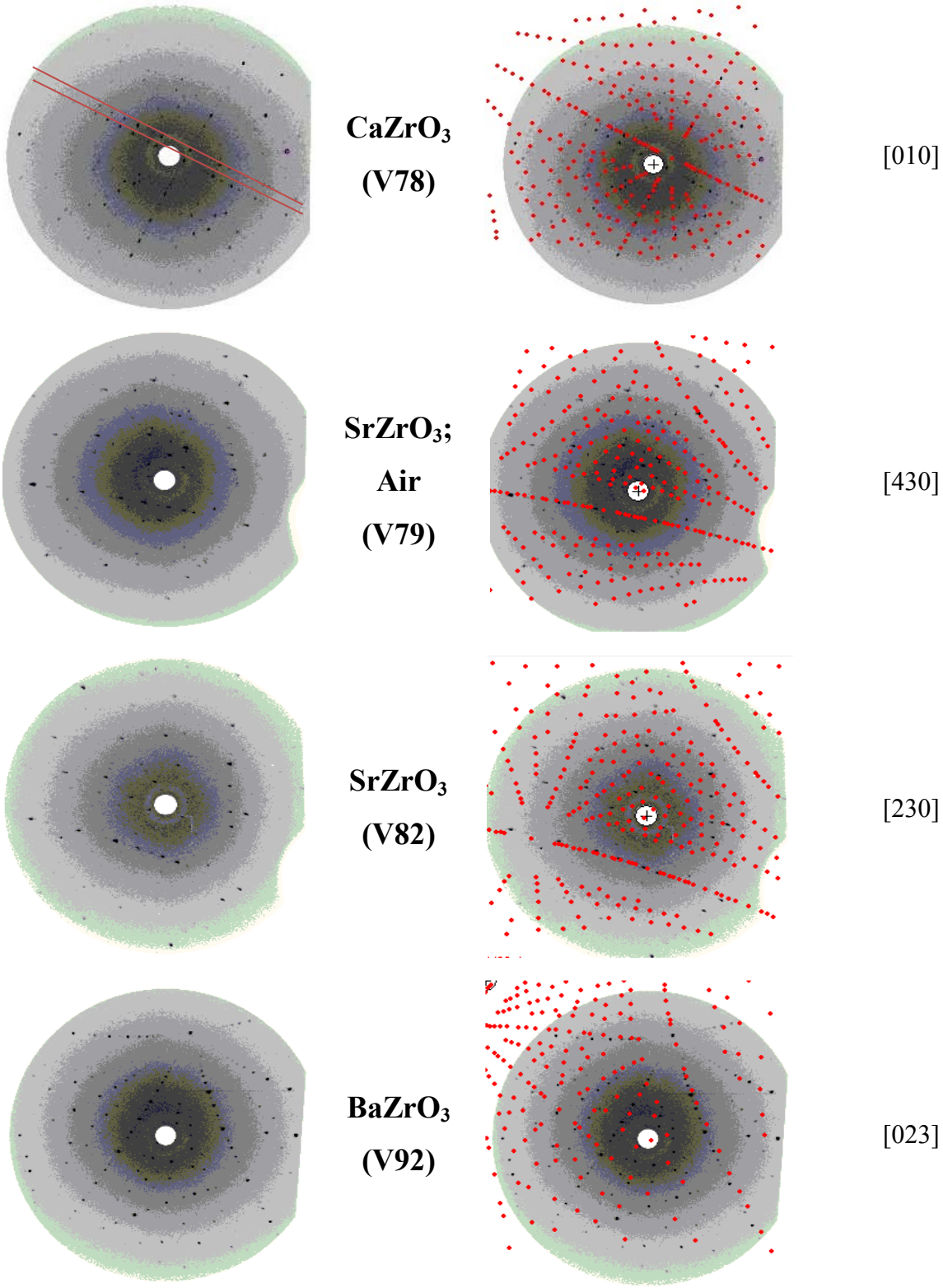

Figure 4.1.3. Laue diffraction patterns (reflection) of the grown zirconate single crystals; as measured (left) and with overlaid simulated structure pattern (right) with their corresponding orientation. A possible twin is seen in the pattern of V78 as two parallel lines (marked by red lines).

Figure 4.1.3 shows the Laue diffraction patterns (reflection) of the zirconate single crystals. All patterns show diffraction points which indicate a single crystal nature of the materials since no diffraction rings can be observed. By using the software Orient express simulated structure patterns have been generated and laid over the Laue images. The structure patterns were then adjusted by varying the *x, y* and *z* coordinates to fit the structure pattern of the Laue image. The shown simulated structure patterns fit the best on the Laue images. $CaZrO_3$ V78 is oriented towards the [010] direction and features a second parallel line along the [001] direction indicating possible twinning in the structure. The other particular Laue images indicate no twins. The Laue images of $SrZrO_3$ (V79 and V82) seem to be oriented towards the [430] and [230] direction axis, respectively. The corresponding Laue group of *Pcmn*/*Pbnm* is *mmm*. The Laue image of $BaZrO_3$ V92 appear to be oriented approximately towards the [023] direction axis, with the Laue group for the cubic $Pm\bar{3}m$ being $m\bar{3}m$.

In addition to the Laue diffraction, single crystal diffraction experiments have been conducted to describe the single crystal nature of the materials. It should be noted that the single crystal analysis was only conducted for $SrZrO_3(N_2)$ V82 since the structural differences of $SrZrO_3$ (Air) V79 and $SrZrO_3(N_2)$ V82 were marginal. The absorption coefficients of the three crystals were very high resulting in a low total number of reflections. The refinement of the single crystal data confirms an orthorhombic structure for V78 (*Pcmn*) and V82 (*Pbnm*) with lattice parameter of a = 5.7505, b = 7.9953 Å and c = 5.5779 Å for V78 and a = 5.7881 Å, b = 5.8109 Å and c = 8.1933 Å for V82. These values correlate very well with the powder diffraction data. The structure and lattice parameters of V92 ($Pm\bar{3}m$) correlate also very well with the powder diffraction data. The complete data of the single crystal refinement is listed in Table 4.1.5.

Table 4.1.5. Results of the single crystal data refinement of the grown zirconate single crystals (standard deviations in parentheses where applicable).

Sample	V78 $CaZrO_3$	V82 $SrZrO_3$	V92 $BaZrO_3$
Molar mass (g mol^{-1})	179.30	226.84	276.56
Crystal system	Orthorhombic	Orthorhombic	Cubic
Space Group	*Pcmn* (62)	*Pbnm* (62)	$Pm\bar{3}m$ (221)
Radiation	MoK_a (λ = 0.71 Å)	MoK_a (λ = 0.71 Å)	MoK_a (λ = 0.71 Å)
Temperature (K)	150.2 (2)	150 (2)	151 (2)
a (Å)	5.7505 (3)	5.7881 (5)	4.1905 (2)
b (Å)	7.9953 (5)	5.8109 (3)	4.1905 (2)
c (Å)	5.5779 (3)	8.1933 (6)	4.1905 (2)
V ($Å^3$)	256.45 (3)	275.57 (3)	73.59 (10)
Formula units per cell (z)	4	4	1
Calculated density (g cm^{-3})	4.64	5.47	6.24
F(000) (e)	336	408	120
Crystal size (mm^3)	0.69 x 0.51 x 0.39	0.36 x 0.12 x 0.10	0.53 x 0.25 x 0.13
Absorption coefficient (mm^{-1})	6.017	22.887	16.603
Absorption correction	analytical	analytical	analytical
ϑ range (°)	3.59 - 32.55	4.31 - 29.98	4.87 - 30.58
Range in hkl	$7 \leq h \leq 6$	$8 \leq h \leq 8$	$6 \leq h \leq 5$
	$9 \leq k \leq 9$	$8 \leq k \leq 8$	$5 \leq k \leq 5$
	$6 \leq l \leq 6$	$11 \leq l \leq 11$	$6 \leq l \leq 6$
Total no. of reflections	738	431	41
Independent reflections	738	431	41
Reflections with $I > 2\ \sigma(I)/R\sigma$	738	431	41
Ref. parameters	0.1467	0.0604	0.0221
Goodness of fit on Fi^2	1.562	1.052	1.297
Final indices R_1/wR_2 [$I > 2\sigma(I)$]	0.0376	0.0403	0.0089
Final indices R_1/wR_2 (all data)	0.0376	0.0403	0.0089
Largest diff. peak and hole (e $Å^{-3}$)	1.574 / -1.929	1.708/-1.366	0.287 / -0.517

The orthorhombic structure of V78 and V82 (and V79 as well) is a result of the tilted $[ZrO_6]^{2-}$ octahedra (Figure 4.1.4). This is also shown by the Goldschmidt tolerance factor of $\tau = 0.89$ and $\tau = 0.95$ for V78 and V82 (V79), respectively. According to the classification proposed by Glazer, V78 and V82 belong to the $a^- b^+ a^-$ category of tilting with an out of plane tilting about the [001] and [100] axes and an in-plane tilting about the [010] axis. The [010] axis is also referred to as pseudo-cubic axis.

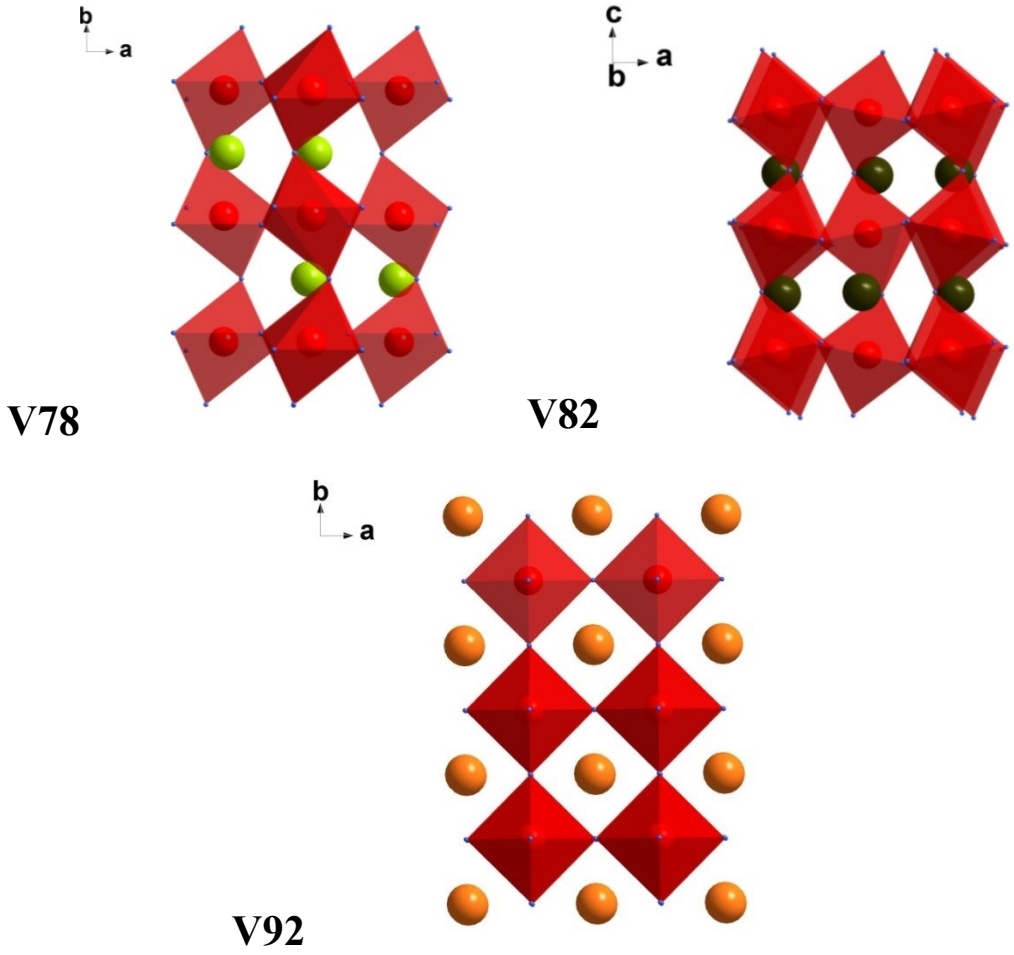

Figure 4.1.4. Crystal structures of $CaZrO_3$ (V78), $SrZrO_3$ (V82), and $BaZrO_3$ (V92) showing the different tilting of the $[ZrO_6]^{-2}$ corner-sharing octahedra. The space in between is occupied by the corresponding Ca^{2+}, Sr^{2+} and Ba^{2+} cations.

The $[ZrO_6]^{-2}$ octahedra of the cubic V92 feature no tilting at all and belong therefore according to the classification proposed by Glazer, in the $a^0 a^0 a^0$ category of tilting with no in-plane or out-of-plane tilting. This is also demonstrated by the Goldschmidt tolerance factor of 1.01.

The following tables summarize the atomic coordinates, Wyckoff positions, and anisotropic displacement factors as well as selected values for the bond lengths and interatomic angles of the grown zirconate single crystals which resulted from the refinement of the single crystal data.

Table 4.1.6. Wyckoff positions and atomic coordinates for the grown zirconates (standard deviation in parentheses).

Atom	**Wyck.**	***x***	***y***	***z***
$CaZrO_3$ (V78)				
Ca1	4*c*	0.0504 (7)	1/4	0.4875 (3)
Zr1	4*a*	0	0	0
O1	4*c*	0.4601 (11)	1/4	0.6050 (11)
O2	8*d*	0.2996 (7)	0.0555 (5)	0.1976 (7)
$SrZrO_3$ (V82)				
Sr1	4*c*	0	0	0
Zr1	4*a*	0.00553 (15)	0.52053 (14)	1/4
O1	4*c*	-0.0692 (11)	-0.0126 (14)	1/4
O2	8*d*	0.2185 (10)	0.2809 (10)	0.0347 (6)
$BaZrO_3$ (V92)				
Ba1	1*b*	1/2	1/2	1/2
Zr1	1*a*	0	0	0
O1	3*d*	1/2	0	0

The anisotropic displacement factors are tensors. These tensors Uij are the squares of the displacements of the electron density function from the coordinates in the structure. The diagonal U_{11}, U_{22}, and U_{33} consider the displacements along the cell edges and the other elements the displacements at the angle to the cell edges. The displacements are caused from the thermal motion and static disorder of atoms. Figure 4.1.5 shows this in the thermal ellipsoid plot ($BaZrO_3$ as an example). The parameters shown in Table 4.1.7 indicate a greater displacement along the cell edges. Especially the displacements of the two cations in the orthorhombic structures show a high displacement due to their distortion. The displacement of V92 is equal for the diagonal $U_{11,}$ U_{22} and U_{33} elements and zero for the other elements as expected from a cubic structure.

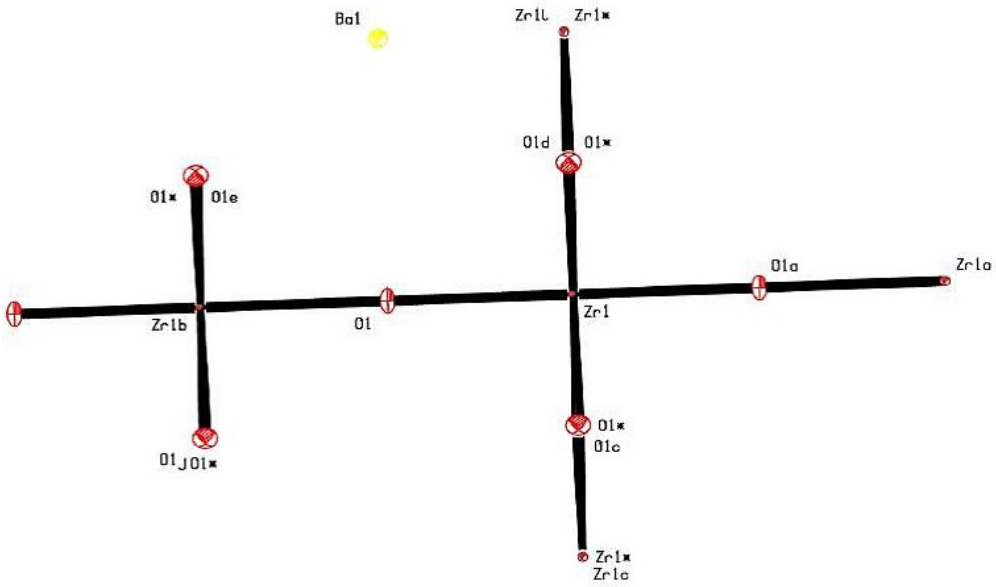

Figure 4.1.5. Thermal ellipsoid plot (50% probability) of $BaZrO_3$ (V92). The O1 positions can be seen as ellipsoids

Table 4.1.7. Anisotropic displacement parameters for the grown zirconates (standard deviation in parentheses).

Atom	U_{11}	U_{22}	U_{33}	U_{12}	U_{13}	U_{23}
$CaZrO_3$ (V78)						
Ca1	0.0044 (14)	0.0072 (14)	0.0055 (13)	0,0000	-0.0004(6)	0,0000
Zr1	0.0035 (11)	0.0028 (11)	0.0023 (11)	0.0001 (3)	0,0000	-0.0001(2)
O1	0.006 (3)	0.006 (3)	0.007 (4)	0,0000	0.001 (2)	0,0000
O2	0.005 (2)	0.007 (3)	0.006 (2)	-0.0009(18)	-0.0014(16)	0.0010 (18)
$SrZrO_3$ (V82)						
Zr1	0.0030(6)	0.0020(5)	0.0005(4)	-0.0002(4)	-0.0003(2)	-0.0001(2)
Sr1	0.0075(6)	0.0103(5)	0.0124(4)	0.0006(3)	0	0
O1	0.008(3)	0.016(4)	0.010(3)	0.000(2)	0	0
O2	0.020(3)	0.022(3)	0.011(2)	-0.011(2)	0.003(2)	0.000(2)
$BaZrO_3$ (V92)						
Ba1	0.0042 (2)	0.0042 (2)	0.0042 (2)	0	0	0
Zr1	0.0012 (2)	0.0012 (2)	0.0012 (2)	0	0	0
O1	0.0028 (12)	0.0081 (7)	0.0081 (7)	0	0	0

Table 4.1.8 lists the bond lengths of the three measured perovskite single crystals. As expected the bond lengths of Ca1 – O1 and Ca1 – O2 as well as Sr1 – O1 and Sr1 – O2 vary due to the distortion of the aristotype structure. The $[ZrO_6]^{-2}$ octahedra are also slightly distorted. The average bond length increases from $CaZrO_3$ to $BaZrO_3$ since the ionic radius of the of the cations increase as well which "stretches" the structure.

Table 4.1.8. Selected bond lengths in Å for the grown zirconates (standard deviation in parentheses).

$CaZrO_3$ (V78)			
Atoms (Ca-O)	**Bond length[Å]**	**Atoms (Zr-O)**	**Bond length[Å]**
Ca1—O1	2.332 (6)	Zr1—O2	2.091 (4)
Ca1—O2	2.359 (5)	Zr1—O2	2.093 (4)
Ca1—O1	2.446 (7)	Zr1—O1	2.0955 (18)
Ca1—O2	2.662 (5)	**Average**	**2.093 (3)**
Ca1—O2	2.843 (5)		
Average	**2.528 (5)**		
$SrZrO_3$ (V82)			
Atoms (Sr-O)	**Bond length[Å]**	**Atoms (Zr-O)**	**Bond length[Å]**
Sr1—O1	2.533 (7)	O1—Zr1	2.0884 (13)
Sr1—O2	2.563 (5)	O2—Zr1	2.087 (7)
Sr1—O1	2.747 (8)	**Average**	**2.088 (4)**
Sr1—O2	2.820 (5)		
Average	**2.665 (6)**		
$BaZrO_3$ (V92)			
Atoms (Ba-O)	**Bond length[Å]**	**Atoms (Zr-O, Ba)**	**Bond length[Å]**
Ba1—O1	2.9631 (1)	Zr1—O1	2.0952 (1)
		Zr1—Ba1	3.6291 (2)

The interatomic angles as shown in Table 4.1.9 also vary greatly for the orthorhombic crystals due to the distortion as expected.

Table 4.1.9. Selected interatomic angels for the grown zirconates (standard deviation in parentheses).

$CaZrO_3$ (V78)			
Atoms (O-Ca-O)	**Angles [°]**	**Atoms (O-Zr-O)**	**Angles [°]**
O1—Ca1—O2	106.88 (19)	O2—Zr1—O2	180
O2—Ca1—O2	82.5 (2)	O2—Zr1—O2	89.08 (7)
O1—Ca1—O1	87.31 (17)	O2—Zr1—O1	87.9 (2)
O2—Ca1—O1	134.94 (14)	O2—Zr1—O1	88.0 (2)
O2—Ca1—O2	116.65 (10)		
O1—Ca1—O2	70.47 (11)		
O2—Ca1—O2	158.80 (17)		
$SrZrO_3$ (V82)			
Atoms (O-Sr-O)	**Angles [°]**	**Atoms (O-Zr-O)**	**Angles [°]**
O1—Sr1—O2	115.99 (18)	O2—Zr1—O2	180
O2—Sr1—O2	87.0 (2)	O2—Zr1—O2	89.17 (6)
O1—Sr1—O1	85.3 (2)	O2—Zr1—O1	90.6 (2)
O2—Sr1—O1	127.74 (15)	O2—Zr1—O1	89.4 (2)
O2—Sr1—O2	116.72 (9)	O1—Zr1—O1	180
O1—Sr1—O2	63.85 (17)		
$BaZrO_3$ (V92)			
Atoms (O-Ba-O)	**Angles [°]**	**Atoms (Ba, O-Zr-O, Ba)**	**Angle [°]**
O1—Ba1—O1	180	O1—Zr1—O1	90
O1—Ba1—O1	120	O1—Zr1—O1	180
O1—Ba1—O1	60	O1—Zr1—O1	90
O1—Ba1—O1	60	O1—Zr1—Ba1	54.7
		O1—Zr1—Ba1	125.3
		Ba1—Zr1—Ba1	180
		Ba1—Zr1—Ba1	109.5

The single crystal refinement revealed that $CaZrO_3$ (V78) and $SrZrO_3$ (V82) feature twining. $CaZrO_3$ (V78) is twinned (as contact twin) by a rotation of approximately 90° around [010} (alternative notation: $\{010\}_{90°}$) mono-periodically. $SrZrO_3$ (V82) is twinned (as penetration twin) by a 180° rotation about [101] (alternative notation: {101}) tri-periodically.

Table 4.1.10 shows the charge distribution of the grown zirconate crystals. The charge distribution was calculated with the bond-length/bond-strength model, which was implemented by Brese *et al.* in 1991 [160]. The model uses the most commonly adopted equation:

$$v_{ij} = \exp[\frac{(R_{ij} - d_{ij})}{b}] \qquad (44)$$

where v_{ij} is the bond-valence between atom *i* and *j*, R_{ij} the bond-valence parameter of atom *i* and *j* and d_{ij} the bond length between atom *i* and *j*. The value of *b* is a "universal" constant equal to 0.37 Å [161].

The valence V_i is equal to the sum of the bond-valences of atom *i:*

$$V_i = \sum_i v_{ij} \qquad (45)$$

Table 4.1.10. Charge distribution (Valence; *V*) in V78, V79 and V92, calculated with the bond-length/bond-strength model [160].

	$CaZrO_3$ (V78)			
V_i	**Ca1**	**Zr1**	**O1**	**O2**
	1.69 (3)	3.85 (4)	-1.82 (2)	-1.30 (5)
	$SrZrO_3$ (V79)			
	Sr1	**Zr1**	**O1**	**O2**
	1.75 (2)	3.93 (3)	-1.90 (2)	-1.31 (6)
	$BaZrO_3$ (V92)			
	Ba1	**Zr1**	**O1**	/
	1.72 (2)	3.82 (4)	-1.90 (3)	/

The calculated valences of the various ions differ slightly from the theoretical values (Ca^{2+}, Sr^{2+}, Ba^{2+}; Zr^{4+}; O^{2-}) but are still located within a region which seems logical. The calculation shows that the expected valences are in fact present for the various ions. This also confirms the quality of the single crystal refinement which were calculated with the theoretical valence values.

Group-subgroup relations

As previously mentioned, feature $CaZrO_3$ (V78) and $SrZrO_3$ (V82) twins. The twins are induced by solid state transformation upon cooling from cubic to orthorhombic symmetry. Wang *et al.* reported that certain twins are the result of certain losses of symmetry [162]. The $\{010\}_{90°}$ contact twin of V78 corresponds to the loss of the 4 fold axis of rotation and the {101} penetration twin of V82 to the loss of the mirror plane *m*. Therefore, a view at the group-subgroup relations of V78 and V82 (and subsequently V79) is commendable. The group-subgroup relations will be discussed using the Bilbao Crystallographic Server [163 – 165], specifically the programs CELLSUB [166] and WYCKSPLIT [167]. The maximal ono-isomorphic subgroups were used. Figure 4.1.5 shows the group-subgroup relation diagram starting from the cubic aristotype $Pm\bar{3}m$ (No. 221) and the possible transformation paths to subgroup *Pnma* (No. 62).

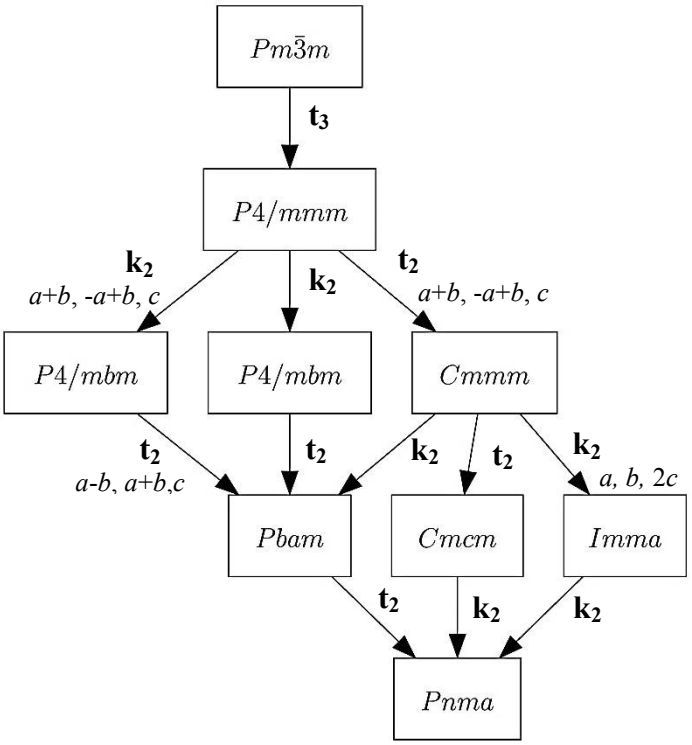

Figure 4.1.6. Group-subgroup diagram starting from $Pm\bar{3}m$ aristotype to *Pnma*. The arrows point to a maximal subgroup. The letters *t* and *k* indicate if the subgroup is "translationsgleich" or "klassengleich". The number describes the index of symmetry reduction. The basis vectors are described as a linear combination of the basis vector of the supergroups (vector sum).

Kennedy *et al.* reported that $SrZrO_3$ is undergoing at least three phase transitions: from cubic ($Pm\bar{3}m$) to tetragonal ($P4/mmm$) to orthorhombic (*Cmcm* and *Pnma*) [168]. This transformation path correlates well with the possible group-subgroup relations in Figure 4.1.6. It can be assumed that the same path is also valid for $CaZrO_3$. By combining the results of Kennedy *et. al* with the group-subgroup relations from Figure 4.1.6, this leads to following transformation path: $Pm\bar{3}m \rightarrow P4/mmm \rightarrow Cmmm \rightarrow Cmcm \rightarrow Pnma$, ($P\,4/m\,\bar{3}\,2/m \rightarrow P\,4/m\,2/m\,2/m \rightarrow C\,2/m\,2/m\,2/m \rightarrow C\,2/m\,2/c\,2_1/m \rightarrow P\,2_1/n\,2_1/m\,2_1/a$) with following transformation matrix:

$$\begin{pmatrix} 1 & 0 & -1 & 0 \\ 0 & 2 & 0 & 0 \\ 1 & 0 & 1 & 0 \end{pmatrix}$$

The Wyckoff positions of Ca1 (in V78), Sr1 (in V82), Zr1 and O1 change during the transformation from cubic to orthorhombic. The Wyckoff position 1b of Ca1 and Sr1 becomes 4c, while the Wyckoff position 1a of Zr1 becomes 4a. The 3d position of O1 undergoes a Wyckoff-splitting resulting in the two Wyckoff positions 8d and 4c (Table 4.1.11).

Table 4.1.11. Change in Wyckoff positions of V78 and V82 (V79) during the transformation from cubic to orthorhombic.

	Wyckoff positions	
	$Pm\bar{3}m$	*Pnma*
Ca1 / Sr1	1*b*	4*c*
Zr1	1*a*	4*a*
O1	3*d*	8*d*, 4*c*

The space group *Pnma* requires a final transformation to *Pcmn* for V78 and *Pbnm* for V82 (V79). This is achieved by transformation of the lattice parameters $a,b,c \rightarrow c,-b,a$ and b,c,a for V78 and V82, respectively. In addition, the point of origin has to be shifted by 1/2, 1/2, 0 for V78 and 1/2, 1/2, 1/2 for V82 (and V79) as well.

4.1.3 Optical analysis

Optical measurements were conducted by Sascha Krüger at the University Siegen. The crystals were sliced and polished prior to the optical transmission experiments.
However, the slices had proved to be opaque, making any reliable measurement impossible. Therefore, the samples were grinded to a powder for optical reflection experiments.

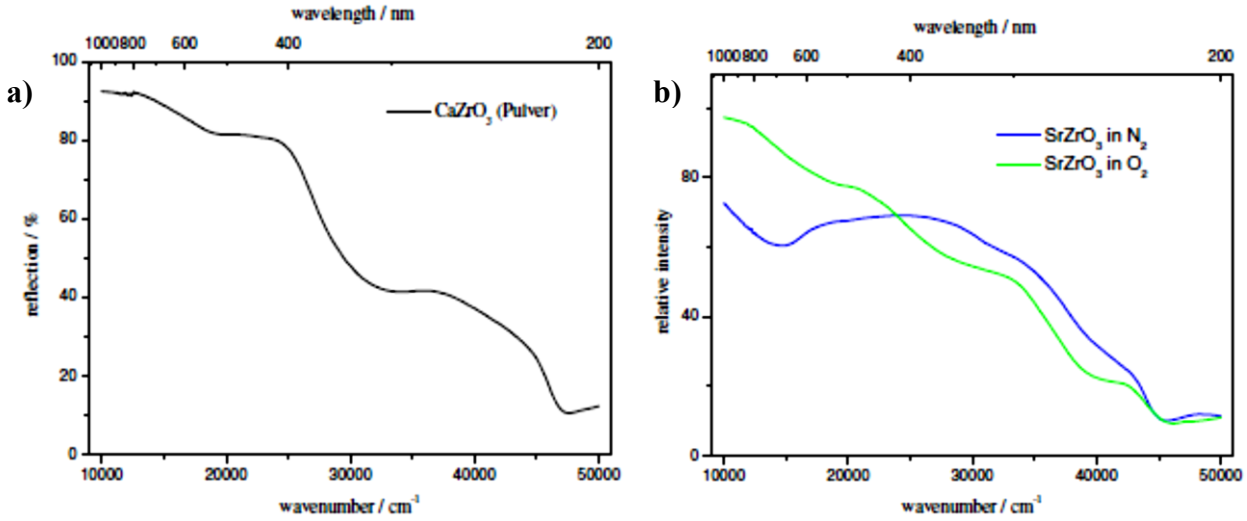

cont.

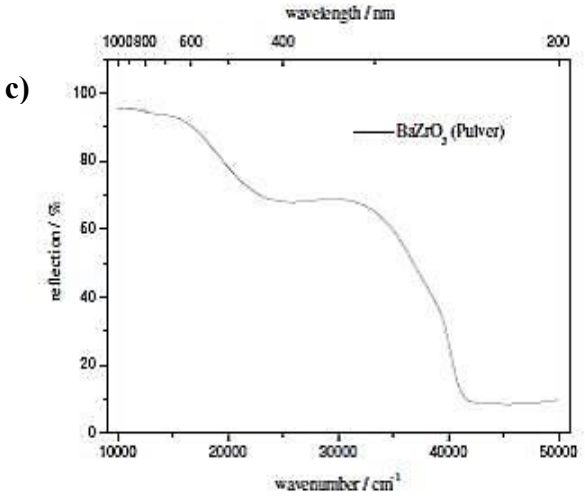

Figure 4.1.7. Reflection spectra of a) $CaZrO_3$, b) $SrZrO_3$ (V79 and V82) and c) $BaZrO_3$.

Figure 4.1.7 shows the reflection spectra of the grown zirconate crystals. V78 displays several optical reflection-bands in its spectrum with the most intense lying in the blue spectral region explaining the pink/red colorization of the crystal. V92 also displays, similar to V78, several optical reflection-bands.

The most intense reflection-band is lying in the green spectral region of light which explains the orange color of the crystal. V79 and V82 display several reflection-bands (i.e. 1000 cm^{-1} to 2000 cm^{-1}, 30000 cm^{-1} and 40000 cm^{-1}). However, a comparison of both samples shows that the spectra differ from each other. The lower wavenumbers and absorption maxima vary the most. Compared to V79, V82 has a distinct reflection-band at 15000 cm^{-1} which shows that red spectrum of light is absorbed more. This explains the blue colorization. The absorption maximum of V82 lies at much lower energy compared to the absorption maximum of the V79 sample. It was suggested that the difference in the optical spectra between V79 and V82 can be explained from the possible incorporation of nitrogen in the structure of V82 due to the growth process under N_2 atmosphere. Therefore, a nitrogen/oxide analysis has been conducted by Steven Orthmann (AK Lerch, Technische Universität Berlin, Berlin). The measurement detected no significant nitrogen concentration. However, the limit of detection (LOD) lies at approximately 0.5 mass % and the optical effects of V82 can be induced by much lower concentrations of nitrogen incorporated in the lattice. Therefore, it can be assumed that a very small amount of nitrogen (in the range of ppm) is causing the difference in the reflection spectra between V79 and V82. The absorption lies at 40000 cm^{-1} corresponds to the emission of the luminescence. This can be seen by the comparison of reflection and emission spectra of the samples (Figure 4.1.8).

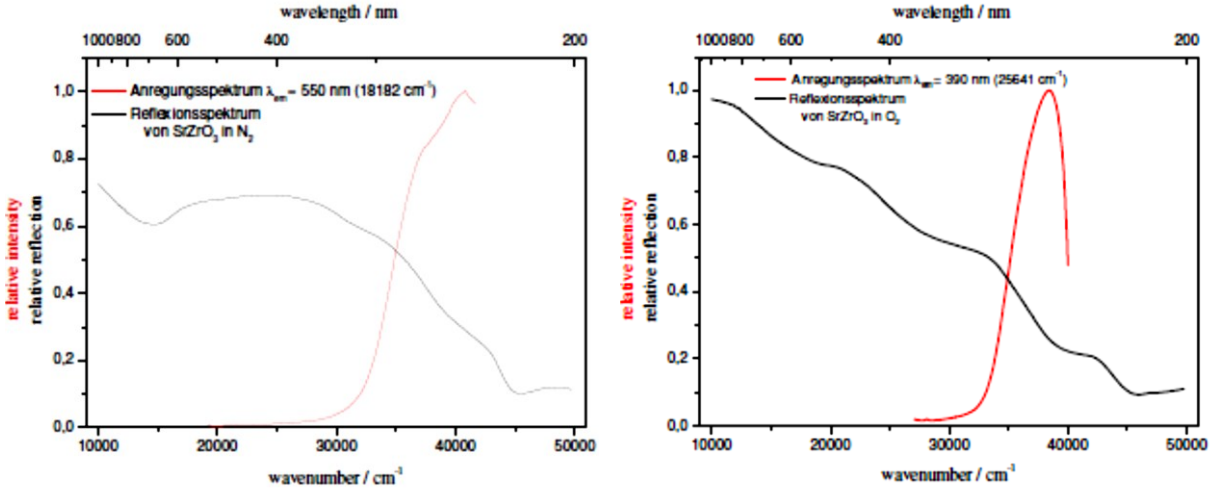

Figure 4.1.8. Reflection and emission spectra of V79 (right) and V82 (left), respectively

A severe difference of V79 and V82 can be seen in the luminesce effect of the samples as shown in Figure 4.1.9. The maxima of the emission spectra have a difference of approximately 6000 cm^{-1} to each other and a shift of 160 nm.

Again, it was suggested that, again, the incorporation of nitrogen in the crystal lattice has influence on the fluorescent emission spectrum. By comparing the reflection spectra of all samples it is evident that the band gap is shifting towards lower energies from $CaZrO_3$ to $BaZrO_3$. However, the spectra are also very complex in nature and which makes a detailed interpretation very difficult.

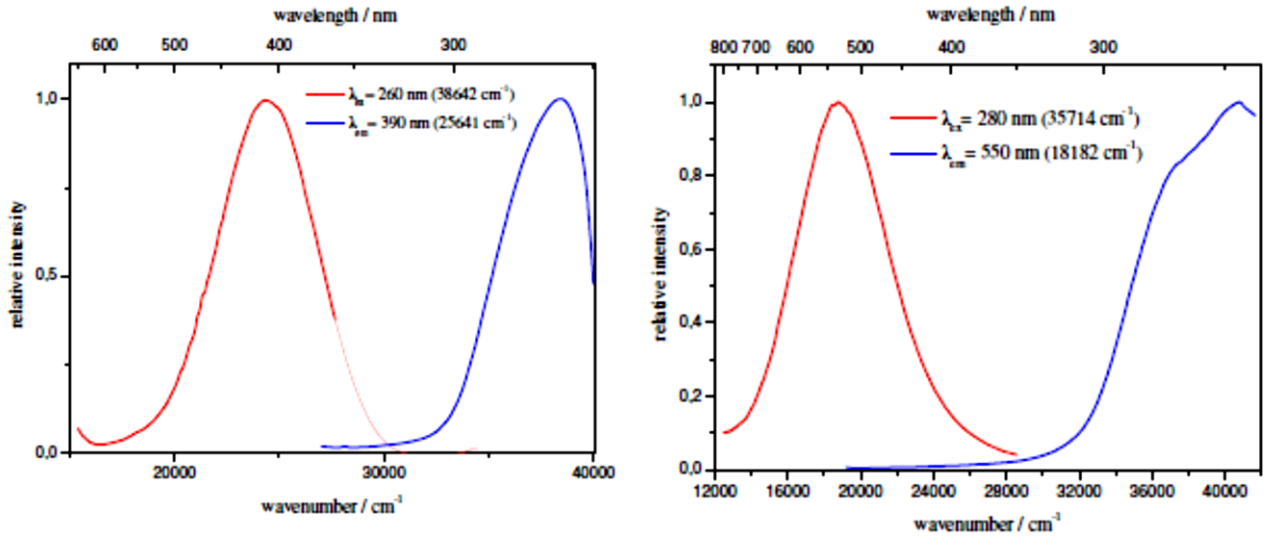

Figure 4.1.9. Excitation and emission spectra of V79 (right) and V82 (left) at room temperature

4.1.4 $CaZrO_3$ substrates

The large V78 single crystals were used as substrate material for multiferroic thin films. Multiferroic materials possess interesting properties such as simultaneously ferroelectricity, ferromagnetism and ferroelasticity and its magneto-electric coupling is expected to be used for various functional devices [169]

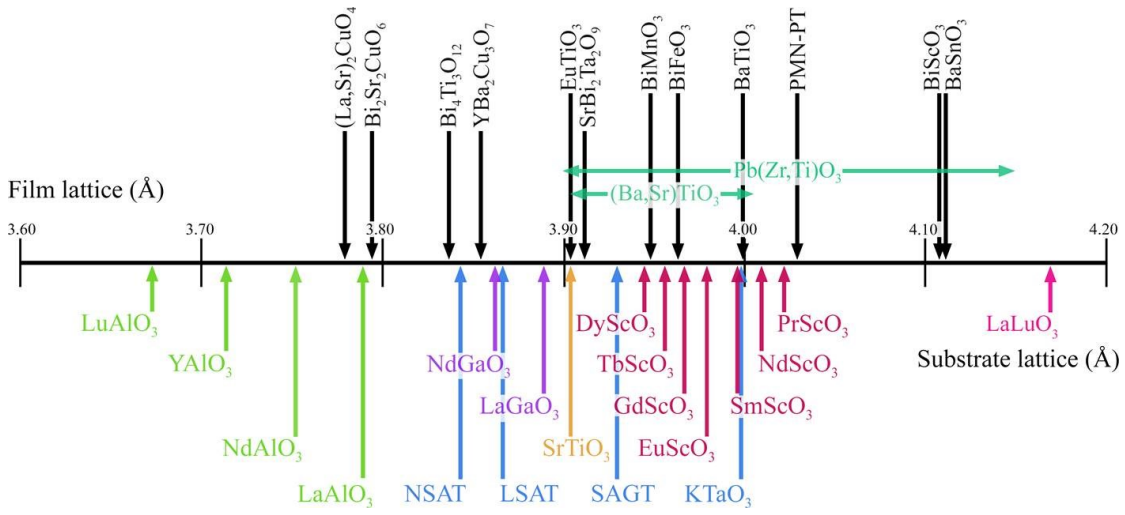

Figure 4.1.10. Perovskites used as substrates for multiferroic materials with lattice parameters from 3.60 – 4.20 Å (Figure provided by Dr. Reinhard Uecker, IKZ, Berlin).

Figure 4.1.10 shows the available substrates for multiferroic materials with a lattice parameter range from 3.6 Å to 4.2 Å. A lack of suitable substrate materials is present from a lattice parameters of 4 Å and above (with exception of $LaLuO_3$ and some scandate materials). The grown zirconate single crystals are promising candidates to fill this gap due to their lattice parameters ($CaZrO_3$; pseudo-cubic 4.01 Å, SrZrO3; pseudo-cubic 4.10 Å and $BaZrO_3$; cubic 4.19 Å). Since the needed single crystals have to be fairly large to get substrates with practical use only the $CaZrO_3$ single crystals remained as suitable candidate. Therefore, the crystals were therefore cut along the pseudo-cubic axis [101], polished and annealed at 1000 °C for 1 hour under a pure oxygen atmosphere. The surfaces of the polished crystals were analyzed by atomic force microscopy (AFM) as seen in figure 4.1.11.

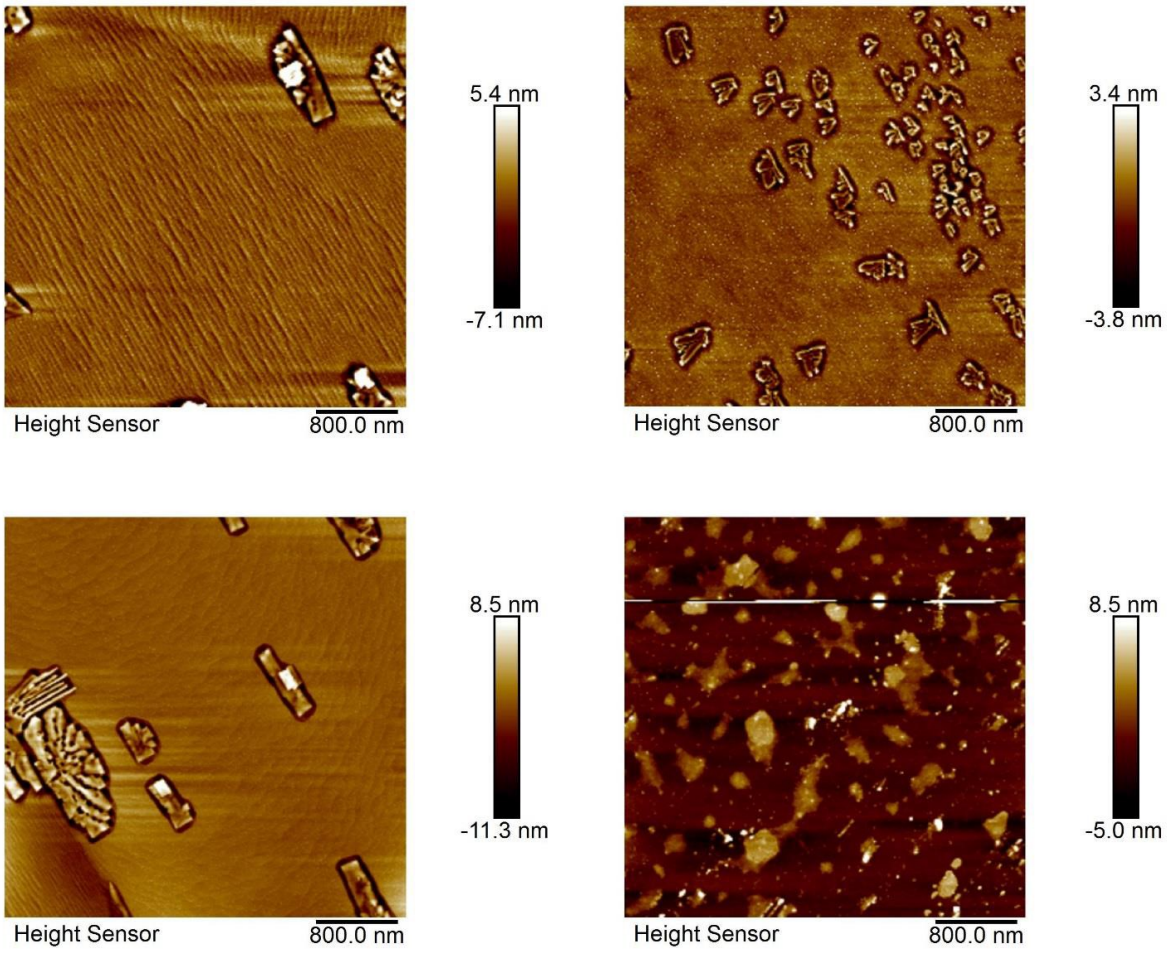

Figure 4.1.11. AFM images of four separate $CaZrO_3$ surfaces after the polishing and annealing. Small cluster are visible on the inhomogeneous surfaces.

The samples exhibit very rough surfaces and little to no homogeneity even after the polishing. Small cluster are formed on the surfaces increasing the roughness even more. The magnitude of this effect also varies strongly from sample to sample. Nevertheless, the substrates were used for growth experiments of $K_{0.8}Na_{0.2}NbO_3$ thin films with a thickness of 20 – 25 nm. The grown films have then been analyzed with AFM. The results are shown in Figure 4.1.12.

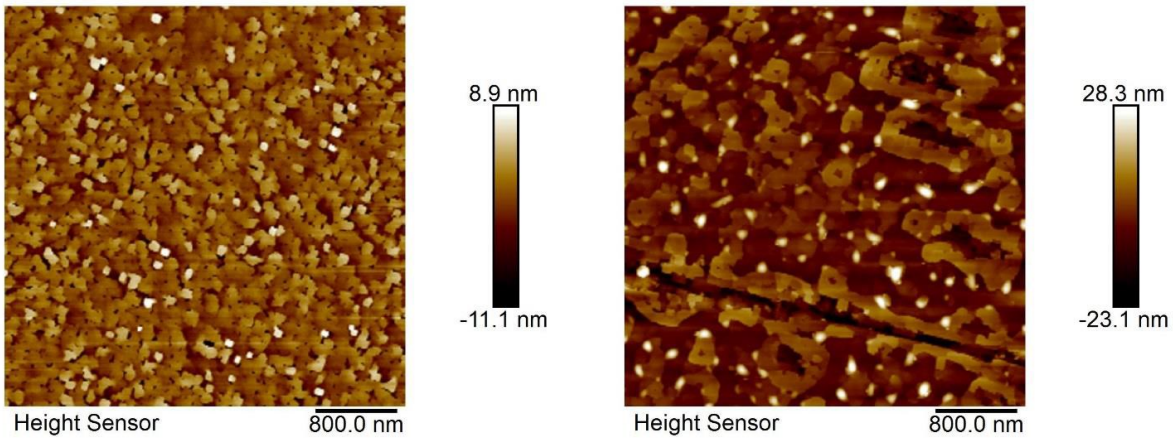

Figure 4.1.12. AFM images of two different $K_{0.8}Na_{0.2}NbO_3$ thin films grown on $CaZrO_3$ substrates.

The surfaces of the grown thin films suffer from the same roughness as the substrates. The formation of cluster are also present as well as the inhomogeneous appearance of this effect from sample to sample (Figure 4.1.11). However, the high resolution X-ray diffraction measurements show that $K_{0.8}Na_{0.2}NbO_3$ thin films were successfully grown on the $CaZrO_3$ substrates with no appearance of a secondary phase (Figure 4.1.13).

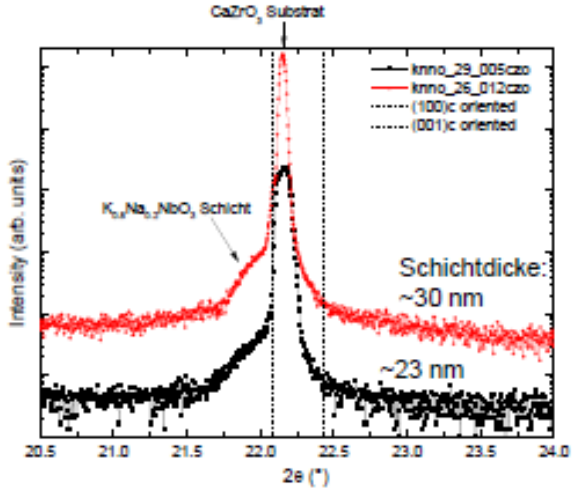

Figure 4.1.13. High resolution X-ray diffraction pattern of $K_{0.8}Na_{0.2}NbO_3$ thin films grown on $CaZrO_3$ substrates.

In addition, no shift in the reflection positions of substrate and thin film are seen indicating that no lattice tension was created due to the growth process. However, the reflections appear very broad with FWHM (full width at half maximum) of approx. 0.4 ° which indicates a poor ordering and therefore a poor crystal quality even for the very thin film. The substrate itself shows also a very broad reflection with a FWHM of approx. 0.2 ° or 720 arcsec which was expected after the inhomogeneous AFM images. The poor quality of the substrate, and subsequently the thin film, can be explained by the twinning effect present in the $CaZrO_3$. The twins create additional defects, hereby, disrupting the lattice.

4.1.5 Conclusion

The grown alkaline zirconates, namely $CaZrO_3$, $SrZrO_3$ and $BaZrO_3$ are the first grown single crystals of their kind and were therefore the first who are structurally described as single crystals in this thesis. They were needed for optical measurements at the University of Siegen and as substrates for multiferroic materials. $SrZrO_3$ single crystals were grown twice, one time under normal air atmosphere and one time under nitrogen atmosphere of 1350 mbar. All the zirconates belong to the perovskite structure type. Powder and single crystal diffraction experiments revealed that $CaZrO_3$ and $SrZrO_3$ have an orthorhombic structure (space group *Pcmn, a* = 5.762 Å, *b* = 8.017 Å and *c* = 5.590 Å and *Pbnm a* = 5.791 Å, *b* = 5.824 Å and *c* = 8.205 Å) while $BaZrO_3$ exhibiting cubic aristotype ($Pm\bar{3}m$, *a* = 4.19 Å). According to the classification proposed by Glazer, $CaZrO_3$ and $SrZrO_3$ belong to the $a^- b^+ a^-$ category while $BaZrO_3$ can be described as $a^0 a^0 a^0$. Both the orthorhombic $CaZrO_3$ and $SrZrO_3$ feature twins. $CaZrO_3$ is twinned as contact twin by a rotation of approximately 90° around [010] mono-periodically. $SrZrO_3$ is twinned as penetration twin by a 180° rotation about [101] tri-periodically. The twinning is induced by the transformation of the high symmetry cubic phase at higher temperatures to the lower symmetric tetragonal and finally orthorhombic phase. The loss of symmetry creates the twins. The transformation path described by the group-subgroup relations is as follows: $Pm\bar{3}m \rightarrow P4/mmm \rightarrow Cmm \rightarrow Cmcm \rightarrow Pnma$. The single oxygen position conducts a Wyckoff splitting into two positions from cubic to orthorhombic. The optical reflectance spectroscopy measurements reveal complex spectra for all zirconate single crystals. Especially the $SrZrO_3$ samples are showing luminescence effects at wavelengths of 260 to 280 nm. A strong difference of 160 nm is noted on the emission wavelength of the $SrZrO_3$ grown under air and the one grown under nitrogen atmosphere.

This difference was suggested to be caused from small amounts of nitrogen incorporated in $SrZrO_3$ which couldn't be detected with the methods at hand. $CaZrO_3$ was used as a substrate for multiferroic materials, since it was the only crystal with suitable dimensions and lattice parameters. Therefore, $K_{0.8}Na_{0.2}NbO_3$ was successfully grown as layer on the $CaZrO_3$ substrate. However, the twins present in the $CaZrO_3$ crystals lead to a poor quality of the grown layer, with a rough surface and cluster formation.

4.2 M:TiO_2 (M = Ni, Fe, Co, Mn, Nb)

Five TiO_2 based single crystals with transition metal dopants (Ni, Fe, Co, Mn and Nb) were successfully grown and examined as part of this thesis. The goal was to synthesize TiO_2 single crystals which feature a lower optical bandgap than pure TiO_2 (bandgap of ~3 eV).

4.2.1 Single crystal growth

It was necessary to prepare the titania material prior to the growth experiments by solid state reaction. NiO (99.9 %), Fe_2O_3 (99.9 %), Co_3O_4 (99.99 %), $MnCO_3$ (99.9 %) or Nb_2O_5 (99.9 %) were mixed homogenously in the correct stoichiometry with TiO_2 (99 %) and air fired in an alumina crucible at a temperature of 950 °C for 12 h. The exact composition and solid state reaction parameters are listed in Table 4.2.1. The resulting *M*:TiO_2 (*M* = Ni, Fe, Co, Mn, Nb) powders could then be filled in the Skull-crucible for the growth experiment.
During the melt process. the solid surface of the material tended to break, hereby, revealing the melt. This resulted in a large heat emission, disrupting the solid-melt equilibrium. Therefore, the ignition metals have been laid deeper in the material, at a depth of approximately 3 cm. This would result in a thicker upper surface of the material, therefore, minimizing the risk of breaking. The grown single crystal will be referred to as V87, V88, V89, V104 and V108 for Ni:TiO_2, Fe:TiO_2, Co:TiO_2, Mn:TiO_2 and Nb:TiO_2, respectively.

Table 4.2.1. **S**toichiometry and solid state reaction parameters of *M*:TiO2 (*M* = Ni, Fe, Co, Mn, Nb) which were prepared prior to the single crystal growth experiment.

V87 $Ni_{0.0075}Ti_{0.9925}O_{2-\delta}$		V88 $Fe_{0.0075}Ti_{0.9925}O_{2-\delta}$		V89 $Co_{0.0075}Ti_{0.9925}O_{2-\delta}$	
Compound	**mass [g]**	**Compound**	**mass [g]**	**Compound**	**mass [g]**
Titanium(IV) oxide; TiO_2	1189	Titanium(IV) oxide; TiO_2	1189	Titanium(IV) oxide; TiO_2	1189
Nickel oxide; NiO	8.2	Iron(III) oxide; Fe_2O_3	9.4	Cobalt(II,III) oxide; $CoO + Co_2O_3$	9
Sum	1197.2	**Sum**	1198.4	**Sum**	1198

Solid state reaction parameters			
Temperature [°C]	950		
Time [h]	12		
V104 $Mn_{0.0015}Ti_{0.9975}O_{2-\delta}$		V108 $Nb_{0.0005}Ti_{0.9995}O_{2+\delta}$	
Compound	**mass [g]**	**Compound**	**mass [g]**
Titanium(IV) oxide; TiO_2	1196.2	Titanium(IV) oxide; TiO_2	1596
Manganese(II) carbonate; $MnCO_3$	2.6	Niobium(V) oxide; Nb_2O_5	1.3
Sum	1198.2	**Sum**	1597.3
Solid state reaction parameters			
Temperature [°C]	950	1350	
Time [h]	12	12	

The growth experiment was conducted under normal air atmosphere conditions with approximately 5 g Titanium serving as ignition metal (Table 4.2.2).

Table 4.2.2. Operating parameters for the growth of *M*:TiO_2 (*M* = Ni, Fe, Co, Mn, Nb).

	Ni:TiO_2 (V87)	**Fe:TiO_2 (V88)**	**Co:TiO_2 (V89)**	**Mn:TiO_2 (V104)**	**Nb:TiO_2 (V108)**
Ignition metal	Ti; 5 g	Ti; 5 g	Ti; 5.2 g	Ti; 5.6 g	Ti; 6.5 g
Growth atmosphere	Air; 1 bar	Air; 1 bar	Air; 1 bar	Air; 1 bar	Air; 1 bar
Parameters at idle position					
Voltage [%]	51.5	48	52	53	45
Current [%]	22	22	21.5	22	21
Power output [%]	11.5	10.5	10	10.5	8.5

The crucible was kept at the idle position between 30 min and 1 hour to achieve a good homogenization of the melt prior to the growth.

Table 4.2.3. Growth parameters (speed and time) for *M*:TiO_2 (*M* = Ni, Fe, Co, Mn, Nb).

	Ni:TiO_2 (V87)	**Fe:TiO_2 (V88)**	**Co:TiO_2 (V89)**	**Mn:TiO_2 (V104)**	**Nb:TiO_2 (V108)**
Speed	**Time**				
Idle phase	1 h	30 min	30 min	30 min	30 min
1 mm/h	/	1 h	1 h 30 min	/	/
3 mm/h	/	/	/	/	/
6 mm/h	1 h 30 min.	1 h	1 h	1 h	1 h
9 mm/h	1 h	1 h	1 h	1 h	1 h
12 mm/h	1 h 30 min	/	30 min	1h 30 min	1 h
15 mm/h	1 h	45 min	/	/	1h 30 min
18 mm/h	/	/	/	1h	/
Sum	**6 h**	**4 h 15 min**	**4 h 30 min**	**5 h**	**5 h 30 min**

The growth experiments took approximately 4 to 6 hours to complete, starting with a growth speed of 1 mm/h with gradually increasing speed up to 18 mm/h (Table 4.2.3). All grown titania crystals have an elongated shape with varying dimensions. They have a black color and are overall opaque with a metallic glance. V87 has a length of approximately 1 cm and a width of 0.4 cm (1 x 0.4 x 0.4 cm^3). The crystals sizes decrease from V87 to V89 with lengths of 0.6 cm and 0.4 cm as well as widths of 0.3 cm and 0.2 cm for V88 and V89, respectively (V88: 0.6 x 0.3 x 0.3 cm^3; V89: 0.4 x 0.2 x 0.2 cm^3). The sizes of V104 and V108 are larger compared to V87 with lengths of 1.1 and 1.2 cm as well as widths of 0.5 and 0.6 cm for V104 and V018 respectively (Figure 4.2.1). Heat treatments at 1000 °C under pure oxygen atmosphere were conducted on all five Titania single crystals. The treatment oxidized the dopants as well as the Ti^{3+} to Ti^{4+} which altered the colorization of the crystals. All crystals obtained a red to orange color of varying shades, with exception of V108 Nb:TiO_2 which got a green to yellow colorization.

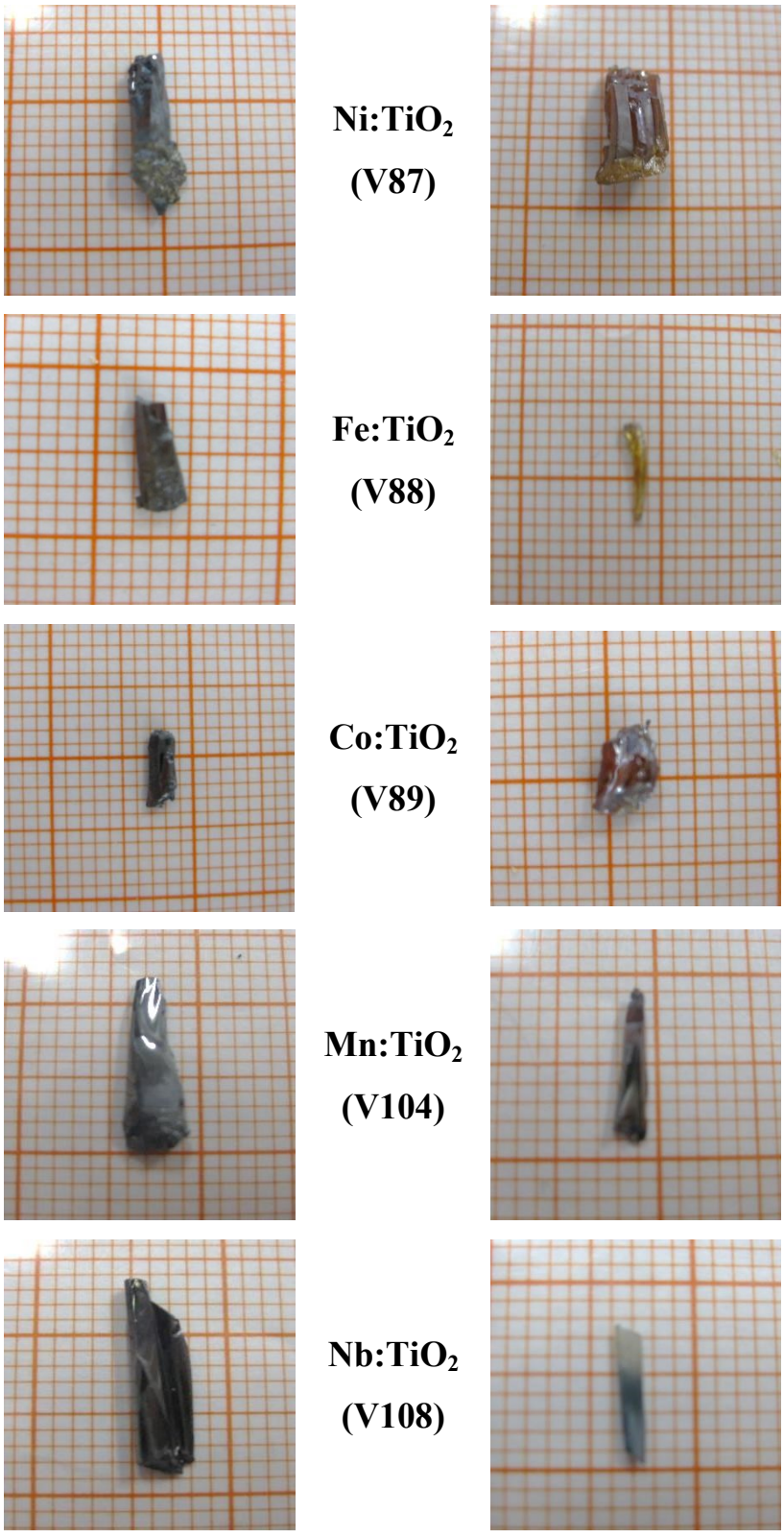

Figure 4.2.1. Titania single crystals of Ni:TiO_2 (V87), Fe:TiO_2 (V88), Co:TiO_2 (V89), Mn:TiO_2 (V104) and Nb:TiO_2 (V108); as-grown (left) and heat treated by 1000 °C under pure O_2 atmosphere for 12 h.

4.2.2 Structural analysis

The first structural characterization was achieved via X-ray powder diffraction analysis and Rietveld refinement.

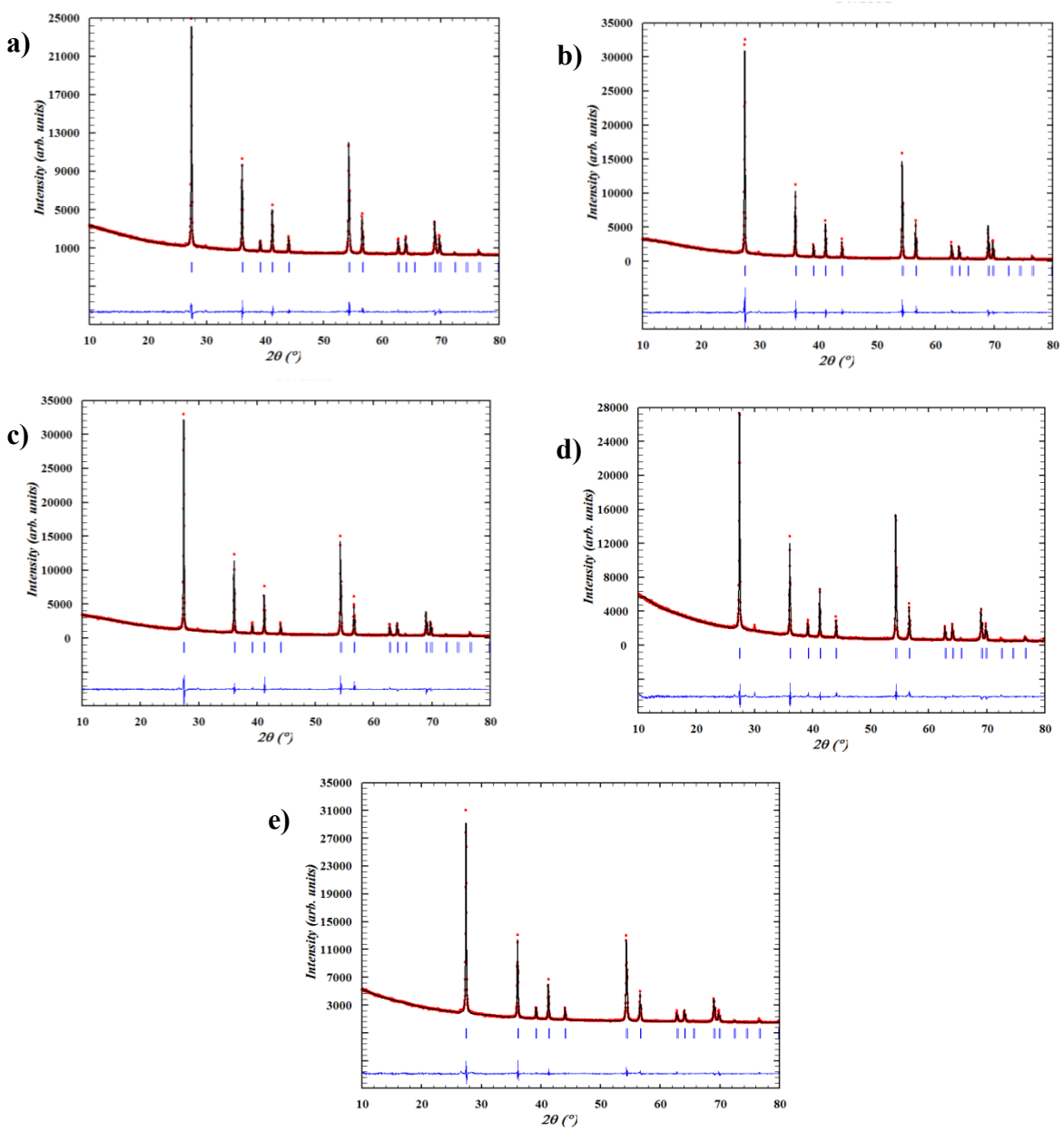

Figure 4.2.2. X-ray powder diffraction diagrams of a) Ni:TiO_2 (V87) b) Fe:TiO_2 (V88) c) Co:TiO_2 (V89) d) Mn:TiO_2 (V104) and e) Nb:TiO_2 (V108) with the graphical interpretation of the Rietveld refinement.

Figure 4.2.2 shows the X-ray powder diffraction patterns of the grown titania crystals, with the completed Rietveld fit.

All samples have a tetragonal structure (rutile structure) and were refined using space group $P4_2/mnm$ (No. 136) with two formula units per cell. The lattice parameters are a = 4.5957 Å and c = 2.9594 Å for V87, a = 4.5955 Å and c = 2.9598 Å for V88, a = 4.5952 Å and c = 2.9595 Å for V89, a = 4.5936 Å and c = 2.9575 Å for V104, a = 4.5948 Å and c = 2.9581 Å for V108. Table 4.2.4 lists the lattice parameters and selected values of the Rietveld refinement. The goodness of fit varies from 1.13 – 2.47, which correspond to a good fit of the structure.

Table 4.2.4. Results of the Rietveld refinement of the titania samples (standard deviations in parentheses where applicable).

	Ni:TiO_2 (V87)	**Fe:TiO_2 (V88)**	**Co:TiO_2 (V89)**
Space group	$P4_2/mnm$	$P4_2/mnm$	$P4_2/mnm$
Lattice parameter [Å]	a = 4.59569 (11) c = 2.95942 (7)	a = 4.59549 (11) c = 2.95976 (7)	a = 4.59521 (11) c = 2.95949 (7)
R_{wp}	5.50	7.44	6.98
R_{exp}	3.16	3.01	2.95
R_{Bragg}	3.50	3.85	3.99
S	1.74	2.47	2.37

	Mn:TiO_2 (V104)	**Nb:TiO_2 (V108)**
Space group	$P4_2/mnm$	$P4_2/mnm$
Lattice parameter [Å]	a = 4.59365 (11) c = 2.95754 (8)	a = 4.59479 (12) c = 2.95813 (8)
R_{wp}	3.05	2.77
R_{exp}	2.41	2.46
R_{Bragg}	5.48	3.24
S	1.26	1.13

The Bragg-*R* factors have all approximately the same magnitude with the exception of V104 with a slightly higher Bragg-R factor of 5.48. However, the value still lies within the accepted range. Laue-diffraction experiments have been conducted to determine the single crystal nature of the material.

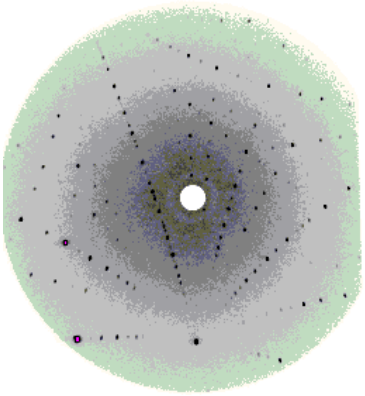

Ni:TiO_2 (V87)

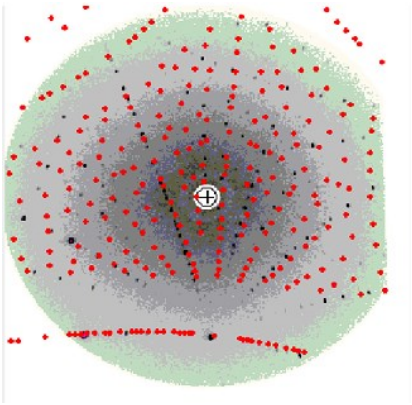

[230]

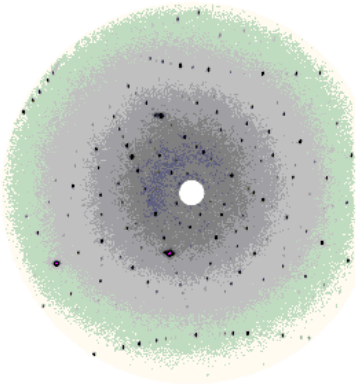

Fe:TiO_2 (V88)

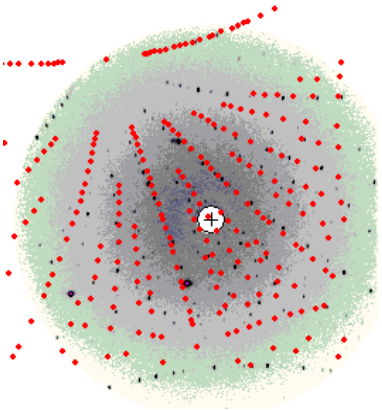

[411]

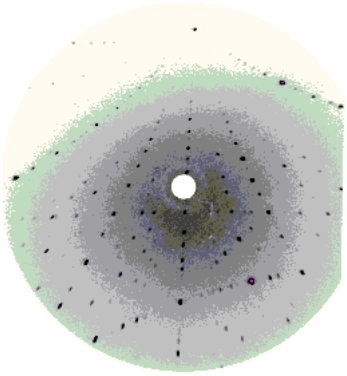

Co:TiO_2 (V89)

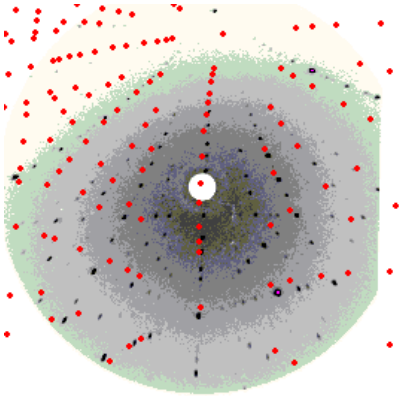

[21$\bar{1}$]

cont.

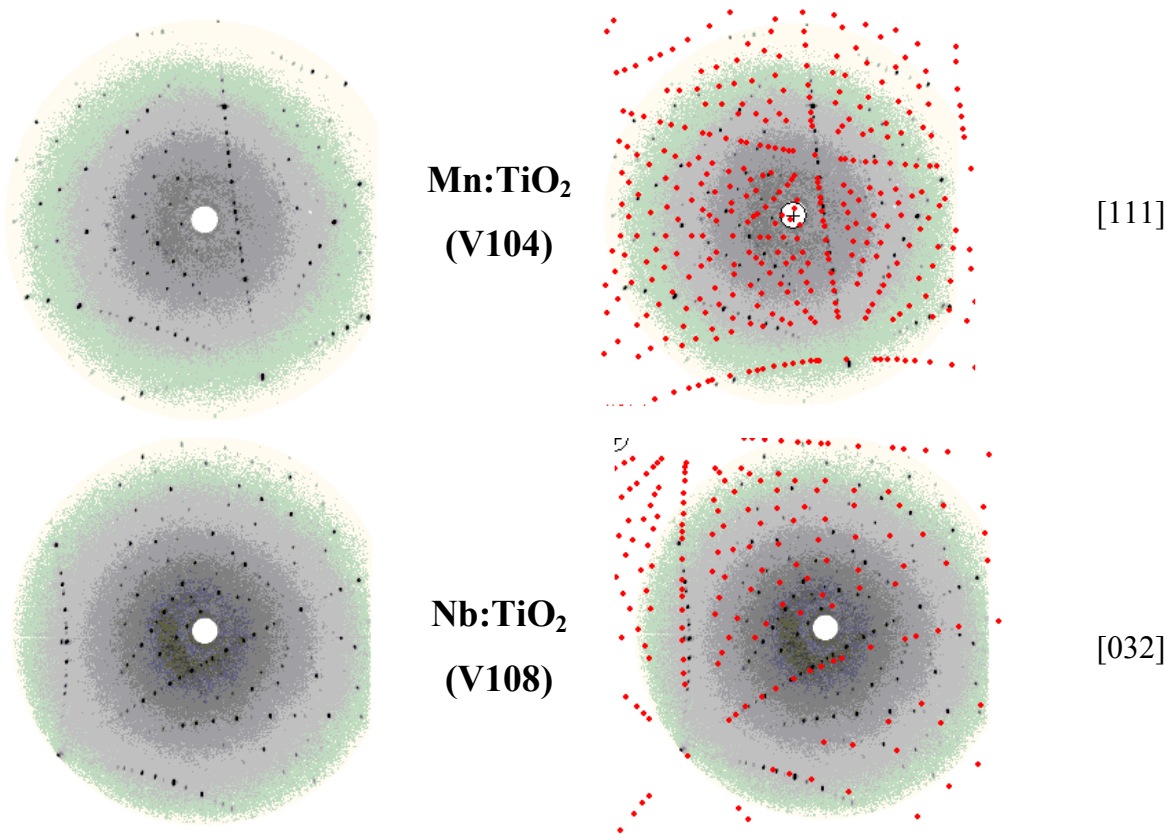

Figure 4.2.3. Laue Diffraction pattern of the grown titania single crystals; As measured (left) and with overlaid simulated Laue structure patterns.

Figure 4.2.3 shows the Laue diffraction patterns (reflection) of the titania single crystals. TAll patterns show diffracted points, which indicate a single crystal nature of the materials. By using the software Orient express, simulated structure patterns have been generated and laid over the Laue images. The structure patterns were then adjusted by varying the *x, y* and *z* coordinates to fit the structure pattern of the Laue image. The orientation of the Laue images appear to be oriented towards [230] for V87, [411] for V88, [21$\bar{1}$] for V89, approximately [111] for V104 and [032] for V108. The corresponding Laue group for the space group $P4_2/mnm$ is $P4/mmm$. In addition to the Laue diffraction, single crystal diffraction experiments have been conducted to investigate the single crystal nature of the materials. The results are presented in the following Tables (Tables 4.2.5 – 4.2.10).

Table 4.2.5. Results of the single crystal refinement of the grown titania single crystals (standard deviations in parentheses where applicable); continuation on the following page

Sample	**Ni:TiO_2 (V87)**	**Fe:TiO_2 (V88)**	**Co:TiO_2 (V89)**
Molar mass (g mol^{-1})	79.88	79.9	79.91
Crystal system	tetragonal	tetragonal	tetragonal
Space Group	$P4_2/mnm$ (136)	$P4_2/mnm$ (136)	$P4_2/mnm$ (136)
Radiation	MoK_a (λ = 0.71 Å)	MoK_a (λ = 0.71 Å)	MoK_a (λ = 0.71 Å)
Temperature (K)	150.1 (8)	149.95 (10)	151 (5)
a (Å)	4.5852 (2)	4.5914 (2)	4.5930 (1)
b (Å)	4.5852 (2)	4.9514 (2)	4.5930 (1)
c (Å)	2.9562 (2)	2.9543 (2)	2.9560 (1)
V ($Å^3$)	62.151 (7)	62.279 (7)	62.360 (3)
Formula units per cell	2	2	2
Calculated density (g cm^{-3})	4.270	4.260	4.255
F(000) (e)	76	76	76
Crystal size (mm^3)	0.38 x 0.19 x 0.14	0.35 x 0.30 x 0.16	0.42 x 0.23x 0.17
Absorption coefficient (mm^{-1})	6.229	6.181	6.207
Absorption correction	analytical	analytical	analytical
θ range (°)	6.29 - 32.34	6.28 - 32.33	6.28 - 32.31
Range in hkl	$6 \leq h \leq 6$	$6 \leq h \leq 6$	$6 \leq h \leq 6$
	$6 \leq k \leq 6$	$6 \leq k \leq 6$	$6 \leq k \leq 6$
	$4 \leq l \leq 4$	$4 \leq l \leq 4$	$4 \leq l \leq 4$
Total no. of reflections	76	75	76
Independent reflections	76	75	76
Reflections with $I > 2\ \sigma(I)/R\sigma$	76	75	76
Ref. parameters	0.0164	0.0391	0.0373
Goodness of fit on Fi^2	1.299	1.230	1.361
Final indices R_1/wR_2 [$I > 2\sigma(I)$]	0.0164	0.126	0.0122
Final indices $R1/wR2$ (all data)	0.0164	0.126	0.0122
Largest diff. peak and hole (e $Å^{-3}$)	0.411 / -0.409	0.386 / -0.260	0.269 / -0.425

cont.

Sample	**Mn:TiO_2 (V104)**	**Nb:TiO_2 (V108)**
Molar mass (g mol^{-1})	79.89	79.92
Crystal system	tetragonal	tetragonal
Space Group	$P4_2/mnm$ (136)	$P4_2/mnm$ (136)
Radiation	MoKa (λ = 0.71 Å)	MoK_a (λ = 0.71 Å)
Temperature (K)	149.95 (10)	149.9 (6)
a (Å)	4.58460 (10)	4.5854 (2)
b (Å)	4.58460 (10)	4.5854 (2)
c (Å)	2.9529 (2)	2.9510 (2)
V ($Å^3$)	62.066 (10)	62.047 (7)
Formula units per cell	2	2
Calculated density (g cm^{-3})	4.27	4.28
F(000) (e)	76	76
Crystal size (mm^3)	0.39 x 0.20 x 0.14	0.87 x 0.33 x 0.25
Absorption coefficient (mm^{-1})	6.208	6.206
Absorption correction	analytical	analytical
θ range (°)	6.293 - 32.257	6.29 - 32.37
Range in *hkl*	$6 \leq h \leq 6$	$6 \leq h \leq 6$
	$6 \leq k \leq 6$	$6 \leq k \leq 6$
	$4 \leq l \leq 4$	$4 \leq l \leq 4$
Total no. of reflections	75	76
Independent reflections	75	76
Reflections with $I > 2\ \sigma(I)/R\sigma$	75	76
Ref. parameters	0.0403	0.0484
Goodness of fit on Fi^2	1.249	1.258
Final indices R_1/wR_2 [I > 2σ(I)]	0.0130	0.0173
Final indices R1/wR2 (all data)	0.0130	0.0173
Largest diff. peak and hole (e $Å^{-3}$)	0.275 / -0.358	0.508 / -0.404

The absorption coefficients of the five crystals were very high resulting in a low total number of reflections. The refinement of the single crystal data shows an tetragonal structure for all the crystals ($P4_2/mnm$) with lattice parameters of a = 4.5852 Å and c = 2.9562 Å for V87, a = 4.5914 Å and c = 2.9543 Å for V88, a = 4.5929 Å and c = 2.9562 Å for V89, a = 4.5846 Å and c = 2.9529 Å for V104, a = 4.5854 Å and c = 2.9510 Å for V108. These values correlate very well with the powder diffraction data. The following tables summarize the atomic coordinates, Wyckoff positions and anisotropic displacement factor as well as selected values for the bond lengths and interatomic angles which resulted from the refinement of the single crystals.

Table 4.2.6. Wyckoff positions and atomic coordinates for the grown titania (standard deviation in parentheses).

Atom	Wyck.	*x*	*y*	*z*
Ni:TiO_2 (V87)				
Ti1	2*a*	0	0	0
Ni1	2*a*	0	0	0
O1	4*f*	0.30512 (13)	0.301512 (13)	0
Fe:TiO_2 (V88)				
Ti1	2*a*	0	0	0
Fe1	2*a*	0	0	0
O1	4*f*	0.30494 (12)	0.30494 (10)	0
Co:TiO_2 (V89)				
Ti1	2*a*	0	0	0
Co1	2*a*	0	0	0
O1	4*f*	0.30482 (15)	0.30482 (15)	0
Mn:TiO_2 (V104)				
Ti1	2*a*	0	0	0
Mn1	2*a*	0	0	0
O1	4*f*	0.30508 (13)	0.30508 (13)	0
Nb:TiO_2 (V108)				
Ti1	2*a*	0	0	0
Nb1	2*a*	0	0	0
O1	4*f*	0.30479 (19)	0.30479 (19)	0

The anisotropic displacement factors are tensors. These tensors Uij are the squares of the displacements of the electron density function from the coordinates in the structure. The diagonal U_{11}, U_{22}, and U_{33} consider the displacements along the cell edges and the other elements the displacements at the angle to the cell edges. Figure 4.2.4 shows this in the thermal ellipsoid plot (Fe:TiO_2 as example). The parameters shown in Table 4.2.7 indicate a greater displacement along the cell edges. The displacements are equal for the all diagonal $U_{11,}$ U_{22} and U_{33} elements and almost zero for the other elements.

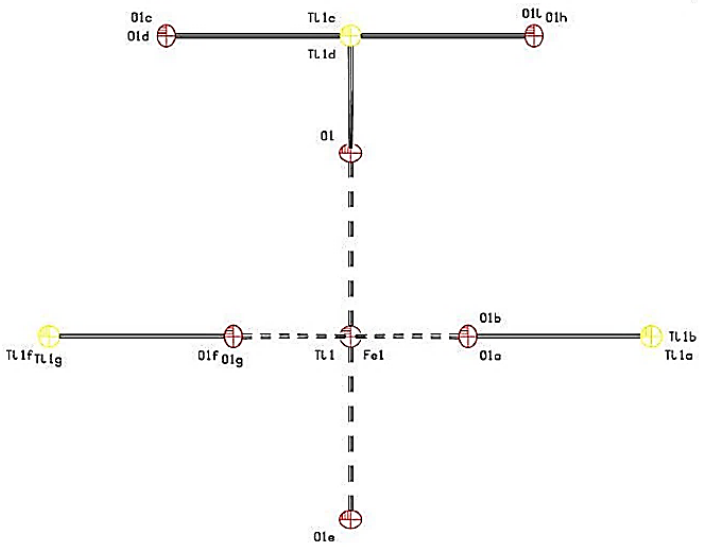

Figure 4.2.4. Thermal ellipsoid plot (50% probability) of Fe:TiO_2 (V88). The O1 positions can be seen as ellipsoids

Table 4.2.7. Anisotropic displacement parameters for the grown titania single crystals (standard deviation in parentheses).

Atom	U_{11}	U_{22}	U_{33}	U_{12}	U_{13}	U_{23}
Ni:TiO_2 (V87)						
Ti1	0.0049 (3)	0.0049 (3)	0.0042 (4)	0.00007 (7)	0	0
Ni1	0.0049 (3)	0.0049 (3)	0.0042 (4)	0.00007 (7)	0	0
O1	0.0043 (4)	0.0043 (4)	0.0040 (6)	-0.0007 (2)	0	0
Fe:TiO_2 (V88)						
Ti1	0.0055 (3)	0.0055 (3)	0.0040 (3)	-0.00003 (6)	0	0
Fe1	0.0055 (3)	0.0055 (3)	0.0040 (3)	-0.00003 (6)	0	0
O1	0.0050 (4)	0.0050 (4)	0.0042 (5)	-0.00107 (19)	0	0

cont.

Co:TiO_2 (V89)						
Ti1	0.0061 (3)	0.0061 (3)	0.0025 (3)	-0.00002 (8)	0	0
Co1	0.0061 (3)	0.0061 (3)	0.0025 (3)	-0.00002 (8)	0	0
O1	0.0055 (4)	0.0055 (4)	0.0027 (5)	-0.0008 (3)	0	0
Mn:TiO_2 (V104)						
Ti1	0.0052 (3)	0.0052 (3)	0.0046 (3)	0.00001 (7)	0	0
Mn1	0.0052 (3)	0.0052 (3)	0.0046 (3)	0.00001 (7)	0	0
O1	0.0048 (4)	0.0048 (4)	0.0046 (5)	-0.0012 (3)	0	0
Nb:TiO_2 (V108)						
Ti1	0.0055 (4)	0.0055 (4)	0.0029 (4)	-0.00005 (10)	0	0
Nb1	0.0055 (4)	0.0055 (4)	0.0029 (4)	-0.00005 (10)	0	0
O1	0.0052 (5)	0.0052 (5)	0.0033 (6)	-0.0009 (4)	0	0

Table 4.2.8. Selected bond lengths in Å for the grown titania (standard deviation in parentheses).

Ni:TiO_2 (V87)			
Atoms (Ti|Ni-O)	**Bond length[Å]**	**Atoms (O-Ti|Ni)**	**Bond length[Å]**
Ti1|Ni1—O1	1.9447 (6)	O1—Ti1|Ni1	1.9447 (6)
Ti1|Ni1—O1	1.9785 (9)		
Average	**1.9616 (6)**		
Fe:TiO_2 (V88)			
Atoms (Ti|Fe-O)	**Bond length[Å]**	**Atoms (O-Ti|Fe)**	**Bond length[Å]**
Ti1|Fe1—O1	1.9800 (8)	O1—Ti1|Fe1	1.9458 (5)
Ti1|Fe1—O1	1.9458 (5)		
Average	**1.9629 (6)**		
Co:TiO_2 (V89)			
Atoms (Ti|Co-O)	**Bond length[Å]**	**Atoms (O-Ti|Co)**	**Bond length[Å]**
Ti1|Co1—O1	1.9799(10)	O1—Ti1|Co1	1.9473(7)
Ti1|Co1—O1	1.9473(7)		
Average	**1.9636 (6)**		

Mn:TiO_2 (V104)			
Atoms (Ti|Mn-O)	**Bond length[Å]**	**Atoms (O-Ti|Mn)**	**Bond length[Å]**
Ti1|Mn1—O1	1.9435(5)	O1—Ti1|Mn1	1.9435(5)
Ti1|Mn1—O1	1.9780(8)		
Average	**1.9608 (6)**		
Nb:TiO_2 (V108)			
Atoms (Ti|Nb-O)	**Bond length[Å]**	**Atoms (O-Ti|Nb)**	**Bond length[Å]**
Ti1|Nb1—O1	1.9441(8)	O1—Ti1|Nb1	1.9441(8)
Ti1|Nb1—O1	1.9765(13)		
Average	**1.9603 (10)**		

The single crystal refinement of all five samples provided no evidence for the existence or formation of twins. Table 4.2.8 lists the bond lengths of the five titania single crystals. The average bonds lengths of Ni, Fe and Co doped titania are slightly larger than the average bonds length of Mn, and Nb doped titania. It would be expected for the Nb doped titania to have a larger bond length since Nb^{5+} has a larger ionic radius and show "stretch" the lattice more. However, the interatomic angles as shown in Table 4.2.9 do not vary much for the tetragonal crystals which was expected and correlates with the previous data.

Table 4.2.9. Selected interatomic angels for the grown titania (standard deviation in parentheses).

Ni:TiO_2 (V87)			
Atoms (O-Ti|Ni-O)	**Angles [°]**	**Atoms (Ti|Ni-O-Ti|Ni)**	**Angles [°]**
O1—Ti1|Ni1—O1	180	Ti1|Ni1—O1—Ti1|Ni1	98.94 (4)
O1—Ti1|Ni1—O1	81.06 (4)	Ti1|Ni1—O1—Ti1|Ni1	130.529 (19)
O1—Ti1|Ni1—O1	98.94 (4)		
O1—Ti1|Ni1—O1	90		
Fe:TiO_2 (V88)			
Atoms (O-Ti|Fe-O)	**Angles [°]**	**Atoms (Ti|Fe-O-Ti|Fe)**	**Angles [°]**
O1—Ti1|Fe1—O1	180	Ti1|Fe1—O1—Ti1|Fe1	98.78 (3)
O1—Ti1|Fe1—O1	81.22 (3)	Ti1|Fe1—O1—Ti1|Fe1	130.611 (17)
O1—Ti1|Fe1—O1	98.78 (3)		
O1—Ti1|Fe1—O1	90		

cont.

Co:TiO_2 (V89)			
Atoms (O-Ti|Co-O)	**Angles [°]**	**Atoms (Ti|Co-O-Ti|Co)**	**Angle [°]**
O1—Ti1|Co1—O1	180	Ti1|Co1—O1—Ti1|Co1	98.76 (4)
O1—Ti1|Co1—O1	81.24 (4)	Ti1|Co1—O1—Ti1|Co1	130.62 (2)
O1—Ti1|Co1—O1	98.76 (4)		
O1—Ti1|Co1—O1	90		
Mn:TiO_2 (V104)			
Atoms (O-Ti|Mn-O)	**Angles [°]**	**Atoms (Ti|Mn-O-Ti|Mn)**	**Angle [°]**
O1—Ti1|Mn1—O1	180	Ti1|Mn1—O1—Ti1|Mn1	98.87 (4)
O1—Ti1|Mn1—O1	81.13 (4)	Ti1|Mn1—O1—Ti1|Mn1	130.563 (19)
O1—Ti1|Mn1—O1	98.87 (4)		
O1—Ti1|Mn1—O1	90		
Nb:TiO_2 (V108)			
Atoms (O-Ti|Nb-O)	**Angles [°]**	**Atoms (Ti|Nb-O-Ti|Nb)**	**Angle [°]**
O1—Ti1|Nb1—O1	180	Ti1|Nb1—O1—Ti1|Nb1	98.75 (6)
O1—Ti1|Nb1—O1	81.25 (6)	Ti1|Nb1—O1—Ti1|Nb1	130.63 (3)
O1—Ti1|Nb1—O1	98.75 (6)		
O1—Ti1|Nb1—O1	90		

Table 4.2.10 shows the charge distribution of the grown titania crystals. The charge distribution was calculated with the bond-length/bond-strength model. The calculated valences of the various ions differ slightly from the theoretical values (Ti^{4+}, O^{2-}) but are still located within a region which seems logical. Most of the transitional metals exist with various valences which can influence the calculated values on the Ti spot. However, the amount doped in the TiO_2 is relative small, making the influence of any differentiating valence marginal.

Table 4.2.10. Charge distribution in M:TiO_2 (M = Ni, Fe, Co, Mn, Nb), calculated with the bond-length/bond-strength model.

	Ni:TiO_2 (V87)	
V_i	**Ti1|Ni1**	**O1**
	4.10	-2.05
	Fe:TiO_2 (V88)	
	Ti1|Fe1	**O1**
	4.09	-2.04
	Co:TiO_2 (V89)	
	Ti1|Co1	**O1**
	4.08	-2.04
	Mn:TiO_2 (V104)	
	Ti1|Mn1	**O1**
	4.11	-2.06
	Nb:TiO_2 (V108)	
	Ti1|Nb1	**O1**
	4.11	-2.06

4.2.2 Optical analysis

Diffuse optical reflectance measurements were conducted on the *M*:TiO_2 crystals *(M* = Ni, Fe, Co, Mn, Nb). The samples were grinded up prior to the experiment. The grinding was achieved with an agate mortar and pestle. The results are presented in Figure 4.2.5.

Ni:TiO_2 (V87)

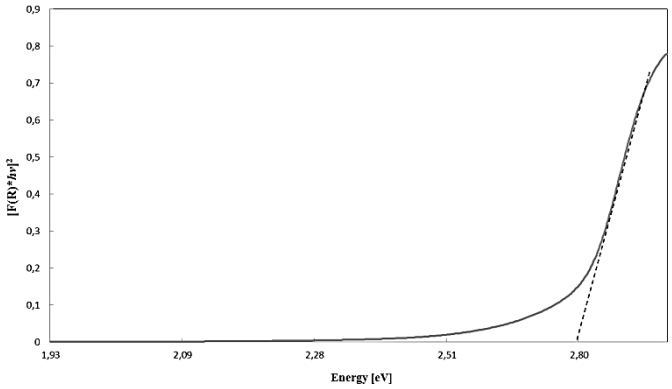

cont.

Fe:TiO_2 (V88)

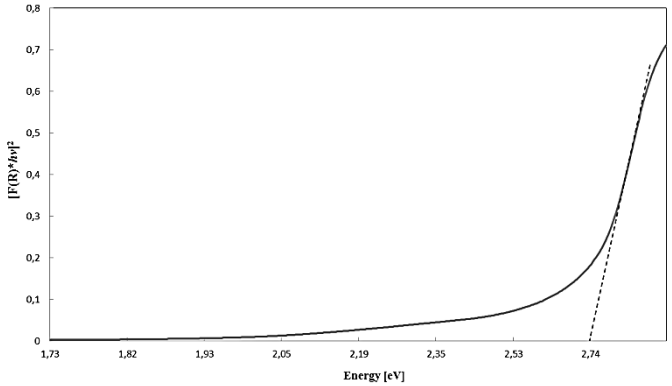

Co:TiO_2 (V89)

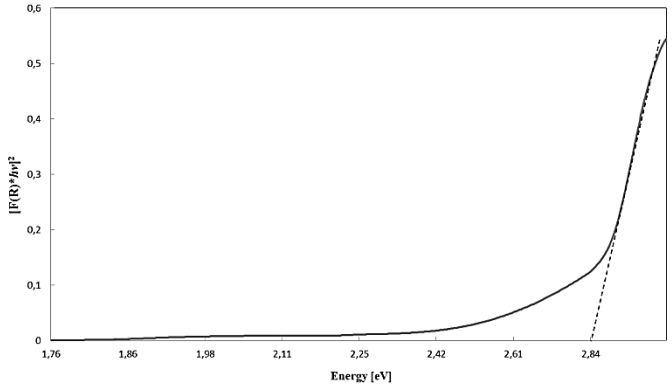

Mn:TiO_2 (V104)

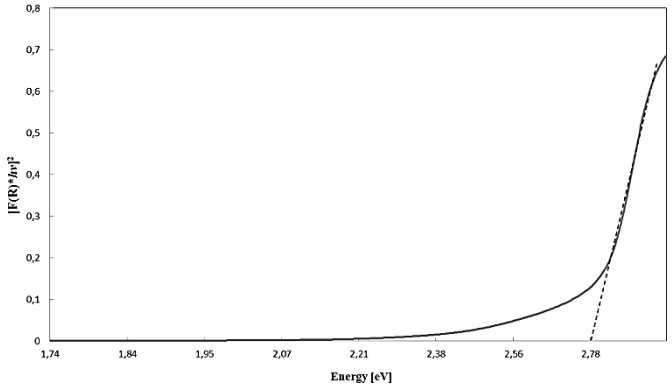

Nb:TiO_2 (V108)

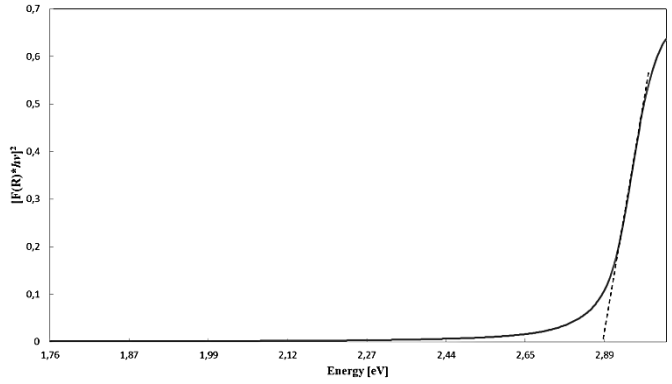

Figure 4.2.5 Kubelka-Munk transformed reflectance spectra of the grown titania single crystals.

The spectra were measured in a wavelength range of 890 nm to 220 nm. The experimental optical band-gap is determined by the use of the Kubelka-Munk function obtained from the diffuse reflectance spectrum. The extrapolation of the linear region of the Kubelka-Munk function gives the direct band-gap energy in electron Volt (eV). Figure 4.2.5 shows the Kubelka-Munk transformed reflectance spectra for each of the five titania single crystals. Based on this function, F(R)*hv* versus *hv* (energy eV) plot give the band gap energy of 2.80 eV for V87, 2.74 eV for V88, 2.84 eV for V89, 2.78 eV for V104 and 2.89 eV for V108. The values are listed in the table below (table 4.2.11).

Table 4.2.11. Optical band-gap in eV for *M*:TiO_2 (*M* = Ni, Fe, Co, Mn, Nb), derived from the Kubelka-Munk model.

Sample	**Ni:TiO_2 (V87)**	**Fe:TiO_2 (V88)**	**Co:TiO_2 (V89)**	**Mn:TiO_2 (V104)**	**Nb:TiO_2 (V108)**
Optical band-gap [eV]	2.80 ± 0.05	2.74 ± 0.05	2.84 ± 0.05	2.78 ± 0.05	2.89 ± 0.05

Since the determination of the band-gap is made "per hand" on the diagram, the error is difficult to define. Therefore, the error has been set to 0.05 to compensate for the inaccuracy of the manual determination of the band-gap. The doping of the TiO_2 based single crystals was sufficient enough to reduce the optical band-gap of the material (band-gap narrowing) by a significant portion with Fe:TiO_2 (V88) having the lowest band-gap of 2.74 eV.

4.2.3 Chemical analysis

The samples were grinded to a fine powder and homogenized by a vibrating mill from Retsch (Rethsc GmbH, Haan, Germany). The grinded powders were then pre-heated to 240 °C for 20 min under a gas mixture of HNO_3/HF/H_2O_2. Three separated weigh portions of each sample were used for the measurements. The results of the ICP-OES measurements are shown in Table 4.2.12.

Table 4.2.12. Results of the dopant measurements by ICP-OES.

Theoretical composition	Measured composition
$Ni_{0.0075}Ti_{0.9925}O_{2-\delta}$	$Ni_{0.0089}Ti_{0.9911}O_{2-\delta}$
$Fe_{0.0075}Ti_{0.9925}O_{2-\delta}$	$Fe_{0.0100}Ti_{0.9900}O_{2-\delta}$
$Co_{0.0075}Ti_{0.9925}O_{2-\delta}$	$Co_{0.0200}Ti_{0.9800}O_{2-\delta}$
$Mn_{0.0015}Ti_{0.9985}O_{2-\delta}$	$Mn_{0.00147}Ti_{0.99853}O_{2-\delta}$
$Nb_{0.0005}Ti_{0.9995}O_{2+\delta}$	$Nb_{0.0009}Ti_{0.9991}O_{2+\delta}$

The results shown in Table 4.2.12 correlate fairly with the theoretical stoichiometry. The concentration of Ni in V87 is 890 ppm or 0.089 m%. Greater deviations can be observed on V88 and V89 were the discrepancy are very high, with concentration lying at approximately 1000 ppm or 0.1 m% and 2272 ppm or ~0.23 m% for Fe and Co, respectively. This difference can be explained by slight mishandling during the mixture of the powders prior to the growth experiment. V104 and V108 correlate again very well with the theoretical values. The ICP-OES measurements result in an updated stoichiometry for the titania samples; V87 $Ni_{0.0089}Ti_{0.9911}O_{2-\delta}$, V88: $Fe_{0.0100}Ti_{0.9900}O_{2-\delta}$, V89: $Co_{0.0200}Ti_{0.9800}O_{2-\delta}$, V104: $Mn_{0.00147}Ti_{0.99853}O_{2-\delta}$ and V108: $Nb_{0.0009}Ti_{0.9991}O_{2+\delta}$.

4.2.4 Conclusion

TiO_2 has proven to have excellent photocatalytic properties with an optical band-gap of approximately 3 eV. In order to improve these properties, several transition metals (Ni, Fe, Co, Mn and Nb) were incorporated in small amounts in the host lattice with the goal to decrease the optical band-gap of the materials. The grown titania single crystals were the following: $Ni_{0.0075}Ti_{0.9925}O_{2-\delta}$, $Fe_{0.0075}Ti_{0.9925}O_{2-\delta}$, $Co_{0.0075}Ti_{0.9925}O_{2-\delta}$, $Mn_{0.0015}Ti_{0.9975}O_{2-\delta}$ and $Nb_{0.0005}Ti_{0.9995}O_{2+\delta}$. Powder and single crystal diffraction experiments reveal a tetragonal rutile structure with space group $P4_2/mnm$ (Ni:TiO_2: a = 4.596 Å, c = 2.959 Å; Fe:TiO_2: a = 4.596 Å, c = 2.960 Å; Co:TiO_2: a = 4.595 Å, c = 2.958 Å, Mn:TiO_2: a = 4.594 Å, c = 2.958 Å; Nb:TiO_2: a = 4.595 Å, c = 2.958 Å). Uv/Vis. spectroscopy measurements were conducted, using the Kubelka-Munk model, to determine the optical band-gap of the doped titania samples. The results show an optical band-gap of 2.80 eV for Ni:TiO_2, 2.70 eV for Fe:TiO_2, 2.80 eV for Co:TiO_2, 2.80 eV for Mn:TiO_2 and 2.90 eV for Nb:TiO_2.

Chemical analysis via ICP-OES showed an overall good correlation with the theoretical stoichiometry. V88 and V89 show high deviations to the theoretical values. The updated stoichiometry for the titania single crystal samples are therefore as follows: V87 $Ni_{0.0089}Ti_{0.9911}O_{2-\delta}$, V88: $Fe_{0.0100}Ti_{0.9900}O_{2-\delta}$, V89: $Co_{0.0200}Ti_{0.9800}O_{2-\delta}$, V104: $Mn_{0.00147}Ti_{0.99853}O_{2-\delta}$ and V108: $Nb_{0.0009}Ti_{0.9991}O_{2+\delta}$.

4.3 REE:YSZ (REE = Eu, Er, Tb, Yb, Tm)

Several yttrium stabilized zirconium dioxide (YSZ) single crystals were grown successfully for the first time as part of this thesis. The YSZ single crystals were (co-)doped with rare earth elements (REE) to achieve luminescent properties.

4.3.1 Single crystal growth

It was necessary to prepare the zirconia material prior to the growth experiment. Y_2O_3 (99.99%) and ZrO_2 (99.99%) were mixed homogenously in the right ratio with Eu_2O_3 (99.99%), Er_2O_3 (99.99%), Tb_2O_3 (99.99%), Yb_2O_3 (99.99%), or Tm_2O_3 (99.99%) for Eu:YSZ, (Er,Yb):YSZ, Tb:YSZ and (Tm,Yb):YSZ. The REE:YSZ (REE = Eu, Er, Tb, Yb, Tm) powders could then be filled in the Skull-crucible for the growth experiment. Hereby, no air firing was needed prior to the experiment. The exact stoichiometry is listed in Table 4.3.1. The default configuration of the Skull-melting setup is preset for the YSZ system, which allows the standard growth procedure for the experiment, with the ignition metal being put at a depth of approximately 1.5 cm. Eu:YSZ will be referred to as V93, (Er,Yb):YSZ as V95, Tb:YSZ as V97 and (Tm,Yb):YSZ as V98.

Table 4.3.1. Stoichiometry for grown REE:YSZ (REE = Eu, Er, Tb, Yb, Tm) single crystals.

V93 $Y_{0.20}Eu_{0.05}Zr_{0.75}O_{2-\delta}$		**V95** $Y_{0.200}Er_{0.015}Yb_{0.010}Zr_{0.775}O_{2-\delta}$	
Compound	**mass [g]**	**Compound**	**mass [g]**
Zirconium(IV) oxide; ZrO_2	924.2	Zirconium(IV) oxide; ZrO_2	955.0
Yttrium(III) oxide; Y_2O_3	225.8	Yttrium(III) oxide; Y_2O_3	225.8
Europium(III) oxide; Eu_2O_3	87.9	Erbium(III) oxide; Er_2O_3	28.7
/	/	Ytterbium(III) oxide; Yb_2O_3	18.6
Sum	1237.9	**Sum**	1228.1

cont.

V97 $Y_{0.20}Tb_{0.02}Zr_{0.78}O_{2-\delta}$		**V98** $Y_{0.20}Tm_{0.01}Yb_{0.01}Zr_{0.78}O_{2-\delta}$	
Compound	**mass [g]**	**Compound**	**mass [g]**
Zirconium(IV) oxide; ZrO_2	961.0	Zirconium(IV) oxide; ZrO_2	961.0
Yttrium(III) oxide; Y_2O_3	225.8	Yttrium(III) oxide; Y_2O_3	225.8
Terbium(III) oxide; Tb_2O_3	36.6	Thulium(III) oxide; Tm_2O_3	19.3
/	/	Ytterbium(III) oxide; Yb_2O_3	18.6
Sum	1237.9	**Sum**	1224.7

The growth experiment was conducted under normal air atmosphere conditions with 6.4 g zirconium serving as ignition metal (Table 4.3.2).

Table 4.3.2. Operating parameters for grown REE:YSZ (REE = Eu, Er, Tb, Yb, Tm) single crystals.

	Eu:YSZ (V93)	**(Er,Yb):YSZ (V95)**	**Tb:YSZ (V97)**	**(Tm,Yb):YSZ (V98)**
Ignition metal	Zr; 6.4 g	Zr; 6.4 g	Zr; 6.2 g	Zr; 6.6 g
Growth atmosphere	Air; 1 bar	Air; 1 bar	Air; 1 bar	Air; 1 bar
Parameters at idle position				
Voltage [%]	54	53	50	53
Current [%]	22	22.5	22	22
Power output [%]	11.5	10.5	10	10.5

The crucible was kept at the idle position for approximately 30 min to achieve a good homogenization of the melt prior to the growth.

Table 4.3.3. Growth parameters (speed and time) for the grown REE:YSZ (REE = Eu, Er, Tb, Yb, Tm) single crystals.

	Eu:YSZ (V93)	**(Er,Yb):YSZ (V95)**	**Tb:YSZ (V97)**	**(Tm,Yb):YSZ (V98)**
Speed	**Time**	**Time**	**Time**	**Time**
Idle phase	30 min	30 min	1 h	30 min
3 mm/h	1 h 30 min	1 h	1 h	1 h
6 mm/h	1 h	1 h	1 h	1 h
9 mm/h	1 h	1 h	1 h	1 h
12 mm/h	1 h	1 h	1 h	1 h
15 mm/h	15 min	45 min	30 min	/
Sum	**5 h 15 min**	**5 h 15 min**	**5 h 30 min**	**4 h 30 min**

The growth experiments had varying growth times, starting with 4.5 hours for the fastest (V98) and ending with 5.5 hour for the slowest (V97). The growth speed started from 3 mm/h and was gradually increased until 15 mm/h, with the exception of V98 where the end speed was 12 mm/h (Table 4.3.3). All grown zirconia crystals have an quadratic shape with varying dimensions and color (Figure 4.3.1). V93 has a length and width of approximately 1.5 cm (1 x 1.5 x 1.5 cm^3). The crystals sizes of V95 up to V97 are very similar with lengths and widths of approximately 2.5 cm (V95: 2.3 x 2.3 x 2.2 cm^3; V97: 2.5 x 2.5 x 2.1 cm^3). The size of V98 is slightly smaller compared to V95 and V97 but still a little larger than V93, with dimensions of 1.8 x 1.8 x 1.6 cm^{-3}. The dopants affected the colorization of the YSZ crystals (pure YSZ is colorless). Eu:YSZ (V93) is almost colorless with a slight pink touch. Whereby, (Er,Yb):YSZ (V95) has a bright pink colorization which becomes even fuller under selective artificial light. Tb:YSZ (V97) is orange to honey colored and (Tm,Yb):YSZ (V98) is, similar to Eu:YSZ (V93), almost colorless with a slight blueish colorization. However, all YSZ single crystals are transparent at all facets (Figure 4.3.1).

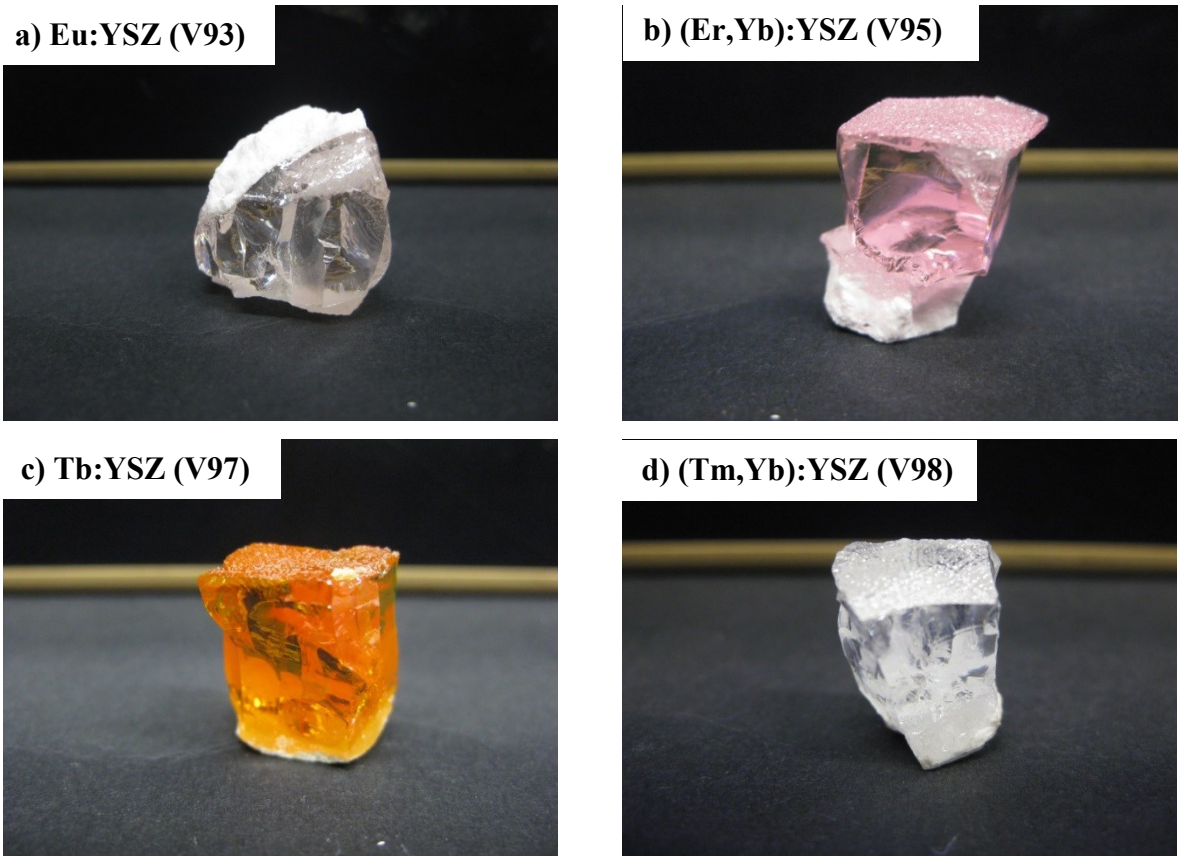

Figure 4.3.1. As-grown REE:YSZ (REE = Eu, Er, Tb, Yb, Tm) single crystals; a) Eu:YSZ (V93) b) (Er,Yb)YSZ (V95) c) Tb:YSZ (V97) and d) (Tm,Yb):YSZ (V98).

4.3.2 Structural analysis

The first structural characterization was achieved via X-ray powder diffraction analysis. Figure 4.3.2 shows the X-ray powder diffraction patterns of the grown zirconia crystals with the completed Rietveld fit. All samples have a cubic structure and were refined in space group $Fm\bar{3}m$ (No. 225) with four formula units per cell. The lattice parameters of the grown YSZ crystals are a = 5.1470 Å and for Eu:YSZ (V93), a = 5.1514 Å for (Er,Yb):YSZ (V95), a = 5.1522 Å for (Er,Yb):YSZ (V95) and a = 5.1498 Å for (Tm,Yb):YSZ (V98).

Table 4.3.4 lists the lattice parameters and selected values of the Rietveld refinement. The goodness of fits varies from 1.10 up to 2.14 which correspond to a very good fit of the structure.

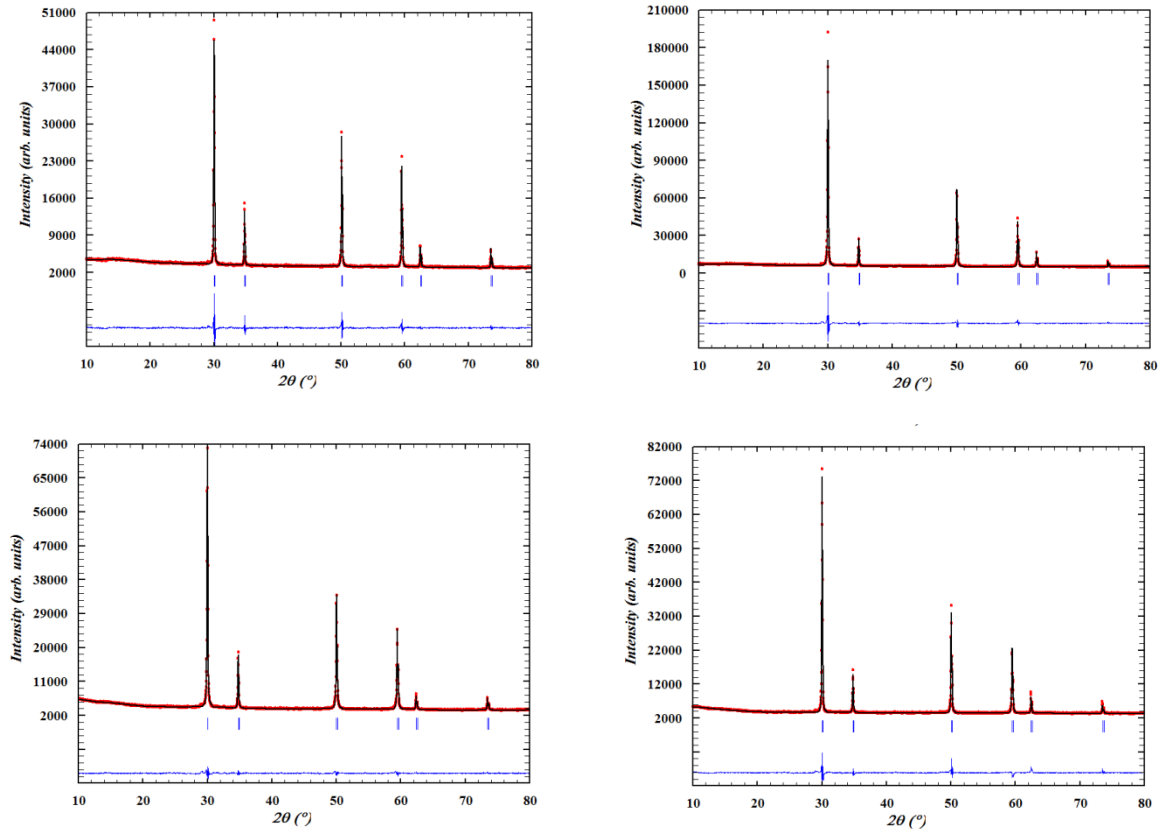

Figure 4.3.2. X-ray powder diffraction pattern for REE:YSZ (REE = Eu, Er, Tb, Yb, Tm) crystals; a) Eu:YSZ (V93) b) (Er,Yb):YSZ (V95) c) Tb:YSZ (V97) d) (Tm,Yb):YSZ (V98) with the graphical interpretation of the Rietveld refinement.

Table 4.3.4. Results of the Rietveld refinement for REE:YSZ (REE = Eu, Er, Tb, Yb, Tm) samples (standard deviations in parentheses where applicable).

	Eu:YSZ (V93)	**(Er,Yb):YSZ (V95)**	**Tb:YSZ (V97)**	**(Tm,Yb):YSZ (V98)**
Space group	$Fm\bar{3}m$	$Fm\bar{3}m$	$Fm\bar{3}m$	$Fm\bar{3}m$
Lattice parameter [Å]	a = 5.1472 (2)	a = 5.1514 (2)	a = 5.1522 (3)	a = 5.1498 (2)
R_{wp}	2.16	2.66	1.64	2.34
R_{exp}	1.65	1.24	1.50	1.57
R_{Bragg}	3.01	3.59	1.28	5.54
S	1.30	2.14	1.10	1.49

The Bragg-R factors have all approximately the same magnitude with the exception of V98 with a slightly higher Bragg-R factor of 5.54. However, the value is still within the accepted range. Laue-diffraction experiments have been conducted to determine the single crystal nature of the material.

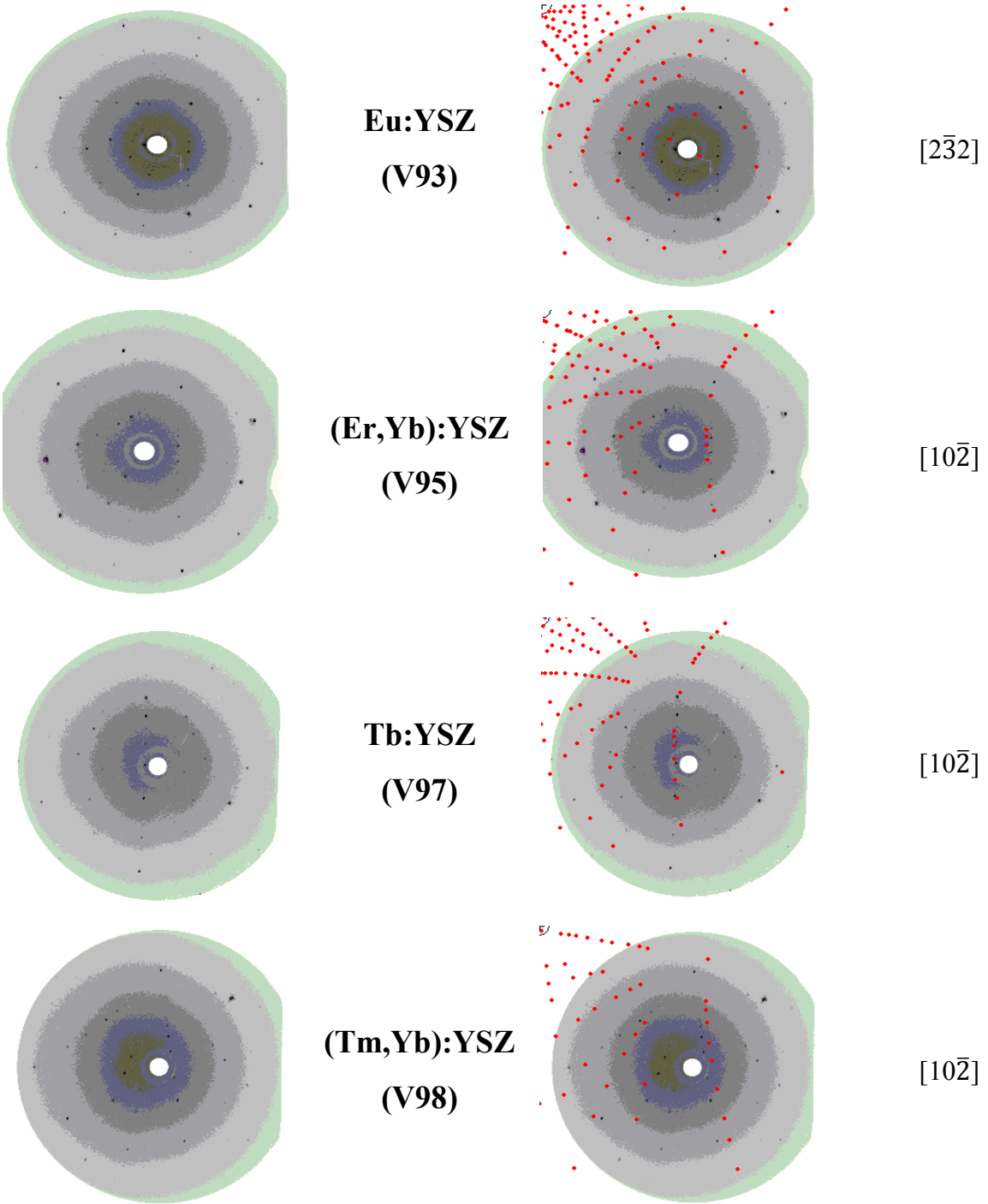

Figure 4.3.3. Laue Diffraction pattern for REE:YSZ (REE = Eu, Er, Tb, Yb, Tm) single crystals; as-measured (left) and with overlaid simulated Laue structure image.

Figure 4.3.3 shows the Laue diffraction pattern (refection) of the zirconia single crystals. All patterns show diffracted points indicating the single crystal nature of the materials. By using the software Orient express, simulated structure patterns have been generated and laid over the Laue images. The structure patterns were then adjusted by varying the *x, y* and *z* coordinates to fit the structure pattern of the Laue image. The orientation of the Laue images appear to be oriented towards $[2\bar{3}2]$ for V93, $[10\bar{2}]$ for V95, V97 and V98. The corresponding Laue group of $Fm\bar{3}m$ is $m\bar{3}m$. The patterns show no indication for any twins.

4.3.3 Optical analysis

Transmission UV/Vis. spectroscopy measurements at room temperature were conducted at the IKZ in Berlin for the four doped YSZ single crystals. The crystals were sliced to thickness of approximately 2 mm and polished on both sites. The exact thickness and diameters of the samples ate listed in Table 8.2 in the appendix.

The optical transmission was measured in a wavelength range of 200 – 2500 nm. The results of the optical transmission spectra are presented in Figure 4.3.4.

a) Eu:YSZ (V93)

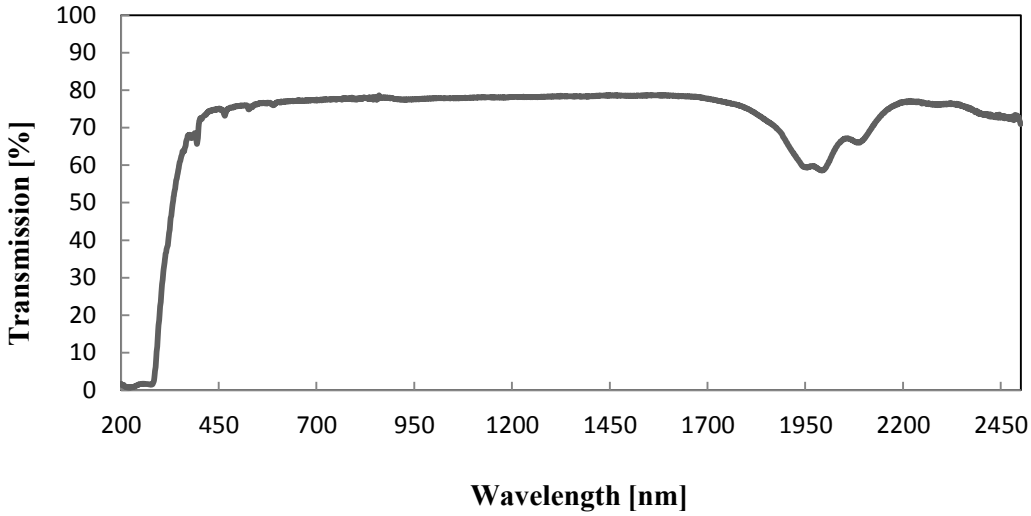

cont.

b) (Er,Yb):YSZ V95

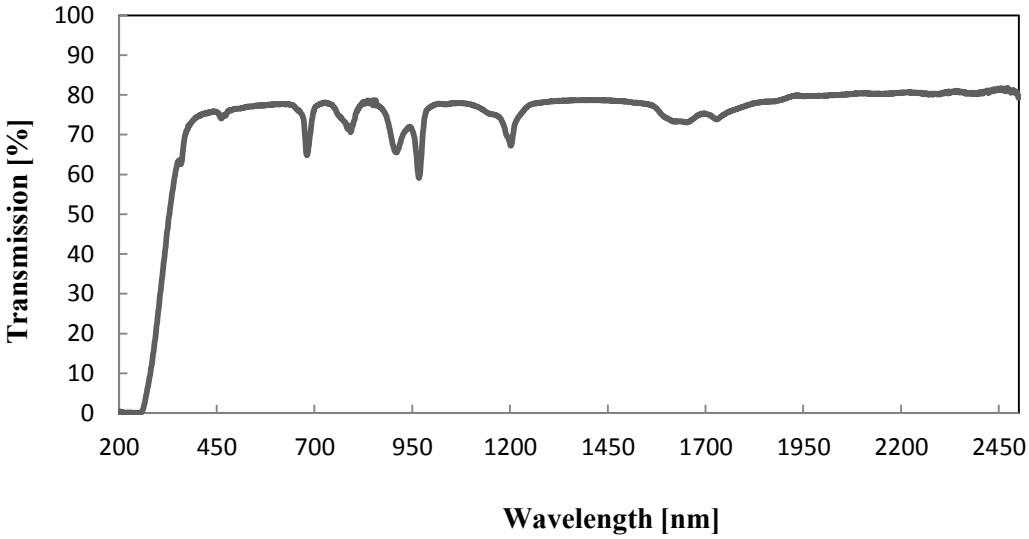

c) Tb:YSZ (V97)

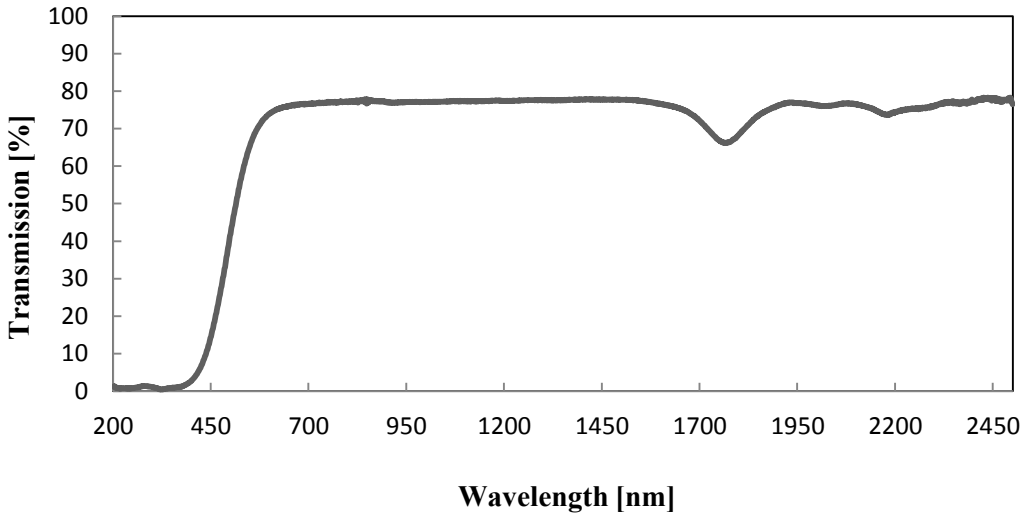

d) (Tm,Yb):YS (V98)

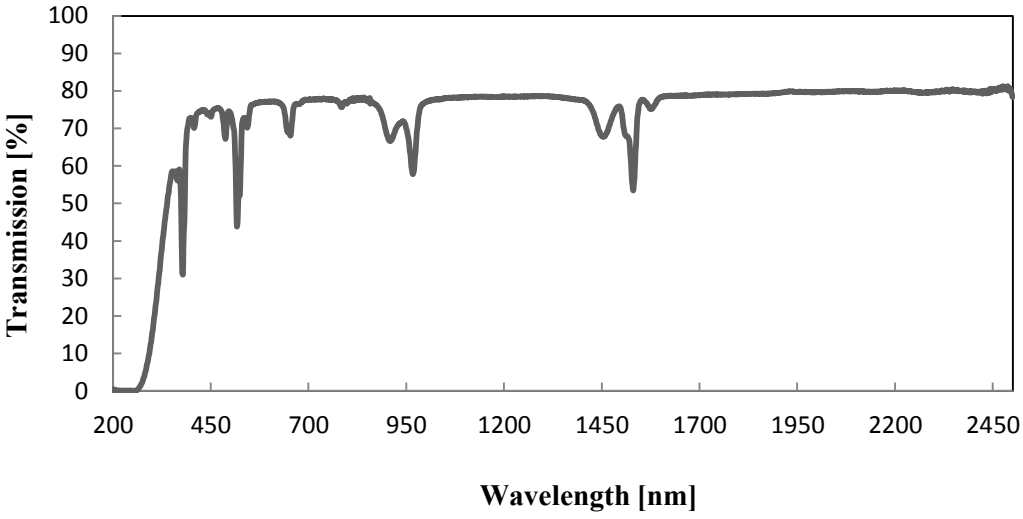

Figure 4.3.4. Transmission spectra of a) Eu:YSZ b) (Er,Yb):YSZ c) Tb:YSZ and d) (Tm,YB):YSZ single crystals.

V93 shows good absorption in the low wavelength range up to 250 nm. The fundamental absorption refers to band-to-band transitions, i.e. the excitation of an electron from the valence band to the conduction band. From there on, the transmission increases up to 80 % and then stays constant over the whole measured wavelength range. The only exception is in the 1950 nm range where the absorption-band of Eu^{3+} is visible. (Er,Yb):YSZ (V95) has, similar to Eu:YSZ (V93), a good absorption of low wavelength light up to approximately 250 nm. The transmission goes up to approximately 80 % with a number of absorption bands. The narrow absorption bands at 400 nm, 500 nm and 650 nm as well as the absorption band at 1500 nm corresponds to Er^{3+} while the absorption band at approximately 950 nm is characteristic for Yb^{3+}. The absorption in the low wavelength range in the Tb:YSZ (V97) crystal goes up to 400 nm showing a red shift in comparison to the other three samples. The transmission increases up to 80 % similar to the other crystals. A broad absorption band is visible at approximately 1800 nm and a small at 2200 nm. Both are characteristic for Tb^{3+}. The last sample (Tm,Yb):YSZ (V98) has the same absorption of low wavelength light up to 250 nm as Eu:YSZ (V93) and (Er,Yb):YSZ (V95). The transmission lies also at the 80 % range. The characteristic absorption bands of Yb^{3+} at 950 nm are here visible as well. This is similar to (Er,Yb):YSZ (V95). The remaining absorption band at 700 nm, 800 nm, 1250 nm and 1700 nm correspond to the Tm^{3+}.

The optical band-gap (E_g), expressed in eV, is calculated be following equation:

$$E_g = h\frac{c}{\lambda} \qquad (46)$$

where h is Planks constant ($h = 6.626 \cdot 10^{-34}$ Joules sec), c the speed of light ($c = 3 \cdot 10^6$ m/sec) and λ *the* cut-off wavelength. Table 4.3.5 lists the calculated optical band-gaps for the RE:YSZ (RE = Eu, Er, Tb, Yb, Tm) single crystals.

Table 4.3.5. Cut-off wavelengths and calculated optical band-gaps for REE:YSZ (REE = Eu, Er, Tb, Yb, Tm) single crystals.

Sample	**λ [nm]**	**E_g [eV]**
Eu:YSZ (V93)	256	4.85
(Er,Yb):YSZ (V95)	260	4.78
Tb:YSZ (V97)	379	3.27
(Tm,Yb):YSZ (V98)	262	4.74

The optical band-gaps of Eu:YSZ (V93), (Er,Yb):YSZ (V95) and (Tm,Yb):YSZ (V98) lie in the same magnitude since the cutoff wavelength are located at approximately the same region. The optical band-gap of Tb:YSZ (V97) is lower due to the optical red-shift in the transmission induced from the Tb^{3+} dopant. All REE:YSZ (REE = Eu, Er, Tb, Yb, Tm) single crystals feature a luminescence effect. The crystals emit under UV light excitation a characteristic colored light. Eu:YSZ (V93) which is almost colorless emits an orange light upon UV excitation with a wavelength of 585 nm up to 647 nm. (Er,Yb):YSZ (V95), which has a pink colorization emits green light upon excitation with a wavelength region of 492 to 575 nm. V97 has an orange colorization under natural light and emits partially yellow and green light, broadening the overall wavelength emission region of 492 to 585 nm. V98 has, similar to V93, almost no colorization under natural light but emits a blue light, under UV excitation, with a wavelength region of 425 to 492 nm (Figure 4.3.5).

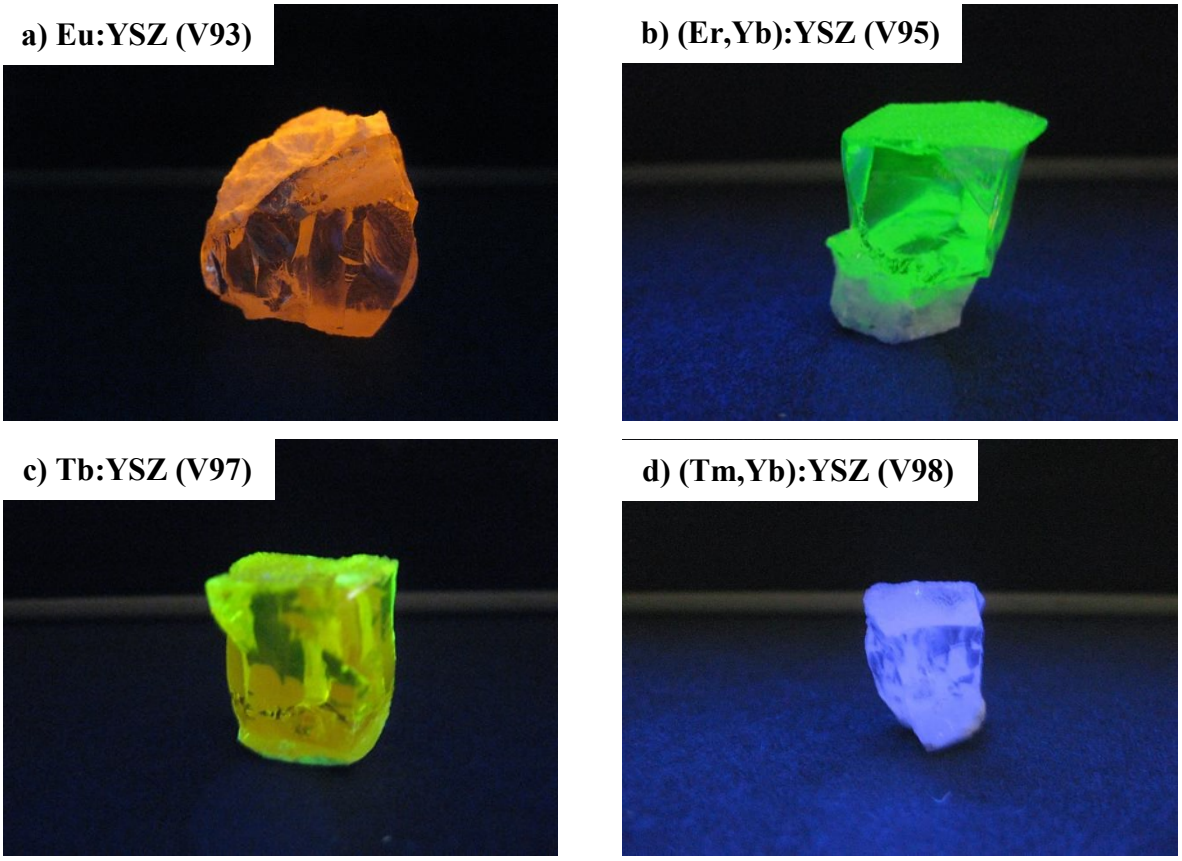

Figure 4.3.5. As-grown REE:YSZ (REE = Eu, Er, Tb, Yb, Tm) single crystals under long wave UV light (365 nm); a)Eu:YSZ (V93) b) (Er,Yb):YSZ (V95) c) Tb:YSZ (V97) and d) (Tm,Yb):YSZ (V98).

In addition, Tb:YSZ (V97) features a thermochromic effect. Hereby, the crystal changes its colorization upon heating/cooling as presented in Figure 4.3.6.

Figure 4.3.6. As-grown Tb:YSZ (V97) single crystal under ambient conditions (left) and heated up to 400°C (right). The crystal becomes much darker upon heating.

To investigate this effect, Tb:YSZ (V97) was heated up to 400°C. The crystal was taken out of the oven after 1 hour. The color changed from orange under ambient conditions to a dark red color at 400 °C. The process is reversible; after cooling down the color of the crystals was again orange. Several heating and cooling circles had the same result. Since sample V97 showed a thermochromic effect high temperature UV/Vis. measurements were conducted for Tb:YSZ (V97) as well as for Eu:YSZ (V93) and (Er,Yb):YSZ (V95) to compare the optical properties at higher temperature. The measurements were conducted with 50 K steps for each spectrum. However, for reasons of clarity and comprehensibility the graphic will only consists of spectra with 100 K step (Figures 4.3.7 to 4.3.9). The graphical interpretation of the raw data can be found in the appendix (Figures 8.2 to 8.4)

a)

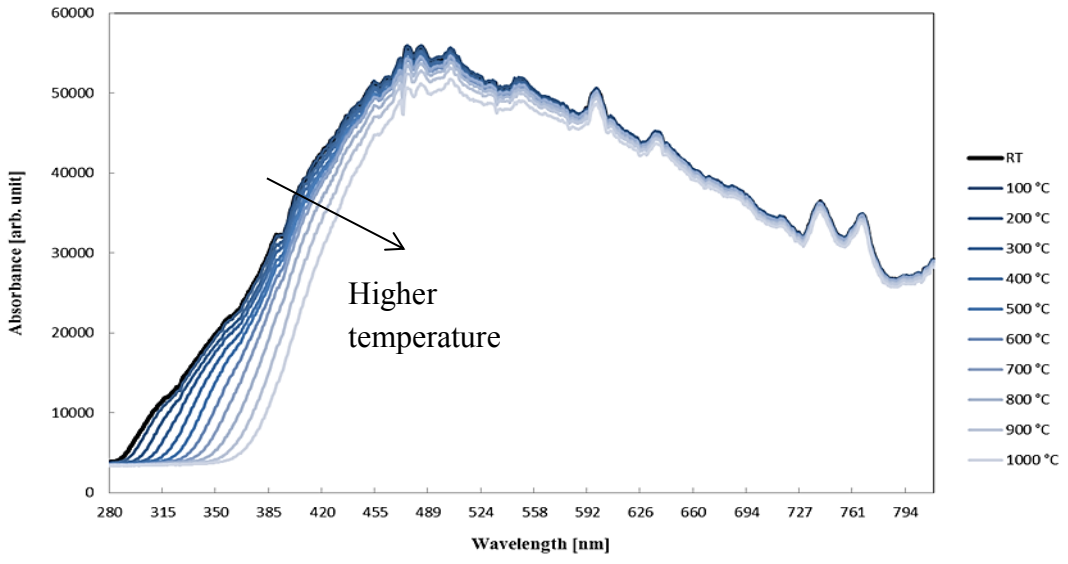

cont.

b)

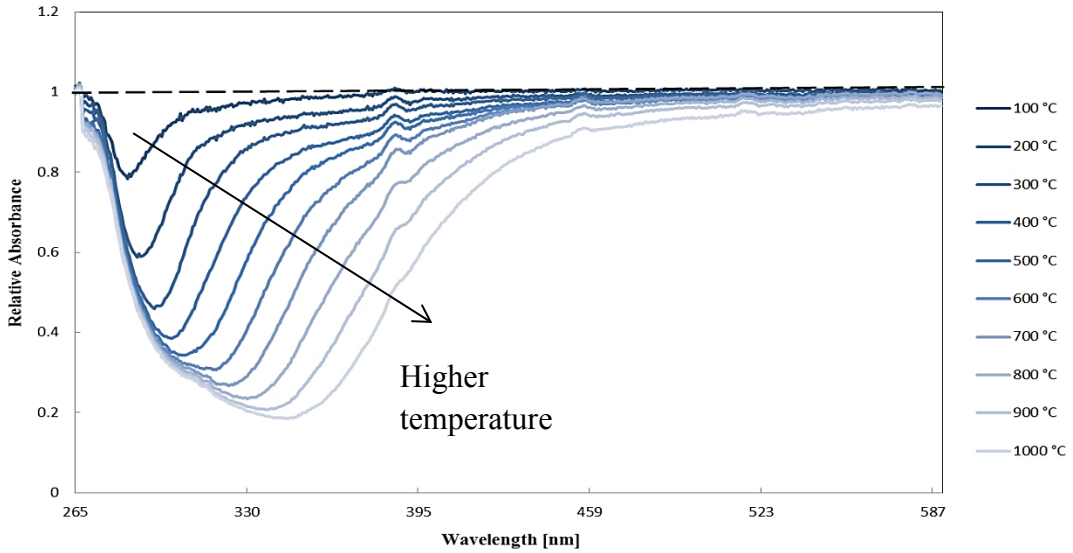

Figure 4.3.7. High temperature optical absorbance spectra for Eu:YSZ (V93) with temperature steps of 100 K; a) as measured and b) normalized to room temperature spectrum (dotted line).

Figure 4.3.7 shows the optical absorbance spectra of Eu:YSZ (V93) from room temperature to 1000 °C in range of 280 nm to 583 nm The absorbance cut-off features a red shift with increasing temperature resulting in a decreased optical band-gap in comparison to the room temperature spectrum. This can be observed even clearer in the second image (b), where the measured spectra are normalized to the room temperature spectrum. The absorbance cut-off changes from 265 nm up to 350 nm shifting almost 100 nm to the red optical spectrum. Therefore, the optical band-gap decreases from 4.85 to 3.54 eV. This effect can be explained due to the fact that the interatomic spacing increases with the amplitude of the atomic vibrations caused from the increased thermal energy (anharmonic oscillation). An increased interatomic spacing decreases the potential of the electrons in the material which subsequently reduces the optical band-gap. This effect is reversible as seen in Figure 8.5.

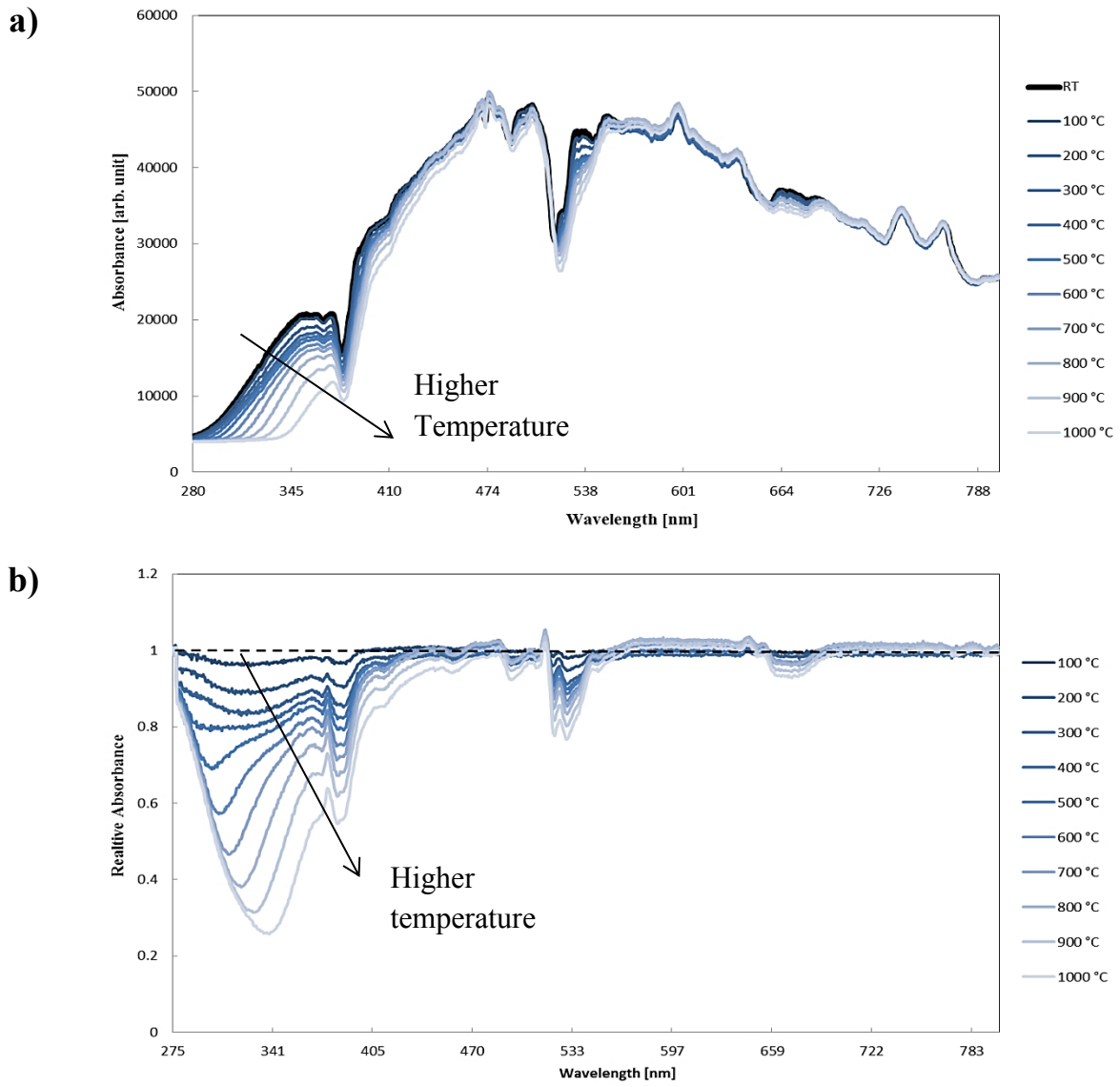

Figure 4.3.8. High temperature optical absorbance spectra for (Er,Yb):YSZ (V95) with temperature steps of 100K; a) as measured and b) normalized to room temperature spectrum (dotted line).

Figure 4.3.8 shows the optical absorbance spectra of (Er,Yb):YSZ (V95) from room temperature up to 1000 °C, starting from a wavelength of 280 nm. The absorbance cut-off features a red-shift similar to Eu:YSZ (V93). This results again in a change of the optical band-gap. The normalized spectra are showing a much better insight in the change of the band-gap (Figure 4.3.8 b). The absorbance cut-off changes from 275 nm to approximately 345 nm, which corresponds to a decrease in the band-gap from 4.78 to 3.60 eV. In addition, the normalized spectra are showing a slightly increased light absorption within the 550 nm to 640 nm wavelength region (yellow to red light) from 950 °C and above.

The same effect is occurring again in the 680 nm to 790 nm region, which corresponds to the red to IR region of light. It can be assumed that these wavelength regions are affected from Yb^{3+}. However, no reference could be found to confirm or deny this.

(a)

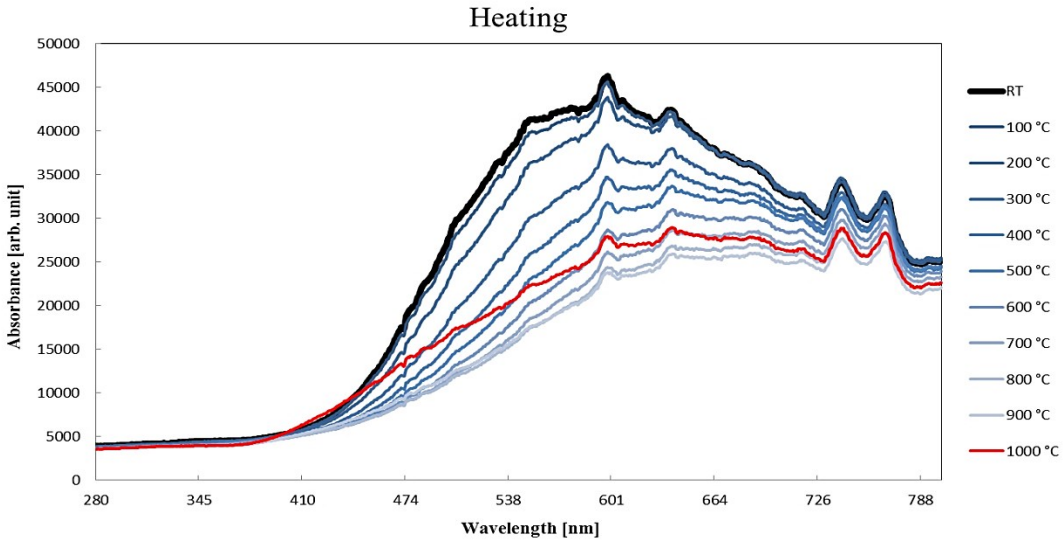

(b)

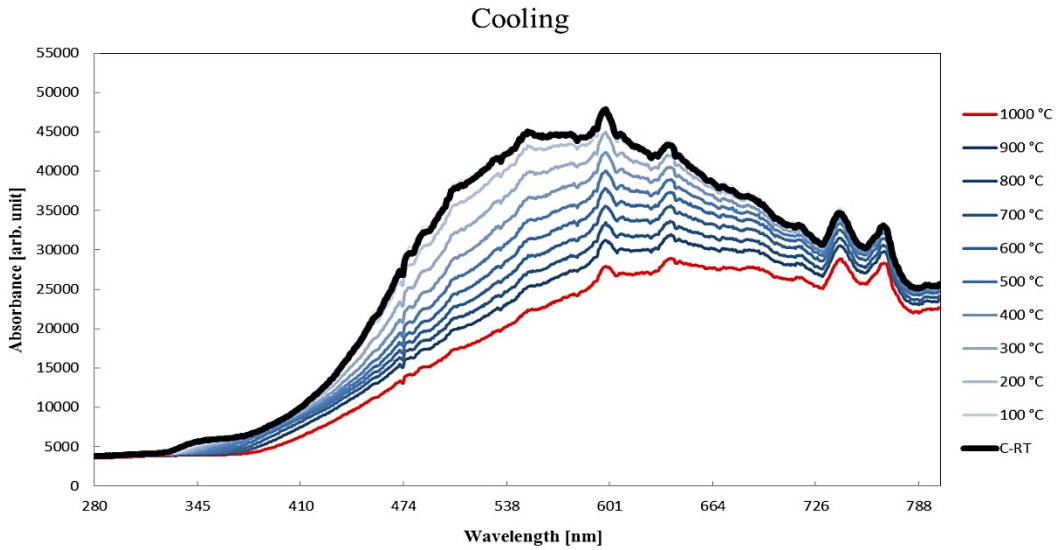

cont.

(c)

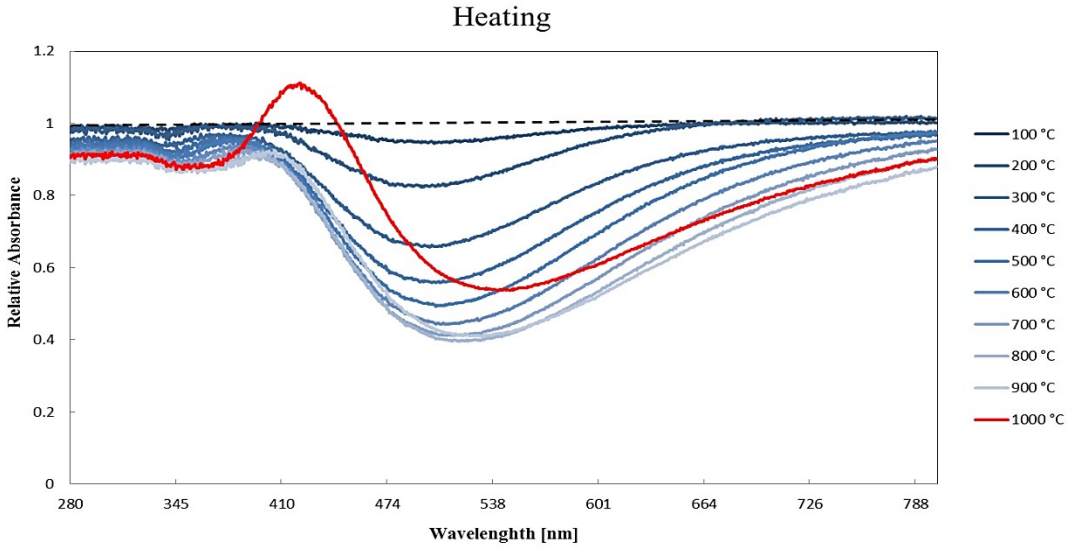

(d)

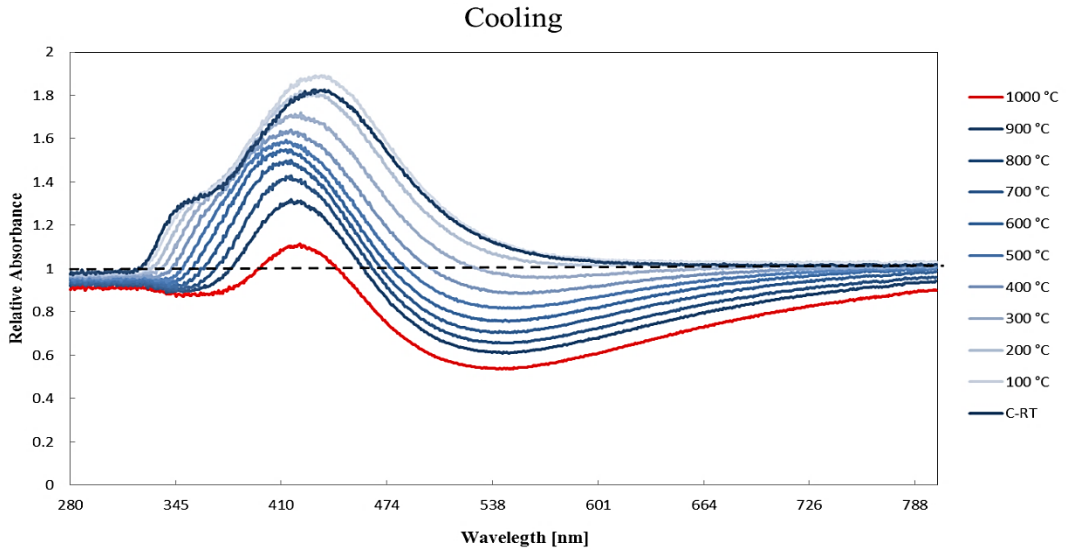

Figure 4.3.9. High temperature optical absorbance spectra for Tb:YSZ (V97) with temperature steps of 100 K; a) as measured upon heating b) as measured upon cooling c) normalized to RT spectrum upon heating d) normalized to RT spectrum upon cooling.

Figure 4.3.9 shows the optical absorbance spectra of Tb:YSZ (V97) from room temperature to 1000°C, starting from wavelength of 280 nm. The absorbance cut-off features a red-shift towards lower high wavelengths similar to Eu:YSZ (V93). This results again in a change of the optical band-gap which decreases from 3.27 to 2.89 eV.

However, the optical absorbance is not reversible; featuring a blue-shift towards lower wavelengths and subsequently higher band-gaps. The absorbance already increases during the heating process at the 1000 °C mark and continues to increase further during the cooling process resulting in an overall higher absorbance and blue-shifted spectra. This is seen even better in the normalized spectra. The transparency is decreasing as expected until the 1000 °C mark where the transparency at the 435 nm region is suddenly jumping above the normalized level. The absorbance further increases during the cooling process while the spectra continue to shift towards the higher wavelengths. This results in an approximately 80 % higher light absorbance compared to the pre-heated sample. The transmission band also shifts slightly to the red from 440 nm to 450 nm. This effect only occurred in sample Tb:YSZ (V97). The optical band-gap also changed to a higher value of 3.76 eV at room temperature after the heat circle (Figure 8.5). The Tb^{3+} dopant appears to influence this effect. However, by the time of this thesis, no explanation for this occurring effect could be given.

4.3.4. Conclusion

Rare earth element (REE) doped materials are suitable for various optical applications like tunable laser, planar guides and smart windows. YSZ promises to be an excellent host material, due to its high mechanical and chemical stability as well as good optical properties. Therefore, several REE (co-)doped YSZ single crystals were successfully grown for the first time as part of this work as well; $Y_{0.2}Eu_{0.05}Zr_{0.75}O_{2-\delta}$, $Y_{0.2}Er_{0.015}Yb_{0.01}Zr_{0.775}O_{2-\delta}$, $Y_{0.2}Tb_{0.02}Zr_{0.78}O_{2-\delta}$ and $Y_{0.2}Tm_{0.01}Yb_{0.01}Zr_{0.78}O_{2-\delta}$. Powder X-ray diffraction experiments revealed a cubic structure belonging to the space group $Fm\bar{3}m$ (Eu:YSZ (V93): a = 5.147 Å; (Er,Yb):YSZ (V95): a = 5.151 Å; Tb:YSZ (V97): a = 5.152 Å; (Tm,Yb):YSZ (V98): a = 5.149 Å). The single crystalline nature of the materials was confirmed with Laue diffraction measurements. The single crystals feature fluorescence properties due to their RE doping. Therefore, UV/Vis. spectroscopy measurements were conducted on the sliced and polished crystals. Room temperature transmission spectroscopy experiments revealed an increase in transmission up to 80 % for all samples from approximately 250 nm. The only exception being the Tb doped YSZ crystal with a red shift of approximately 150 nm compared to the other three crystals. The characteristic absorption bands for the rare earth elements are: Eu^{3+}: 1950 nm; Yb^{3+}: 950 nm; Er^{3+}: 400, 500, 650 and 1500 nm; Tb^{3+}: 1800 and 2200 nm; Tm^{3+}: 700, 800, 1250 1700 nm.

The calculated optical band-gaps are: 4.85 eV for Eu:YSZ; 4.78 eV for (Er,Yb):YSZ; 3.27 eV for Tb:YSZ and 4.74 eV for (Tm,Yb):YSZ. Additionally, high temperature absorption spectroscopy measurements were conducted with the Eu:YSZ, (Er,Yb):YSZ and Tb:YSZ single crystals (with 50 K steps for each spectrum). The absorption cut-offs feature a shift towards higher wavelengths with increasing temperature which results in a lower optical band-gap. The spectra have also been normalized to the room temperature spectrum in order to compare the relative variation in absorbance of the samples. For Eu:YSZ (V93) and (Er,Yb):YSZ (V95) the overall absorbance decreases with increasing temperature while the optical band-gap is decreasing simultaneously as well. In addition, the spectrum of Tb:YSZ (V97) is showing a similar behavior until the 950 °C mark. Then, the absorbance is increasing at the 1000 °C point and continues increasing during cooling, resulting in a 80 % higher absorbance compared to the initial room temperature spectrum. Unfortunately, no literature could be found to explain this effect of the TB:YSZ (V97) single crystal.

5. SUMMARY

The alkaline earth zirconate single crystals, namely $CaZrO_3$, $SrZrO_3$ and $BaZrO_3$ are the first grown single crystals of their kind and were therefore are structurally described for the first time as single crystals in this thesis. They were used for optical measurements at the University Siegen and also as substrates for multiferroic materials at the Leibniz Institute of crystal growth in Berlin. $SrZrO_3$ single crystals were grown twice, one time under normal air atmosphere and one time under nitrogen atmosphere of 1350 mbar. All the zirconates belong to the perovskite structure type. The powder and single crystal diffraction experiments revealed that $CaZrO_3$ and $SrZrO_3$ have an orthorhombic structure with space group *Pcmn* (a = 5.7617 (1) Å, b = 8.0170 (2) Å and c = 5.5902 (1) Å) and *Pbnm* (a = 5.7911 (3) Å, b = 5.8241 (3) Å and c = 8.2045 (4) Å), respectively, while $BaZrO_3$ exhibits the cubic $Pm\bar{3}m$ space group (a = 4.1951 (8) Å). According to the classification proposed by Glazer, $CaZrO_3$ and $SrZrO_3$ belong to the $a^- b^+ a^-$, $BaZrO_3$ to the $a^0 a^0 a^0$ category. Both the orthorhombic $CaZrO_3$ and $SrZrO_3$ feature twins. $CaZrO_3$ is twinned as contact twin by a rotation of approximately 90° around [010] mono-periodically. $SrZrO_3$ is twinned as penetration twin by a 180° rotation around [101] tri-periodically. The twinning is induced by the transformation of the high symmetry cubic phase at higher temperatures to the lower symmetric tetragonal and finally orthorhombic phase. The transformation path described by the group-subgroup relations is as follows: $Pm\bar{3}m \rightarrow P4/mmm \rightarrow Cmm \rightarrow Cmcm \rightarrow Pnma$ ($P\ 4/m\ \bar{3}\ 2/m \rightarrow P\ 4/m\ 2/m\ 2/m \rightarrow C\ 2/m\ 2/m\ 2/m \rightarrow C\ 2/m\ 2/c\ 2_1/m \rightarrow P\ 2_1/n\ 2_1/m\ 2_1/a$). The single oxygen position has a Wyckoff splitting into two positions from cubic to orthorhombic. The optical reflectance spectroscopy measurements reveal complex spectra for all zirconate single crystals. Especially the $SrZrO_3$ samples are showing luminescence effects at wavelengths of 260 to 280 nm. A strong difference of 160 nm is noted on the emission wavelength of the $SrZrO_3$ grown under air and the one grown under nitrogen atmosphere. This difference was suggested to be caused from small nitrogen incorporation in the $SrZrO_3$ which couldn't be detected with the methods at hand. $CaZrO_3$ was used as a substrate for multiferroic materials, since it was the only crystal with suitable dimensions and lattice parameters. Therefore, $K_{0.8}Na_{0.2}NbO_3$ was successfully grown as layer on the $CaZrO_3$ substrate. However, the twins present in the $CaZrO_3$ crystals lead to a poor quality of the grown layer with rough surface and cluster formation. TiO_2 has proven to have excellent photocatalytic properties with an optical band-gap of approximately 3 eV.

In order to improve these properties, several transition metals (Ni, Fe, Co, Mn and Nb) were incorporated in the host lattice with the goal to decrease the optical band-gap of the materials. The grown titania single crystals were the following: $Ni_{0.0075}Ti_{0.9925}O_{2-\delta}$, $Fe_{0.0075}Ti_{0.9925}O_{2-\delta}$, $Co_{0.0075}Ti_{0.9925}O_{2-\delta}$, $Mn_{0.0015}Ti_{0.9975}O_{2-\delta}$, and $Nb_{0.0005}Ti_{0.9995}O_{2+\delta}$. Powder and single crystal diffraction experiments reveal a tetragonal rutile structure with the space group $P4_2/mnm$ (Ni:TiO_2: a = 4.5957 (1) Å, c = 2.9594 (7) Å; Fe:TiO_2: a = 4.5955 (1) Å, c = 2.9598 (7) Å; Co:TiO_2: a = 4.5952 (1) Å, c = 2.95950 (7) Å, Mn:TiO_2: a = 4.5937 (1) Å, c = 2.9575 (8) Å; Nb:TiO_2: a = 4.5948 (1) Å, c = 2.9581 (8) Å). Uv/Vis. spectroscopy measurements were conducted, using the Kubelka-Munk model, to determine the optical band-gap of the doped titania samples. The results show an optical band-gap of 2.80 eV for Ni:TiO_2, 2.70 eV for Fe:TiO_2, 2.80 eV for Co:TiO_2, 2.80 eV for Mn:TiO_2 and 2.90 eV for Nb:TiO_2. The chemical analysis via ICP-OES showed an overall good correlation with the theoretical stoichiometry: $Ni_{0.0089}Ti_{0.9911}O_{2-\delta}$, $Fe_{0.0100}Ti_{0.9900}O_{2-\delta}$, $Co_{0.0200}Ti_{0.9800}O_{2-\delta}$, $Mn_{0.00147}Ti_{0.99853}O_{2-\delta}$, and $Nb_{0.0009}Ti_{0.9991}O_{2+\delta}$.

Rare earth element (REE) doped materials are suitable for various optical applications like tunable lasers, planar guides and smart windows. Yttrium stabilized zirconium dioxide (YSZ) promises to be an excellent host material due to its high mechanical and chemical stability as well as good optical properties. Therefore, four REE (co-)doped YSZ single crystals were successfully grown for the first time as part of this work: $Y_{0.20}Eu_{0.05}Zr_{0.75}O_{2-\delta}$, $Y_{0.200}Er_{0.015}Yb_{0.01}Zr_{0.775}O_{2-\delta}$, $Y_{0.20}Tb_{0.02}Zr_{0.78}O_{2-\delta}$ and $Y_{0.20}Tm_{0.01}Yb_{0.01}Zr_{0.78}O_{2-\delta}$. Powder X-ray diffraction experiments revealed a cubic structure belonging to space group $Fm\bar{3}m$ (Eu:YSZ: a = 5.1472 (2) Å; (Er,Yb):YSZ: a = 5.1514 (2) Å; Tb:YSZ: a = 5.1520 (3) Å; (Tm,Yb):YSZ: a = 5.1498 (2) Å). The single crystalline nature of the materials was confirmed with Laue diffraction measurements. The single crystals feature fluorescence properties due to their RE doping. Therefore, UV/Vis. spectroscopy measurements were conducted on the sliced and polished crystals. Room temperature transmission spectroscopy experiments revealed an increase in transmission up to 80 % for all samples at approximately 250 nm. The only exception is the Tb doped YSZ crystal with a red shift of approximately 150 nm compared to the other three crystals. The measurements gave the characteristic absorption bands for the rare earth elements (Eu^{3+}: 1950 cm^{-1}; Yb^{3+}: 950 cm^{-1}; Er^{3+}: 400, 500, 650 and 1500 cm^{-1}; Tb^{3+}: 1800 and 2200 cm^{-1}; Tm^{3+}: 700, 800, 1250 1700 cm^{-1}). The calculated optical band-gap are: 4.85 eV for Eu:YSZ; 4.78 eV for (Er,Yb):YSZ; 3.27 eV for Tb:YSZ and 4.74 eV for (Tm,Yb):YSZ.

Additionally, high temperature absorption spectroscopy measurements were conducted with the Eu:YSZ, (Er,Yb):YSZ, and Tb:YSZ single crystals (with 50 K steps for each spectrum). The absorption cut-offs feature a red-shift with increasing temperature which results in a lower optical band-gap. The spectra have also been normalized to the room temperature spectrum to observe the relative variation in absorbance of the samples. For Eu:YSZ and (Er,Yb):YSZ the overall absorbance decreases with increasing temperature while the optical band-gap is decreasing simultaneously as well. In addition, the spectrum of Tb:YSZ is showing a similar behavior up to the 950 °C mark. Then, the absorbance is increasing at the 1000 °C point and continues increasing during cooling, resulting in a 80 % higher absorbance compared to the initial room temperature spectrum. The reason for this behavior is still unknown.

6. OUTLOOK

The Skull melting technique was shown to be useful for the growth of the high melting materials presented in this thesis. However, the technique and setup still leave room for improvement and optimization. Although the used ignition materials normally consisted of the metal of the corresponding oxide, an alternative heating method without the use of any metal at all would be preferable. The use of the ignition metals adds a "timer" to the whole growth experiment since the metal itself oxidizes very fast. If the HF-field is not induced to the heated material by the time the metal oxidized the experiment has failed and must be started over. By adding an external heat source, e.g. an oxyhydrogen torch or a high energy laser, the system could be controlled better. An optimization of the growth chamber to withstand higher gas pressures could be another way to improve the single crystal growth. Many materials tend to sublimate partially during the melting process increasing the pressure inside the Skull favoring the breaking of the outer ceramic crust. In the worst case, the sublimation is so strong that it can alter the stoichiometry of the system disrupting a successful crystal growth. A higher gas pressure can prevent or at least reduce the sublimation process of the material. Of the three grown zirconate single crystals only $CaZrO_3$ was huge enough to be processed further to substrates. However, the twins generated from the transformations reduced drastically the overall crystal quality making it unpreferable for the use as substrates for the epitactic growth of mutilferoic materials. By stabilizing the cubic phase of the zirconates ($CaZrO_3$ and $SrZrO_3$) by doping, the formation of twins can be prevented, hereby, increasing the overall crystal quality. Since both orthorhombic zirconates have a Goldschmidt tolerance factor relatively near to 1 (pseudo-cubic), a small substitution of barium may be enough to stabilize $CaZrO_3$ and $SrZrO_3$ in its cubic phase. Furthermore, the size of the grown crystals may also be increased.

Doping of TiO_2 single crystals with transition metals already influenced the optical band gap of the material. The optical band-gap can be altered further by optimizing the dopant concentration and by usage of co-dopants (i.e. band-gap engineering).

The REE doping of the YSZ single crystals can be altered as well by optimizing the dopant concentration to improve quantum yield. Further co-doping, especially with ytterbium, may also improve the overall fluorescent properties of europium and terbium doped YSZ. The increase in absorbance after heating for the Tb:YSZ single crystals should be analyzed further to explain this effect.

7. BIBLIOGRAPHY

[1] Adraina Zaleska; *Rec. Pat. on Eng.* 2**,** 157 – 164; **2008**

[2] J. Li, A.M. Gilbertson, K.L. Litvinenko, L.F. Cohen, S.K. Clowes; *Phys. Rev.* B 85 045431; **2012**

[3] O. Savchyn, K.R. Coffey, P.G. Kik; *Appl. Phys. Lett*. 97 201107; **2010**.

[4] V.S. Marques, L.S. Cavalcante, J.C. Sczancoski, E.C. Paris, J.M.C. Teixeira, J.A. Varelac, F.S. De Vicente, M.R. Joya, P.S. Pizani, M. Siu Li, M.R.M.C. Santos, E. Longo; *Spectrochim. Acta A* 74 1050; **2009**

[5] T.M. Mazzo,M.L. Moreira, I.M. Pinatti, F.C. Picon, E.R. Leite, I.L.V. Rosa, J.A. Varela, L.A. Perazolli, E. Longo; *Opt. Mater.* 32 990; **2010**

[6] R. Jia, W. Yang, Y. Bai, T. Li, *Opt. Mater*. 28 246; **2006**

[7] W. Hönle, G. Miller and A. Simon; *J. Sol. Stat. Chem*. 75, 147-155; **1988**.

[8] A. Clearfield; *Acta Cryst*. 16, 134-142; **1963**.

[9] F. Gingl T. Vogt, E. Akiba and K. Yvon; *J. Al. and Comp.* 282, 125; **1999**

[10] S. Peschel, B. Ziegler, M. Schwarten and D. Babe;, *Z. Anorg. Allg. Chem*. 626; 1561-1566; **2000**.

[11] S. Carlson, A. K. Larsson and F. E. Rohrer; *Acta Cryst*. B56; 189-196; **2000**.

[12] R. Marchand, Y. Laurent, J. Guyader, P. L'Haridon and P. Verdier; *J. Eur. Ceram. Soc.* 8; 197-213; **1991**.

[13] R. J. Hemley, M. D. Jackson and R. G. Gordon; *Phys. Chem. Minerals* 14, 2-12; **1987**.

[14] Y. Nishihata, Y. Mizuki, T. Akao, H. Tanaka, M. Uenishi, M. Kimura, T. Okamoto and N. Hamada; *Nature* 418, 164-167; **2002**.

[15] H. Hughes, D. M. Iddles and I. M. Reaney; *Appl. Phys. Letters* 79; 2952-2954; **2001**.

[16] P. K. Davies, J. Tong and J. Negas; *J Am. Ceram. Soc*. 80(7); 1727-1740; **1997**.

[17] B. Soubeyroux, J. L. Tholence and R. Tournier; *Europhysic. Let.* 3, 1301- 1307; **1987**.

[18] G. Shirane, H. Danner and R. Pepinski; *Phys. Rev.* 105, 3, 856-860; **1957**.

[19] R. E. Newnham and G. R. Ruschau; *J. Am. Ceram. Soc*. 74, 463-480; **1991**.

[20] S. Trolier-McKinstry and R. E. Newnham; *MRS Bulletin April*, 27-33; **1993**.

[21] R. E. Newnham; *MRS Bulletin May*, 20-34. **1997**.

[22] A. W. Sleight, J. L. Gillson P. E. Bierstedt; *Solid St. Comm*. 17, 27-28. **1975**.

[23] R. J. Cava, R. B. van Dover, B. Batlogg and E. A. Rietman, E.A.; *Phys. Rev. Lett.* 58(4), 408 410; **1987**.

[24] G. Q. Gong, C. Canedy, G. Xiao, J. Sun, A. Gupta and W. J. Gallagher; *Appl. Phys. Lett*. 67, 1783-1719; **1995**.

[25] M. W. Lufaso, *Dissertation*, Ohio State University, Columbus, OH, **2002**.

[26] K. E. Stitzer, M. D. Smith and H. C. zur Loye; *Sol. Stat. Sc.* 4, 311-316; **2002**.

[27] T. Sakai, G. Adachi, J. Shiokawa and Shinike, T.; *Mat. Res. Bull*. 11; 1295-1300; **1976**.

[28] I. D. Brown; *Acta Cryst*. B48, 553-572; **1992**.

[29] A. M. Glazer, H. D. Megaw; *Act. Cryst*, Section A29, pp. 489-495; **1973**

[30] J. Kanamori; *J. Appl. Phys*. 31(5), 14S-23S; **1960**.

[31] P. M. Woodward; *Acta Cryst*. B53, 32-43; **1997a**.

[32] A. M. Glazer; *Acta Cryst*., B28**,** 3384-3392.; **1972**.

[33] K. S. Aleksandrov; *Kristallografiya* 21, 249-255; **1976**.

[34] C. J. Howard and H. T. Stokes; *Acta Cryst*. B54, 782-789; **1998**.

[35] K. S. Aleksandrov J. Bartolome; *Phase Trans*. 74(3), 255-335; **2001**.

[36] K. S. Aleksandrov B. V. Beznosikov; *Ferroelectrics* 226, 1-9; **1999**.

[37] O. Bock and U. Müller; *Acta Cryst*. B58, 594-606; **2002**.

[38] P. M. Woodward; *Acta Cryst*. B53, 44-66; **1997b**.

[39] Y. Zhao, D. Weidner, J. B. Parise, D. Cox; *Phys. Earth and Plan. Int*. 76, 17-34; **1993**.

[40] H. Y. Hwang, T. T. M. Palstra, S. W. Cheong and B. Batlogg; *Phys. Rev. B.* 52(21), 15046-15049; **1995**.

[41] J. Töpfer and J. B. Goodenough; *J. Solid State Chem*. 130, 117-128; **1997.**

[42] E. L. Colla,I. M. Reaney and N. Setter; *J. Appl. Phys*. 74, 3414-3425; **1993**.

[43] V. M. Goldschmidt; *Naturwissenschaften* 14, 477-485; **1926**.

[44] R. D. Shannon; *Acta Cryst*. A32, 751-767; **1976**.

[45] X. Chen and S. S. Mao; *Chem. Rev.* 107, 2891-2959; **2007**.

[46] A. H. Fujishima, K.; *Nature*, 238, pp. 37-38; **1972**.

[47] C. A. M. Grimes, G. K.; "*TiO_2 Nanotube Arrays: Synthesis, Properties and Applications"*, Springer Science LLC, NY, USA, **2009**.

[48] A. Ghicov and P. Schmuki; *Chem. Comm.*, 2791-2808; **2009**.

[49] P. Roy, S. Berger and P. Schmuki; *Ang. Chem.-Intern. Ed.,* 50, 2904-2939; **2011**.

[50] K. Zhu, N. R. Neale, A. F. Halverson, J. Y. Kim and A. J. Frank, *J. of Phys. Chem. C*, 114, 13433-13441, **2010.**

[51] K. Shankar, J. I. Basham, N. K. Allam, O. K. Varghese, G. K. Mor, X. Feng, M. Paulose, J. A. Seabold, K.-S. Choi and C. A. Grimes; *J. of Phys. Chem. C,* 113, 6327 6359; **2009**.

[52] Y. Y. Song, F. Schmidt-Stein, S. Berger and P. Schmuki; Small, 6, 1180-1184; **2010.**

[53] S. Gupta and M. Tripathi*; Chin. Sc. Bull.*, 56, 1639-1657; **2011**.

[54] F. P. Y. Dachille, Simons; R. Roy; *Am. Min.,* 53, pp. 1929- 1939; **1968**.

[55] K. M. Reddy, S. V. Manorama and A. R. Reddy; *Mat. Chem. and Phys.*, 78, 239-245; **2003.**

[56] R. A. H. J.F.W. Bowles, D. J. Vaughan, J. Zussman; *"Non-Silicates: Oxides, Hydroxides and Sulphides";* Geol. Soc. of London*,* UK, Volume 1, 145, 299-301; **2011**.

[57] O. Carp, C. L. Huisman and A. Reller*; Prog. in Sol. St. Chem.*, 32, pp. 33-177, **2004**.

[58] J. F. Porter, Y. G. Li and C. K. Chan; *J. of Mat. Sc.*, 34, 1523-1531; **1999**.

[59] H. Z. Zhang, B. Chen, J. F. Banfield and G. A. Waychunas; *Phys.Rev. B* 78, 214106 **2008**

[60] Q. H. Zhang, L. Gao and J. K. Guo; *Appl. Cat. B-Env.*, 26, 207-215; **2000**.

[61] D. Reyes-Coronado, G. Rodriguez-Gattorno, M. E. Espinosa-Pesqueira, C. Cab, R. de Coss and G. Oskam; *Nanotechnology,* 19; 145605, **2008**.

[62] Pegah Mohammad Hosseinpour, Dissertation, Northeastern University, Boston, MA; **2014**

[63] S. D. Mo and W. Y. Ching; *Phys. Rev. B*, 51, 13023-13032; **1995**.

[64] E. G. S. M. C. Kratzer; *„Charged Semiconductor Defects: Structure, Thermodynamics and Diffusion"*; Springer-Verlag Ltd., London, UK, 67; **2009**.

[65] T. Thompson and J. Yates, Jr; *Top. in Cat.*, 35, 197-210; **2005**.

[66] J. Stausholm-Møller, H. H. Kristoffersen, B. Hinnemann, G. K. H. Madsen and B. Hammer; *J. of Chem. Phys.*, 133; **2010**.

[67] X. Y. Pan, M. Q. Yang, X. Z. Fu, N. Zhang and Y. J. Xu; *Nanoscale*, 5, 3601-3614; **2013**.

[68] M. Ni, M. K. H. Leung, D. Y. C. Leung and K. Sumathy; *Renew. and Sustain. En. Rev.*, 11, 401-425; **2007**.

[69] G. R. Dey and K. K. Pushpa; *Res. on Chem. Interm.*, 33, 631-644; **2007**.

[70] Y. B. Xie and C. W. Yuan; *J. of En. Sc.*, 14, 70-75; **2002**.

[71] M. R. Hoffmann, S. T. Martin, W. Choi and D. W. Bahnemann; *Chem. Rev.*, 95, 69-96; **1995**.

[72] J. A. C. Schwatz, C. I.; Putyera, K.; *Dekker Encyclopedia of Nanoscience and Nanotechnology*, 166; **2004**

[73] S. H. Othman, S. Abdul Rashid, T. I. Mohd Ghazi and N. Abdullah, *J. of Nanom.*, pp. 2011, **2011**

[74] S. Tieng, R. Azouani, K. Chhor and A. Kanaev; *J. of Phys. Chem. C*, 115, 5244-5250; **2011**.

[75] A. Zaleska; *Rec. Pat. on Eng.*, 2, 157-164; **2008**.

[76] F. E. Senftle, Pankey, T., Grant, F. A; *Phys. Rev.*, 120, 820-825; **1960**.

[77] S. D. Yoon, Y. Chen, A. Yang, T. L. Goodrich, X. Zuo, D. A. Arena, K. Ziemer, C. Vittoria and V. G. Harris; *J. of Phys-Cond. Mat.*, 18, L355-L361, **2006**.

[78] X. Zuo, S.-D. Yoon, A. Yang, W.-H. Duan, C. Vittoria and V. G. Harris; *J. of Appl. Phys.* 105; pp. 503; **2009**.

[79] J. M. D. Coey, M. Venkatesan, P. Stamenov, C. B. Fitzgerald and L. S. Dorneles; *Phys. Rev. B*, 72, 024450; **2005**.

[80] W. J. Danley and L. N. Mulay*; Mat. Res. Bull.*, 7, pp. 739-747; **1972**.

[81] L. K. Keys, Mulay, L. N.; *Phys. Rev.*, 154, 453; **1967**.

[82] L. K. Keys and L. N. Mulay*, J. of Appl. Phys.*, 38, 1466-1467; **1967**.

[83] S. D. Yoon, Y. J. Chen, A; Yang, T. L. Goodrich, X. Zuo, K. Ziemer, C. Vittoria and V. G. Harris*; J. of Magn. and Magn. Mat.*, 309, 171-175; **2007**.

[84] Y. Alivov, T. Grant, C. Capan, W. Iwamoto, P. G. Pagliuso and S. Molloi; *Nanotechnology,* 24, 275704; **2013**.

[85] N. N. Hai, N. T. Khoi and P. V. Vinh; *APCTP-ASEAN Workshop on Advanced Mat. Sc. and Nanot.* (Amsn08), 187; **2009**.

[86] D. L. Hou, H. J. Meng, L. Y. Jia, X. J. Ye, H. J. Zhou and X. L. Li; *Epl*, 78; 67001, **2007**.

[87] J. D. Bryan, S. A. Santangelo, S. C. Keveren and D. R. Gamelin; *J. of the Am. Chem. Soc.*, 127, 15568-15574; **2005**.

[88] N. H. Hong; *J. of Magn. and Magn. Mat.*, 303, pp. 338-343; **2006**.

[89] J. P. Wittke; *J. of Am. Ceram. Soc.*, 50, 586-588; **1967**.

[90] W. Wang, J. Dai, J. Tang, D. T. Jiang, Y. Chen, J. Fang, J. He, W. Zhou and L. Spinu; *J. of Supercond.*, 16, 155-157; **2003**.

[91] L. C. Sanchez, A. M. Calle, J. D. Arboleda, J. J. Beltran, C. A. Barrero, J. Osorio and K. Nomura; *Hyperfine Interactions*, 183, 117-122; **2008**.

[92] Y. Ding, W. Q. Han and L. H. Lewis; *J. of Appl. Phys.*, 102; **2007**.

[93] M. Guo, J. Zhao, X. Xu, G. Liu and X. Wang; *Ceram. Inter.*; pp. 1011-1019, **2013**.

[94] D.K. Smith and H.W. Newkirk; *Act Cryst*. 18, 989-991; **1965**

[95] R. J. Hill and L.M.D. Cranswick*; J. Appl. Cryst*. 27, 802-844; **1994**

[96] P. Southon, *Dissertation*, University of Technilogy, Sydney, Australia; **2000**

[97] C.J. Howard, R.J. Hill and B.E. Reichart; *Act. Cryst.* B44, 116; **1988**

[98] R.E. Hann, P.R. Suitch and J.L. Pentecost; *Commun. Am. Ceram. Soc*. 1985 C285-C286; **1985**

[99] J. Adam and M.D. Rogers; *Acta Crys*. 12, 951; **1959**

[100] E. H. Kisi and C.J. Howard; *Key Eng. Mat.* P. 153-154 p. 1-36; **1998**

[101] H. Baker; *ASM International*, Ohio, USA; p. 95 – 112; **1992**

[102] G. Teufer; *Acta Cryst*. 15, 1187; **1962**

[103] D. Michel, L. Mazerolles and M.P.Y. Jorber; *J. Mater. Sci*. 18 2618-2628; **1983**

[104] N. Igawa, Y. Ishii, T. Nagasaki, Y. Morii, S. Funahashi and H. Ohno; *J. Am. Ceram. Soc.* 76*,* 2673-2676; **1993**

[105] H. Nishizawa, N. Yamasaki, K. Matsuoka and H. Mitsushio; *J. Am. Ceram. Soc*. 65 [7] 343-346; **1982**

[106] M. Yashima, M. Kakihana, K. Ishii, Y. Ikuma and M. Yoshimura; *J. Mater. Res***.** 11 [6] 1410-1420; **1996**

[107] R. Srinivasan, S.F. Simpson, J.M. Harris and B.H. Davis; *J. Mater. Sci. Lett*. 10 , 352-354; **1991**

[108] M. Yoshimura; *Bull. Am. Ceram. Soc*. 67 [12] 1950-1955; **1988**

[109] A. H. Heuer, R. Chaim and V. Lanteri; *Adv. in Ceram.* 24 3-20; **1988**

[110] E. P. Butler; *Mater. Sci. Tech*. 1 417-431 **1985**

[111] R. L. Withers, J.G. Thompson, N. Gabbitas, L. R. Wallenberg and T. R. Welberry; *J. Sol. St. Chem*. 120**,** 290-298; **1995**

[112] X. Lu, K. Liang, S. Gu, Y. Zheng and H. Fang*; J. Mater. Sci*. 32, 6653-6656; **1997**

[113] C.J. Howard, B.A. Hunter and D.-J. Kim; *J. Am. Ceram. Soc***.** 81*,* 241-243; **1998**

[114] D.-J. Kim; *J. Am. Ceram. Soc.* 80*,* 1453-1461; **1997**

[115] R.N. Patil and E.C. Subbarao; *Acta. Cryst.* A26 535-542; **1970**

[116] A.H. Heuer and M. Rühle, *Acta Metall*. 33, 2101-2112; **1985**

[117] B. C. Muddle and G. R. Hugo "*Proceedings of the International Conference on Martensitic Transformations",* Monterey, pp. 647-658; **1993**

[118] F. Frey and H. Boysen; *Proc. of the Inter. Conf. on Mart. Trans.*, Monterey, 659-664; **1993**

[119] J. Ortín; *Proc. of the Inter. Conf. on Mart. Trans.*, Monterey, 305-316; **1992**

[120] T. Kanno; *J. Mater. Sci*. 25 1987-1990; **1990**

[121] A. H. Heuer, N. Claussen, W. M. Kriven and M. Rühle; *J. Am. Ceram. Soc*. 65*,* 642-650; **1982**

[122] Y. C. Lin, D. Gan and P. Shen; *J. Am. Ceram. Soc*. 79*,* 559-61; **1996**

[123] R. C. Garvie and M. F. Goss; *J. Mater. Sci*. 21 1253-1257; **1986**

[124] R. C. Garvie and S. K. Chan; *Mat. Sc. For.* 34-36 95-101; **1988**

[125] C. H. Perry and D. W. Liu; *J. Am. Ceram. Soc.* 68, C184-C187; **1985**

[126] V. V. Osiko, Y. K. Voron'ko and A. A. Sobol; "*Growth and Defect Structures - Crystal 10",* Edited by H.C. Freyhard; Springer-Verlag, Berlin; **1984**

[127] P. M. Kelly; *Mater. Sci. Forum* 56-58 335-346; **1990**

[128] N. K. Simha, *Journal de Physique IV* 5 (C8) 1121-1126; **1995**

[129] R. Srinivasan, B. H. Davis, L. A. Rice and R. J. De Angelis; *J. Mater. Sci*. 27 661-670; **1992**

[130] R. Srinivasan, L. Rice and B. H. Davis; *J. Am. Ceram. Soc*. 73*,* 3528-3530; **1990**

[131] Y. Murase and E. Kato; *J. Am. Ceram. Soc*. 66, 196-200; **1983**

[132] D. A. Ward and E. I. Ko; *Chem. Mater*. 5 956-969; **1993**

[133] S. K. Chan; *Adv. in Ceram.* 24 983-995; **1988**

[134] T. Suzuki and K. Takahashi; *Proc. of the Inter. Conf. on Mart. Trans.,* Monterey, 173-178; **1993**

[135] C. A. Andersson and T. K. Gupta; *Adv. in Ceram.* 3 184-201; **1981**

[136] Prof. P. Kelly, University of Queensland, personal communication; **1996**

[137] Vij. D. R; "*Luminescence of solids",* Plenum Press New York; **1998**

[138] C. Fouassier; *Encycl. of Inorg. Chem.*, Accademic Press New York; **1984**

[139] S. W. S. Mckeever; "*Thermoluminescence of Solids"* Cambridge University Press Cambridge; **1985**

[140] P. I. Paulose; *Dissertation*; School of Pure and Applied Physics, Kottayam, India; **2002**

[141] R. H. Bube; *Phys. Rev*. 80 655; **1950**

[142] M. Omar and H. H. Patterson; *Encycl. of Spectr*. Academic Press New York; **1999**

[143] L. Marton; *Sol. St. of Phys.*. Academic Press New York 6; **1959**

[144] R. P. Rao; *J. Mater. Sci*. 21, 3357; **1986**

[145] L. K. Bailif; "*Scientific Dating methods",* Brussels and Luxembourg Netherlands; **1991**

[146] W. Assmus, N. Whippey; *Chem. Ing. Tech.* 55, 716-717; **1983**;

[147] H. Römer, K. D. Luther, W. Assmus; *Cryst. Res.Technol*. 29 (6), 787-794; **1994**

[148] R. F. Sekerka, R. A. Hartzell, B. J. Farr; *J. Cryst. Growth*; 50 (4), 783-800; **1980**

[149] V. I. Aleksandrov, V. V. Osiko, A. M. Prohorov, V. M. Tatarintsev; *Current Topics in Materials Science* Vol**.** 1; **1978**

[150] V. Cingoski, H. Yamashita; *IEEE Trans. on Magn.*; Vol. 30 No. 5, 3459-3462; **1994**

[151] H. R. Harrisson, J. M. Honig; *Bull. Mater. Sci.*; Vol. 3; No. 3 247-253; **1981**

[152] S. Yu, E. Kuz'minov, E. Lomonova, V. V. Osiko, Lomonova, *"Cubic Zirconia and Skull melting";* Cambridge International Science Publishing (CISP); **2008**

[153] G. Ulbrich; *Dissertation*; Technische Universität Berlin, Berlin; **2015**

[154] S. Berendts; *Dissertation*; Technische Universität Berlin, Berlin; **2010**

[155] J. Rodriguez-Carvajal, "*Recent advances in magnetic structure determination by neutron powder diffraction";* Physica B*:* Condensed Matter; p. 95 – 112; **1993**

[156] R. Allmann, A. Kern; Springer-Verlag; 2. Auflage; **2003**

[157] E. Prince; *Inter. Tab. for Crystal. Vol. C*, International Union of Crystallography; **2004**

[158] J. M. Bijvoet, W. G. Burgers, G. Hägg; "*Early Papers on Diffraction of X-rays by Crystals";* A. Oosthoek's Uitgeversmaatschappij N. V. Utrecht; 7-22; **1969**

[159] K. Moffat, D. Szebenyi, D. Bilderback; *Science* Vol. 223 1423-1425; **1984**

[160] N. E. Brese and M. O'Keeffe; *Acta Cryst*. B47 192-197; **1991**

[161] I. D. Brown and D. Altermatt; *Acta Cryst*. B41 244-247; **1985**

[162] W. L. Wang, H. Y. Lu; *Phys. Chem. Minerals* 33 435-444; **2006**

[163] M. I. Aroyo, J. M. Perez-Mato, D. Orobengoa, E. Tasci, G. de la Flor, A. Kirov; *Bulg. Chem. Commun*. 43(2) 183-197; **2011**.

[164] M. I. Aroyo, J. M. Perez-Mato, C. Capillas, E. Kroumova, S. Ivantchev, G. Madariaga, A. Kirov & H. Wondratschek; *Z. Krist.* 221 1, 15-27; **2006**.

[165] M. I. Aroyo, A. Kirov, C. Capillas, J. M. Perez-Mato & H. Wondratschek; *Acta Cryst.* A62 115-128; **2006**.

[166] M. I. Aroyo, J. M. Perez-Mato, C. Capillas, E. Kroumova, S. Ivantchev, G. Madariaga, A. Kirov and H. Wondratschek; *Z. Krist.* 221 1, 15-27; **2006**.

[167] E. Kroumova, J. M. Perez-Mato and M. I. Aroyo; *J. Appl. Cryst.* 31, 646; **1998**.

[168] J. B. Kennedy and C. J. Howard; *Phys. Rev. B* Vol. 59 No.6; 4146; **1999**

[169] J. M. Park, F. Gotoda, S. Nakashima, T. Kanashima and M. Okuyama; *Cur. Appl. Phys.* Vol 11, Issue 3, 270 – 273; **2011**

8. APPENDIX

Table 8.1. List of used chemicals, their purity and supplies.

Chemical	Purity	Company
ZrO_2	99.99 %	SurfaceNet GmbH
Y_2O_3	99.99 %	SurfaceNet GmbH
TiO_2	99 %	AppliChem
$CaCO_3$	99 %	ChemPur
$SrCO_3$	99 %	SurfaceNet
$BaCO_3$	99 %	Chempur
Fe_2O_3	99.9 %	Chempur
NiO	99.9 %	Auer Remy GmbH
Co_3O_4	99.99 %	Chempur
$MnCO_3$	99.9 %	Aldrich Chemistry
Nb_2O_5	99.9 %	Fluka AG
Eu_2O_3	99.9 %	SurfaceNet GmbH
Er_2O_3	99.9 %	SurfaceNet GmbH
Tb_2O_3	99.9 %	SurfaceNet GmbH
Yb_2O_3	99.9 %	SurfaceNet GmbH
Tm_2O_3	99.9 %	SurfaceNet GmbH
Zr	-	Haines & Maassen
Ti	99,8 %	ChemPur

Table 8.2. Measures and thickness for REE:YSZ (REE = Eu, Er, Tb, Yb, Tm) single crystals samples.

Samples	Measures [mm]	Thickness [µm]
Eu:YSZ	19.1 x 10.6	1988
(Er,Yb):YSZ	11.6 x 10.7	1980
Tb:YSZ	12.3 x 9.7	1995
(Tm,Yb):YSZ	9.4 x 7.9	1996

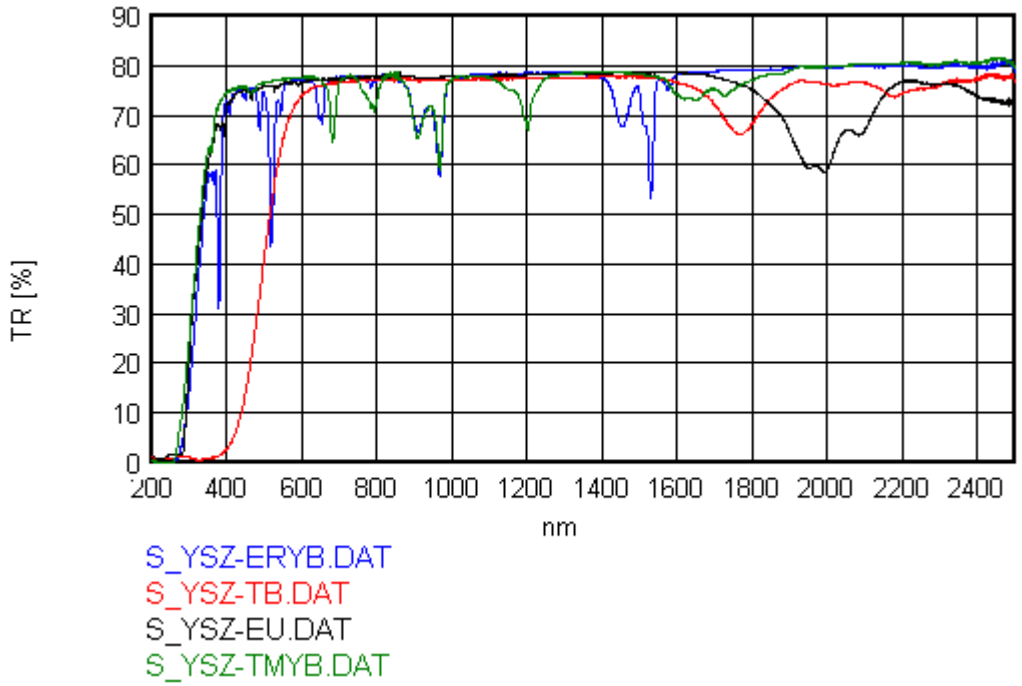

Figure 8.1. Overview of all transmission spectra of the REE:YSZ (REE = Eu, Er, Tb, Yb, Tm) single crystals (raw data).

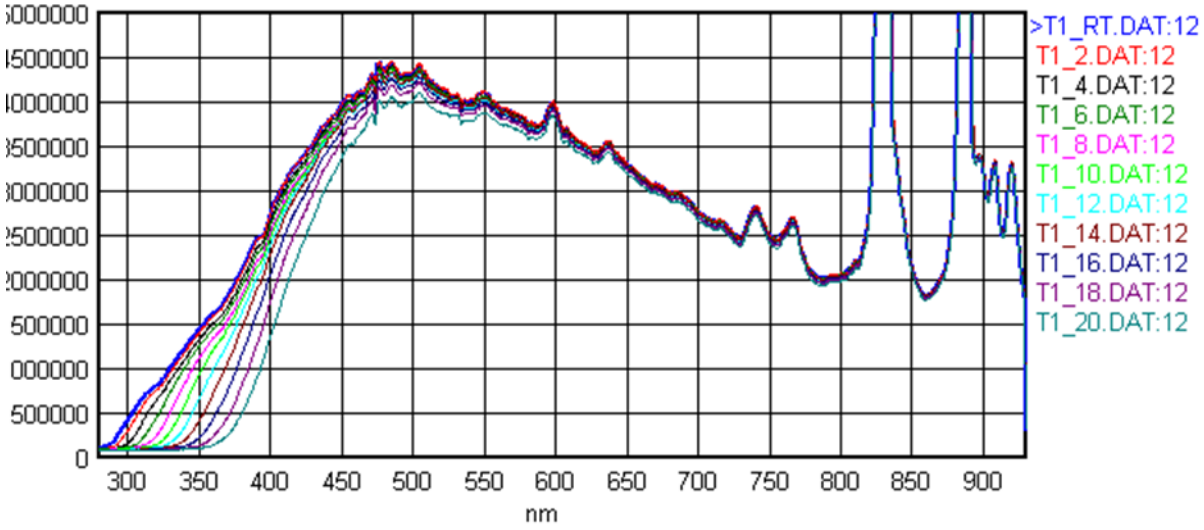

Figure 8.2. Complete high temperature absorbance spectra of Eu:YSZ (raw data).

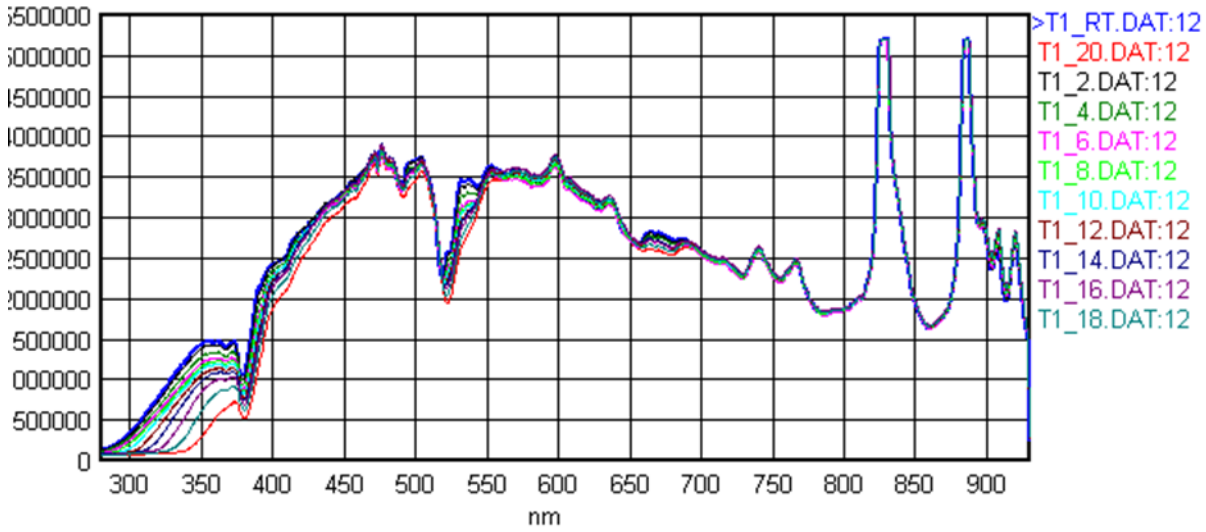

Figure 8.3. Complete high temperature absorbance spectra of (Er,Yb):YSZ (raw data).

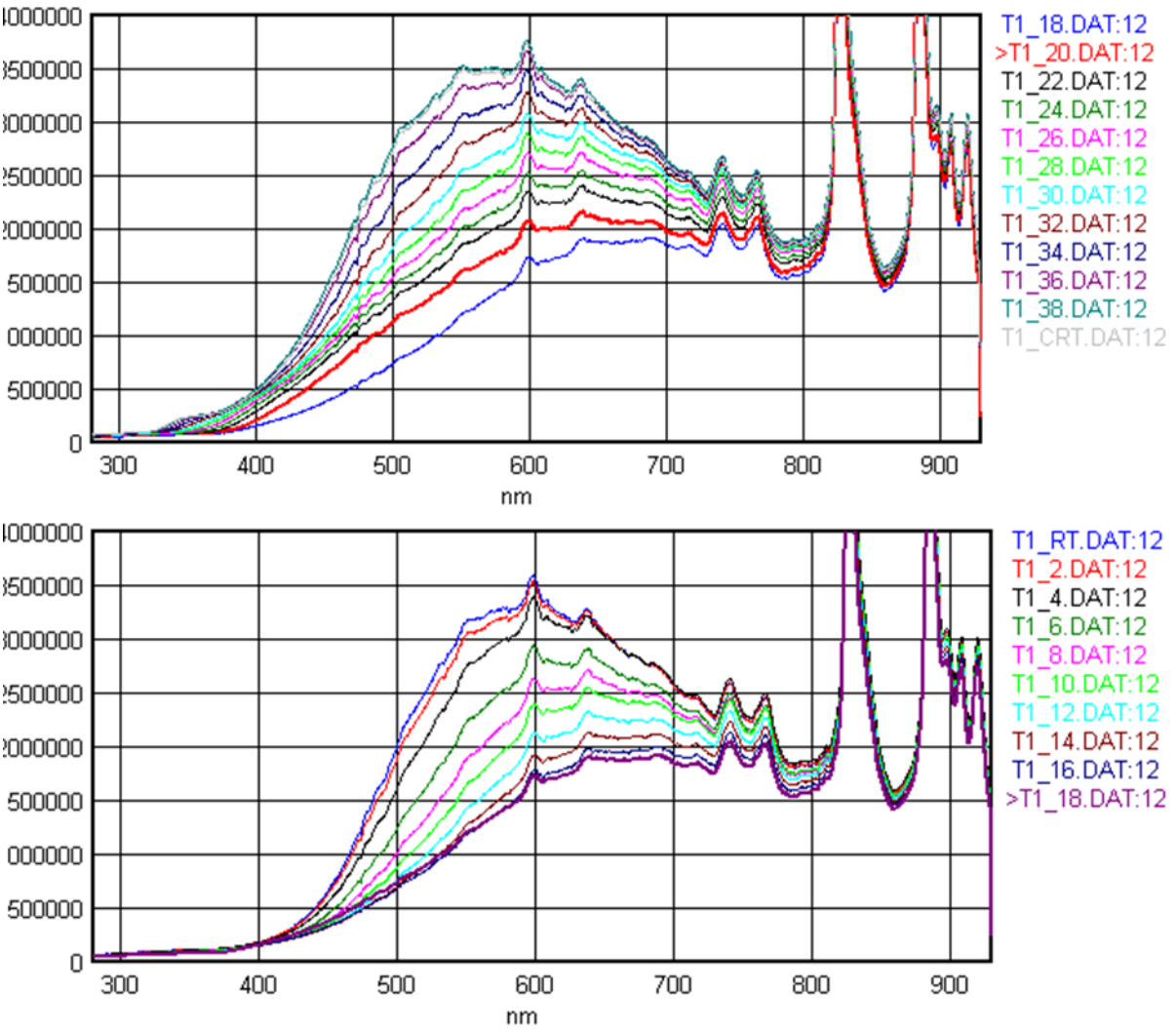

Figure 8.4. Complete high temperature absorbance spectra of Tb:YSZ; upon heating (up) and cooling (down); (raw data).

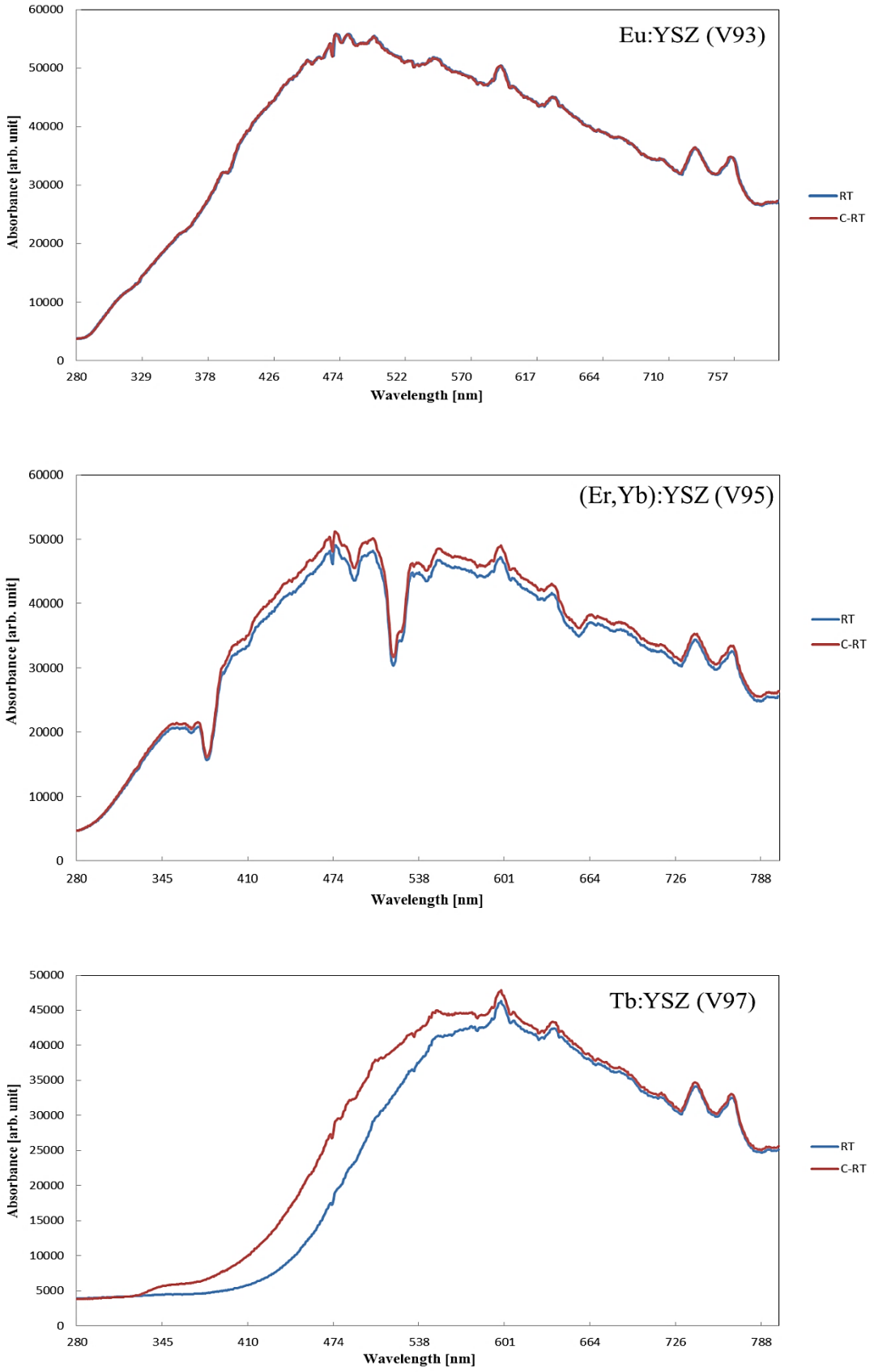

Figure 8.5 Absorbance spectra of Eu:YSZ (V93), (Er,Yb):YSZ (V95) and Tb:YSZ (V97) before (RT) and after the heating (C-RT) process.

List of Figures

List of Tables